

1 20170727: DARK MATTER SEARCH AND ELECTRON BACKGROUND
2 EVALUATION
3 TESTING OF TPC GRID DESIGNING

4 A DISSERTATION
5 SUBMITTED TO THE DEPARTMENT OF PHYSICS
6 AND THE COMMITTEE ON GRADUATE STUDIES
7 OF STANFORD UNIVERSITY
8 IN PARTIAL FULFILLMENT OF THE REQUIREMENTS
9 FOR THE DEGREE OF
10 DOCTOR OF PHILOSOPHY

11 Wei Ji
12 August 2018

¹³

© Copyright by Wei Ji 2018
All Rights Reserved

¹⁴

I certify that I have read this dissertation and that, in my opinion, it is fully adequate in scope and quality as a dissertation for the degree of Doctor of Philosophy.

15

(Tom Shutt) Principal Adviser

I certify that I have read this dissertation and that, in my opinion, it is fully adequate in scope and quality as a dissertation for the degree of Doctor of Philosophy.

16

(Dan Akerib)

I certify that I have read this dissertation and that, in my opinion, it is fully adequate in scope and quality as a dissertation for the degree of Doctor of Philosophy.

17

(Peter Graham)

I certify that I have read this dissertation and that, in my opinion, it is fully adequate in scope and quality as a dissertation for the degree of Doctor of Philosophy.

18

(Giorgio Gratta)

I certify that I have read this dissertation and that, in my opinion, it is fully adequate in scope and quality as a dissertation for the degree of Doctor of Philosophy.

19

()

Approved for the Stanford University Committee on Graduate Studies

20

²¹ Preface

²² This thesis is discussing about the design and validation of liquid xenon LZ Dark Matter experiment
²³ and results from LUX Dark Matter experiment.

²⁴ **Acknowledgments**

²⁵ I would like to thank you Dan, for everything.

²⁶ Contents

²⁷ Preface	iv
²⁸ Acknowledgments	v
²⁹ List of Tables	viii
³⁰ List of Figures	ix
³¹ 1 Gas Test descriptions	1
³² 1.1 The gaseous detector	2
³³ 1.2 Data Acquisition	7
³⁴ 1.3 Operation	11
³⁵ 1.4 Data processing	14
³⁶ 1.5 PMT Calibration	17
³⁷ 1.6 Light Collection	22
³⁸ 1.7 Light production	25
³⁹ 1.8 Signals	32
⁴⁰ 1.8.1 Electron emission	32
⁴¹ 1.8.2 Particle radiation	36
⁴² 1.8.3 Cosmic ray	50
⁴³ 1.8.4 Other miscellaneous sources	54
⁴⁴ 1.9 Signal selections	71
⁴⁵ 1.9.1 Signal selections based on signal shape	73
⁴⁶ 1.9.2 Signal selections based on previous signals	79
⁴⁷ 1.9.3 Signal selections varying $\Delta V_{T,B}$ and operating gas density	86
⁴⁸ 1.10 Evaluation	92
⁴⁹ 1.10.1 Simulations	92
⁵⁰ 1.10.2 Summary	92

51 A Gas Test RQ documentation **94**

52 B Abbreviations **101**

⁵³ **List of Tables**

⁵⁴ 1.1	Spectral response of PMTs tested at Hamamatsu Photonics	5
⁵⁵ 1.2	Data Acquisition system parameters.	8
⁵⁶ 1.3	PMT dead time duration	11
⁵⁷ 1.4	PMT calibration.	20
⁵⁸ 1.5	Light collection simulation geometry parameters.	24
⁵⁹ 1.6	Light collection simulation material parameters.	24
⁶⁰ A.1	<i>Gas Test</i> RQ documentation	100

⁶¹ List of Figures

62 1.1	<i>Gas Test</i> apparatus physical layout.	4
63 1.2	<i>Gas Test</i> electroluminescence detector.	6
64 1.3	<i>Gas Test</i> signal: example waveforms during dead time.	10
65 1.4	Distribution of PMT time differences between pulses in one PMT.	12
66 1.5	<i>Gas Test</i> good and bad voltage configurations.	15
67 1.6	PMT pulse amplitude distribution.	19
68 1.7	PMT SPHE pulse amplitude vs. pulse area distribution.	21
69 1.8	Light collection efficiency of (r, z) cross section in the ELD from simulation.	26
70 1.9	Light collection efficiency and TBA in the EL region in different grid configurations from simulation.	27
71 1.10	Light collection efficiency in the EL region with different PTFE reflectivity from simulation.	27
72 1.11	The reduced first Townsend ionization coefficient $\eta \equiv \alpha/E$ for neon, argon, krypton, and xenon.	31
73 1.12	<i>Gas Test</i> electron emission event from grid wires	34
74 1.13	<i>Gas Test</i> detector electric field.	35
75 1.14	A 3D simulation of an electron drifting in an axially symmetric electric field in xenon gas.	37
76 1.15	Simulated cathodic electron gas gain vs. reduced surface electric field.	38
77 1.16	Simulated signal areas vs. ΔV_{T-B}	39
78 1.17	Attenuation length of photon in xenon.	41
79 1.18	CSDA range of electrons in xenon.	41
80 1.19	<i>Gas Test</i> signal: anode cone event.	43
81 1.19	<i>Gas Test</i> signal: anode cone event (cont.).	44
82 1.20	<i>Gas Test</i> signal: cathode cone event.	45
83 1.21	<i>Gas Test</i> signal: S1 S2 event in the cathode corner.	47
84 1.22	Electrostatic solution of the <i>Gas Test</i> detector (grid ring region).	48

89	1.23 <i>Gas Test</i> signal: S1 S2 event in the EL region.	49
90	1.24 <i>Gas Test</i> signal: grid wire region event.	51
91	1.25 <i>Gas Test</i> signal: grid ring region event.	52
92	1.26 <i>Gas Test</i> signal: multiple scattering event.	53
93	1.27 <i>Gas Test</i> signal: EL region muon event.	55
94	1.28 <i>Gas Test</i> signal: muon event between the grid rings.	56
95	1.29 <i>Gas Test</i> signal: anode cone muon event.	57
96	1.29 <i>Gas Test</i> signal: anode cone muon event (cont.).	58
97	1.30 <i>Gas Test</i> signal: cathode cone muon event.	59
98	1.31 <i>Gas Test</i> signal: electronic noise.	61
99	1.32 <i>Gas Test</i> signal: PMT dark current accidental coincidence.	61
100	1.33 <i>Gas Test</i> signal: PTFE fluorescence after an event with large photon production.	63
101	1.33 <i>Gas Test</i> signal: PTFE fluorescence after an event with large photon production (cont.).	64
102	1.34 Photon fluorescence rate after photon production in the ELD.	65
103	1.35 The average of scaled waveform in the range of 0 μ s to 2000 μ s since source signals.	68
104	1.36 The ratio of the number of photon in the range of 200 μ s to 600 μ s since source signals to the number of photons in the source signal.	68
105	1.37 <i>Gas Test</i> signal: Cherenkov radiation in PTFE.	69
106	1.38 <i>Gas Test</i> signal t_{10-90} duration vs. signal area.	72
107	1.39 <i>Gas Test</i> signal selection (part 1).	82
108	1.39 <i>Gas Test</i> signal selection (part 2).	83
109	1.39 <i>Gas Test</i> signal selection (part 3).	84
110	1.39 <i>Gas Test</i> signal selection (part 4).	85
111	1.40 <i>Gas Test</i> signal selection with ΔV_{T-B} at 8 kV, operating gas density at 0.137 mol L $^{-1}$	87
112	1.41 <i>Gas Test</i> signal selection with ΔV_{T-B} at 10 kV, operating gas density at 0.137 mol L $^{-1}$	88
113	1.42 <i>Gas Test</i> signal selection with ΔV_{T-B} at 12 kV, operating gas density at 0.137 mol L $^{-1}$	89
114	1.43 <i>Gas Test</i> signal selection with ΔV_{T-B} at 14 kV, operating gas density at 0.137 mol L $^{-1}$	90
115	1.44 <i>Gas Test</i> signal selection with ΔV_{T-B} at 16 kV, operating gas density at 0.137 mol L $^{-1}$	91

¹¹⁷ **Chapter 1**

¹¹⁸ ***Gas Test descriptions***

¹¹⁹ In LZ, metallic wire grids under high voltage are used to form electric fields. We apply one field
¹²⁰ in the liquid volume to drift ionization electrons upwards and another in the gas volume to extract
¹²¹ these electrons from the liquid in order to produce proportional scintillation light (S2). Achieving
¹²² high voltages on such grids is necessary for the operation of the LZ TPC. However, such high voltages
¹²³ also increase the rate of electron emission ,which is one of the potential sources of background in
¹²⁴ LZ. Therefore, reduction of the field induced electron emission rate should greatly benefit physics
¹²⁵ studies in the LZ detector.

¹²⁶ Electric field induced electron emission from metallic surfaces is a well known phenomenon. The
¹²⁷ electric field lowers the potential energy outside the metallic surface allowing electrons to come out
¹²⁸ from the metallic surface. The rate of electric field induced electron emission increases with the
¹²⁹ electric field on the metallic surface.

¹³⁰ The electric field induced electron emission events are potential problems in LZ for three reasons.
¹³¹ First, these events look like low energy events in the LZ detector. Thus, reduction of electron
¹³² emission background rate from the grid wires improves our sensitivity to low energy events. This
¹³³ in turn improves our ability to study low mass WIMPs. Second, the electron emission events may
¹³⁴ accidentally coincide with WIMP signals which we want to study in the LZ detector. Reduction
¹³⁵ of electron emission rate helps to keep the data recording environment in LZ cleaner. This reduces
¹³⁶ the systematic errors for S1 and S2 and improves their quality. From that, we improve our events
¹³⁷ classification and energy reconstruction. This in turn improves all physics studies using the LZ
¹³⁸ detector. Finally, the electron emission events interrupt the desired data recording capability of
¹³⁹ the LZ detector. This may prevent or interrupt recordings of wanted data. Thus, the reduction of
¹⁴⁰ electron emission rate helps to keep the data recording environment in LZ quieter to allow longer
¹⁴¹ detector live times for wanted events. In summary, the reduction of the electron emission event rates
¹⁴² benefits LZ because of its impact on detector sensitivity, data quality and data acquisition live time.

¹⁴³ To achieve these qualities, we are developing a two-stage study on the reduction of the electric

144 field induced electron emission rate using two small detectors, *Gas Test* and *LZ System Test: Phase*

145 *I*. These two detectors are capable of testing a pair of grids which have surface areas $\sim 1\%$ the

146 area of grids that will be used in LZ. With these small detectors, we can study the effect of rate

147 reduction in a shorter time than if we were to use full-size grids. Thus, we use these detectors to

148 study parameters that may affect the emission rate in a short period of time.

149 At the first stage, a gaseous detector, “*Gas Test*”, is built to study different methods for reducing

150 the electron emission rate. This detector measures electron emission rates with different electric

151 fields before and after various physical and chemical treatments. Once we discover an effect on the

152 reduction of the electric field induced electron emission rate from these treatments, a second stage

153 of study with a liquid xenon detector, *LZ System Test: Phase I*, is undertaken to confirm that

154 reduction persists in a liquid xenon environment, like that of LZ.

155 After confirmation that a treatment produces a rate reduction, this treatment is used to produce

156 full-size LZ grids. A similar two-stage study method is used to test the full-size LZ grids in a gaseous

157 detector, *LZ System Test: Phase II*(details are described in Ref. ??), and the liquid xenon detector

158 LZ. These two detectors measure the performance and assure the quality of LZ grids.

159 This chapter focuses on descriptions of the *Gas Test* detector. I will first introduce the design

160 concepts for each individual component in *Gas Test* . Then I will discuss data acquisition and the

161 data processing framework. **Last, I will discuss the analysis framework ,which includes event selec-**

162 **tions , simulations and validations, as well as characteristic pulse shape and rate of the background**

163 **events.** Results from measurements for different grids in *Gas Test* will be discussed in Chapter.??.

164 1.1 The gaseous detector

165 The gaseous detector, *Gas Test*, is designed to study grid behavior under high voltage in LZ. It

166 measures scintillation and electroluminescence (EL) light signals from events in the detector. Pairs

167 of grids are made from the same waving technique, material, wire pitch, and wire diameter as the

168 grids that will be used in LZ. The same pair of grids can also be tested in *LZ System Test: Phase I*

169 to study their performance in liquid xenon. Since these grids are physically similar to the grids in

170 LZ except for the overall surface area, the results from studying these grids are useful for LZ grid

171 design.

172 The main interest of our study is the electron emission process from the grid wires, which

173 is studied by grid electron emission tests via using PMTs to detect the associated photon signals.

174 Before each grid electron emission test, a grid sparking test is carried out to understand the maximum

175 operating voltage and the optimal operating voltage. Grid sparking tests are performed with both

176 gaseous xenon and argon under various pressures in order to uncover discharges in the detector

177 via biasing the grids. It provides the detector operation information for grid emission tests. Grid

178 electron emission tests are usually performed with gaseous xenon, in which photons can be produced

179 for carrying out the electron emission signalmeasurements.

180 Next, I will introduce the design concepts of the components in the *Gas Test* detector.

181 **Detector** *Gas Test* detector is the main tool we used to study the electron emission process from
182 metallic grid wire surfaces. The *Gas Test* detector operates with xenon gas, argon gas, and vacuum.
183 The operating pressure for this detector is in the range of 10^{-5} bara to 3.5 bara.

184 A cylindrical vessel, the diameter of which is 10 inch and the height of which is 24 inch, is used to
185 host a electroluminescence detector(ELD), which detect measurable events. The pressure and the
186 temperature of the detector are monitored by sensors mounted above the vessel. A gas circulation
187 system is used to add, remove and purify gas in the detector. Fig. 1.1a and Fig. 1.1b show the
188 physical layout of the vessel setup and the ELD inside.

189 The electroluminescence detector (ELD) is the major location of active measurable electron
190 emission events. Its conceptual drawing is illustrated in Fig. 1.2. A pair of grids for measurement
191 are mounted in the center of the vessel. They are separated apart by 12 PEEK spacers, ,which are
192 13 mm in height. These two grids are biased to different voltages during the measurement. This
193 creates a voltage difference between the two grids. It enables electrons between these two grids to
194 produce EL photons ,which can be measured by the PMTs. The region between these two grids is
195 called the EL region.

196 These grids are named after their physical location in the detector as top grid and bottom grid.
197 The grid plane diameters are 140.9 mm for the top grid and 137.4 mm for the bottom grid. Voltages
198 of the two grids are noted as V_T for the top grid and V_B for the bottom grid. The voltage difference
199 between the top and bottom grids is expressed with ΔV_{T-B} (dV) $\equiv V_T - V_B$. These grids also
200 have another name by their bias voltages; the anodic grid and cathodic grid, and their voltage are
201 respectively V_A and V_C . The top grid is anodic and the bottom grid is cathodic when studying
202 electron emission from the bottom grid, which is called normal polarity operation. Occasionally, the
203 top grid is cathodic and the bottom grid is anodic when studying electron emission from the top
204 grid, which is called reverse polarity operation.

205 Two PTFE reflector cones are used to improve light collection efficiency for the primary scintil-
206 lation and EL photons. These reflector cones are mounted on the top and bottom of the EL region.
207 The surface of the PTFE cones overhang 0.1 mm above the grid. The diameters of the opening of
208 the PTFE cones to the grids are 130 mm. The EL region have the most sensitivity for grid electron
209 emission signal with regart to light collection. The EL region defines the overall grid surface area
210 of studying. Two PMTs mounted on the PTFE reflector cones are used to measure the primary
211 scintillation and EL photons. Distances between the PMTs to the closest grids are 110 mm.

212 The two PMTs used to measure the primary scintillation and EL photons from events happening
213 in the detector are model R11410-20 PMTs manufactured by Hamamatsu Photonics, as described
214 in Ref. [1]. The model of PMT has a synthetic quartz window that is mostly transparent to incident
215 photons of ~ 175 nm (xenon scintillation photons). The PMT window is coated with a bialkali



Figure 1.1: *Gas Test* apparatus physical layout. (a) The *Gas Test* detector: detector vessel (middle), electronic and gas gauge breakouts (top), Genie lift for detector assembly and disassembly (left), vacuum pumps and leak checking system (right). (b) ELD inside the detector vessel. (c) Gas circulation panel. (d) Circulation pump (left), and storage bottles (right).

photocathode material, which absorbs the incident photon and emits electrons by the photoelectric effect. The emitted electron which lands on the effective area of the first dynode is multiplied along the PMT dynode chain in an electron gain process and observed, which is the measured signal. The two PMTs are named after their physical location in the detector as top PMT and bottom(bot) PMT. Their spectral response of is summarized in Table 1.1.

	Top(top) PMT	Bottom(bot) PMT
Serial Number	KB1163	KB1170
Cathode Luminous Sens. [$\mu\text{A lm}^{-1}$]	149.0	148.0
Anode Luminous Sens. [A lm^{-1}]	657.0	1010.0
Anode Dark Current [nA]	1.00	4.60
Cathode Blue Sens. Index	12.60	12.30
Q.E. [%]		
165 nm	22.1	21.2
170 nm	33.3	32.6
175 nm	36.3	36.0
182 nm	37.1	37.0
188 nm	36.1	36.2
194 nm	33.9	34.1
200 nm	32.6	32.9

Table 1.1: Spectral response of PMTs tested at Hamamatsu Photonics.

A CAEN R1470ETD high voltage power supply is used to bias the two grids and the two PMTs. Two custom ceramic feed-throughs are used to deliver high voltage to the two grids in the detector vessel. Each feed-through has a low-pass filter box attached for noise removal. Custom designed cables and cable terminations are used to apply voltages through the feed-throughs to the grids. The cable terminations were a limitation on our ability to bias the grids to high voltage. New design elements have been introduced to solve this problem. Details of iterations of these designs will be discussed in Chapter. ??.

Gas circulation system A gas circulation system is used to purify, add, and remove xenon gas in the detector. The circulation system maintains the gas purity condition in the detector, which is essential for the operation for the following reasons. The purity of xenon gas ensures that electrons that are produced in the ELD do not combine with impurity atoms, thus decreasing the production of primary scintillation and EL light. The purity of xenon also has a notable effect on electron drift velocity in xenon gas, which biases our study; that is impure xenon gas tends to have a slower electron drift velocity. The deviation of electron drift velocity between different impurity levels can reach 20 % in certain reduced electric fields (ratio of electric field to gas density), as described in Ref. [Brooks1982]. This deviation biases the electron emission signal selection, which is based on the predicted pulse duration according to electron drift velocity, and introduces systematic error to the electron emission signal study.

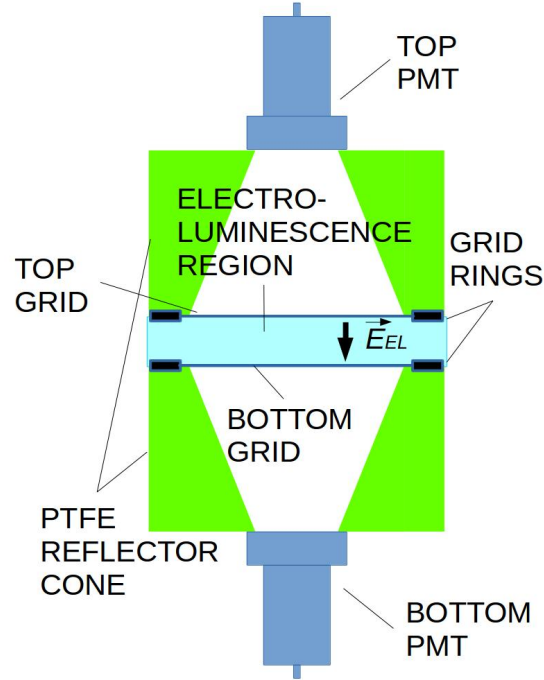


Figure 1.2: Conceptual drawing of *Gas Test* electroluminescence detector (ELD)

Xenon purification is carried out with the following elements in the gas circulation system. A gas circulation panel (Fig. 1.1c) is used to control the flow of xenon gas. A SAES PS3-MT3-R-1 rare gas purifier mounted on the circulation panel is used to purify the gas. The getter element has a sub-ppb efficiency of removing water, nitrogen, oxygen, carbon oxide, carbon dioxide, hydrogen, and hydrocarbons, as described in Ref. [2]. A custom pump (Fig. 1.1d) manufactured by KNF Neuberger, Inc. drives the gas circulation in the system. This pump is a type PM26101-0150.1.2.12 double diaphragm pump, which has company specified 1.5 bar operating pressure, as described in Ref. [3]. During the actual operation, the pump works at pressures of up to 3.7 bar with a leak rate less than 10^{-7} bar L s⁻¹. An Alicat MC-5SLPM-D-485 mass flow controller (MFC) on the gas circulation panel controls the circulation flow rate, which allows a maximum flow rate of 5 slpm, as described in Ref. [4]. During the gas purification process, the flow of gas was controlled and driven through the getter for \sim 20 min to allow the complete absorption of the gas impurities in the detector. This process is frequently conducted between each dataset to ensure the gas purity quality.

The addition and removal of xenon gas are carried out with the same gas panel. Two 4 L bottles (Fig. 1.1d) are used for the storage of xenon gas used in the tests when the gas is not used in the detector. During the xenon gas removal process, these bottles are inserted into two dewars filled with liquid nitrogen. Reducing the temperature of the bottles by using liquid nitrogen allows xenon

256 gas to flow through the gas circulation panel back to the bottles, and to condense inside the bottles.
257 During the addition of xenon gas process, the bottles are taken out from the dewar and warmed up.
258 This process raises the gas pressure in the bottle, which drives the gas to fill the detector through
259 the getter on the gas panel. The gas flow is controlled by the gas regulator and the MFC on the
260 panel.

261 1.2 Data Acquisition

262 A data acquisition(DAQ) system is used for recording PMT pulses for grid emission tests. The
263 DAQ system is designed and made at SLAC, previously used and tested in *LZ System Test: Phase*
264 *I* detector. The DAQ system is customized to maximize the probability for capturing single photon
265 electron (SPHE) pulses from the PMTs. This also enables the DAQ system to record electron
266 emission signals, which are collections of multiple SPHE pulses. The DAQ system contains three
267 parts: (1) amplification and digitization, (2) recording, and (3) transfer and storage. The DAQ
268 system works continuously, except when interrupted by the data transfer process. This interruption
269 is called dead time of the DAQ system. The dead time issue is addressed by the subtraction of live
270 times after each recorded pulses. Aspects of the DAQ system are described below.

271 **Amplification and digitization** This process amplifies and digitizes PMT pulse signals. The
272 amplification and digitization of the PMT signals are carried out by two separate custom made
273 boards. The amplification of signals improves signal to noise ratio. However, this amplification may
274 also cause distortion of the waveform if the pulse signal amplitude exceeds the maximum capability
275 of the electronic circuits in the amplification and digitization boards. Two amplifier gain settings
276 are implemented: low gain ($\times 12$), and high gain ($\times 100$). For electron emission tests, the low
277 gain setting is used to obtain a satisfactory signal to noise ratio. The low gain setting allows 40 to
278 60 SPHEs to be recorded simultaneously without distortion, when the high gain setting is not used
279 because its without distortion SPHE recording range is only 5 to 7 SPHEs, which is too small for the
280 counts of simultaneous SPHEs in electron emission signals. An optical fiber connecting these two
281 boards transfers the amplified PMT signals to the digitizer board. The digitizer board is capable of
282 doing a 16 bit digitization in a dynamic range of 2.5 V (~ -1.26 V to 1.24 V). The digitizer reverses
283 the polarity of signals, which changes SPHE pulses from negative spikes to positive spikes. The
284 digitizing sampling frequency is every 4 ns. Digitized data are written to a buffer memory in the
285 digitizer board. The amplification and digitization system sets the precision of SPHE measurement
286 and signal to noise ratio, and digitizes PMT pulse signals to be handled numerically later.

287 **Recording** The recording system for DAQ makes decisions for data recording. The decision
288 making algorithm is controlled by customized DAQ XML parameters in an XML file. The pulse
289 recording is undertaken in a pending mode without a conventional trigger, which is explained below.

290 First, the continuous digitized pulse amplitude data are compared to a pre-threshold voltage (trigger
 291 voltage), which is called the pre-threshold value, until a threshold crossing is reached. The time of
 292 this threshold crossing is the pulse recording reference time (trigger time). Pulse recording also
 293 includes a preceding segment of samples, which is called the pre-delay. The start time of the
 294 pre-delay period is the pulse recording start time. Next, digitized data are compared to a post-
 295 threshold voltage, which is called the post-threshold value, until a threshold crossing is reached.
 296 Then, the pulse recording continues for a succeeding segment of samples, which is called the post-
 297 delay. During the post-delay period, the digitized data are compared to the pre-threshold value
 298 again. If no pre-threshold crossing is reached, the pulse recording ends when the post-delay period
 299 ends. Otherwise, the DAQ system keeps recording until after a post-threshold crossing is reached,
 300 no other pre-threshold crossing is reached in the next post-delay period. The end time of the last
 301 post-delay period is the pulse recording stop time. The pre-threshold values are chosen so that the
 302 SPHE recording efficiency, also called the trigger efficiency, of both PMTs are larger than 95 %. The
 303 trigger efficiency is estimated by fitting SPHE amplitude distributions to Gaussian distributions, as
 304 described in Section 1.5. Results of these evaluations show that at normal PMT operating voltage
 305 (-1.5 kV) the top PMT and the bottom PMT have good trigger efficiency of 99.6 % and >99.9 %.
 306 The recorded pulses are called pulses of digitization (PODs), which are one of the fundamental
 307 elements for the next step; coincidence event building, as described in Section 1.4.

308 The used DAQ XML parameters during the tests are summarized in Table 1.2.

name	XML parameter name	value	explanation
post-delay	‘PostDelay’	500 sample	counts of samples to keep after crossing post-trigger threshold (‘PostThreshold’).
pre-delay	‘PreDelay’	30 sample	counts of samples to keep before crossing pre-trigger threshold (‘PreThreshold’).
post-threshold	‘PostThreshold’	0x7D80 or as needed	crossing this threshold value determines the stop time of pulse recording.
pre-threshold	‘PreThreshold’	0x7D61 or as needed	crossing this threshold value determines the start time of pulse recording.

Table 1.2: DAQ system parameters. (1 sample is 4 ns.)

309 **Transfer and storage** The transfer and storage system transfers data from the digitizer board
 310 and stores data in binary format in the main computer system. The buffer memory data that pass
 311 the selection of trigger algorithm are transferred through an optical fiber and written to files stored
 312 in the main computer. The data transfer speed is 250 MB s^{-1} . For an average pulse duration of

313 $2\ \mu\text{s}$ (500 sample), the DAQ allows approximately 30 thousand pulses to be recorded per second.
314 The continuously recorded data are separately saved to series of files; each with a maximum size of
315 1.1 GB. The process of data transfer interrupts the process of buffer memory writing of the incoming
316 digitized data, which raises the dead time issue.

317 **Dead time** The dead time of DAQ is the segment of time that the DAQ system stops working
318 after the end of each pulse recording. The reason for the dead time is because the process of buffer
319 writing and the process of data transfer in the DAQ system cannot happen simultaneously. Dead
320 time issue brings challenges in measuring electron emission rates. The duration of dead time shows
321 a dependence on the preceding pulse duration. However, the quantitative relationship between the
322 two is unclear. We address this issue by subtracting a segment of time succeeding each recorded
323 pulse from the live time of study.

324 We studied the dead time issue by using two methods. The first method is finding problematic
325 pulses that might be a result of dead time. We found there exist a population of pulses that when
326 one PMT detects large quantities of photons, the other PMT detects no photon simultaneously.
327 Since the two PMTs are observing the same space in the ELD, we expect to see similar magnitude of
328 photons in both PMTs. The most likely reason for this to happen is that the other PMT channel is
329 suffering from dead time. The other possible causes of these problematic pulses, such as misbehavior
330 of one PMT, are less dominant. The time difference between the recording time of large quantities
331 of photons in one PMT and the first preceding pulse in the dead time problematic PMT is the
332 potential duration of dead time, as shown in Fig. 1.3. More than 400 dead time problematic pulses
333 are examined. From the examinations, we found that for a particular pulse with a duration of $2\ \mu\text{s}$,
334 the duration of dead time is in the range of $0.3\ \mu\text{s}$ to $15\ \mu\text{s}$. For longer pulses, we observe the duration
335 of dead time for as long as $80\ \mu\text{s}$.

336 To estimate the systematic error, we employ a second method based on the idea that the presence
337 of dead time will shift the distribution of time intervals between pulses in one PMT. In the absence
338 of dead time, the time distribution should be an exponential characterized by the average rate.
339 The impact of dead time is to shift time difference probability an exponential curve, which is from
340 assuming uniform distribution:

$$\text{probability} = \frac{1}{\tau} \exp\left(-\frac{t}{\tau}\right) \quad (1.1)$$

341 where τ is the time constant, which is the inverse of average rate.

342 Results of this shift is shown in Fig. 1.4. The figure includes studies of pulses categorized by their
343 durations. These studies confirm the previous conclusion on the dead time issue dominant period,
344 and further show that such period has a dependence on the preceding pulse duration. The clear low
345 statistics at the small time interval range, e.g. range $0\ \text{ns}$ to $10^5\ \text{ns}$ for pulse length in the range of
346 larger than $30\ \mu\text{s}$, clearly showed the shift from expected exponential curve. The low statistic region

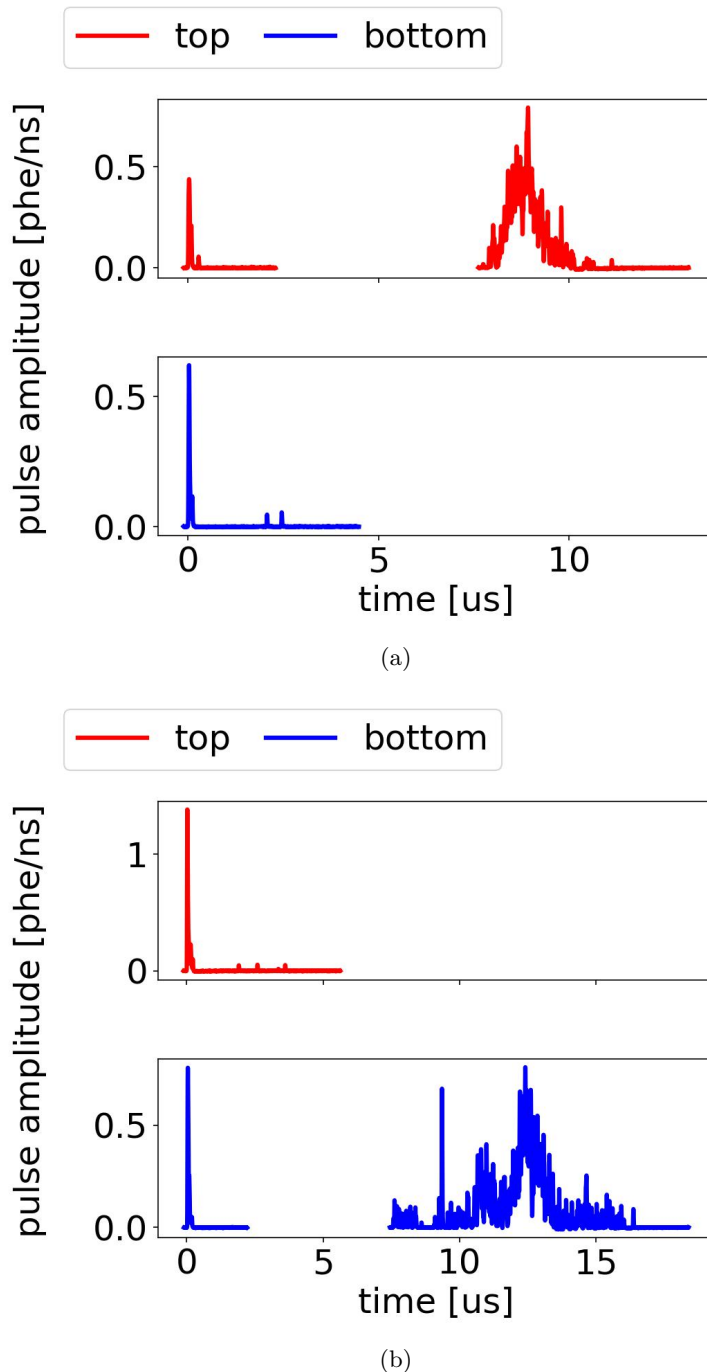


Figure 1.3: *Gas Test* signal: example waveforms during dead time. (a) The top PMT channel is suffering from dead time. (b) The bottom PMT channel is suffering from dead time.

347 changes with preceding pulse duration, as summarized in Table 1.3. The difference on the slopes
 348 of these curves is due to PTFE fluorescence subsequent to each pulse, which is more obvious for
 349 larger area (long duration) pulses, and increases the succeeding average rate, as will be discussed in
 350 Section 1.8.

pulse duration [μs]	dead time duration (low statistics region) [μs]	dead time duration (maximum observed) [μs]
all	7	80
[0, 3)	7	15
[3, 10)	10	15
[10, 30)	50	80
[30, ∞)	100	80

Table 1.3: PMT dead time duration. Data were taken at 2017-12-8 14:02, with grid voltages V_T and V_B at +6 kV and -6 kV, operating gas density at 0.137 mol L^{-1} .

351 Thus, to resolve the dead time issue, we subtract a segment of time after each recorded pulse
 352 from the live time of study and eliminate all pulses that is recorded in this time period, as described
 353 in Section 1.9. The remained pulses that have quiet preceding are used to study the absolute rate
 354 of signals of interest, electron emission signals. The rate of signals of interest is close to such rate
 355 without the dead time issue from the view of DAQ behavior.

356 1.3 Operation

357 think about where to put run selection section. I want to take about , what is sparking test, what
 358 is normal operation before electron emission tests. This is the reason this section is here. however,
 359 put it just in front of cut might also be good.

360 The run selections are to make sure that we have stabilized run conditions to analysis electron
 361 emission process from grids we are studying.

362 **Operating conditions** The normal run of *Gas Test* electron emission test is operated with (1)
 363 the detector filled with xenon gas, (2) two PMTs stably running, and (3) two grids bias to proper
 364 voltages.

365 The typical operating xenon gas density for electron emission tests is 0.137 mol L^{-1} ($\sim 3.3 \text{ bara}$ at
 366 temperature 295 K, or equivalent to the xenon gas density at 177 K on xenon liquid-vapor saturation
 367 curve). This choice minimizes the probability of discharges between two grid electrodes. It also
 368 makes the grids operates under the gas density closest to LZ operating gas density. These discharges
 369 may cause potential damages to grids, and also prevent stable run.

370 The gas operating condition at density 0.137 mol L^{-1} allows us having sensitivities measuring
 371 electron emission from ΔV_{T-B} in the range of 8 kV to 16 kV. For a plain woven grid with wire pitch

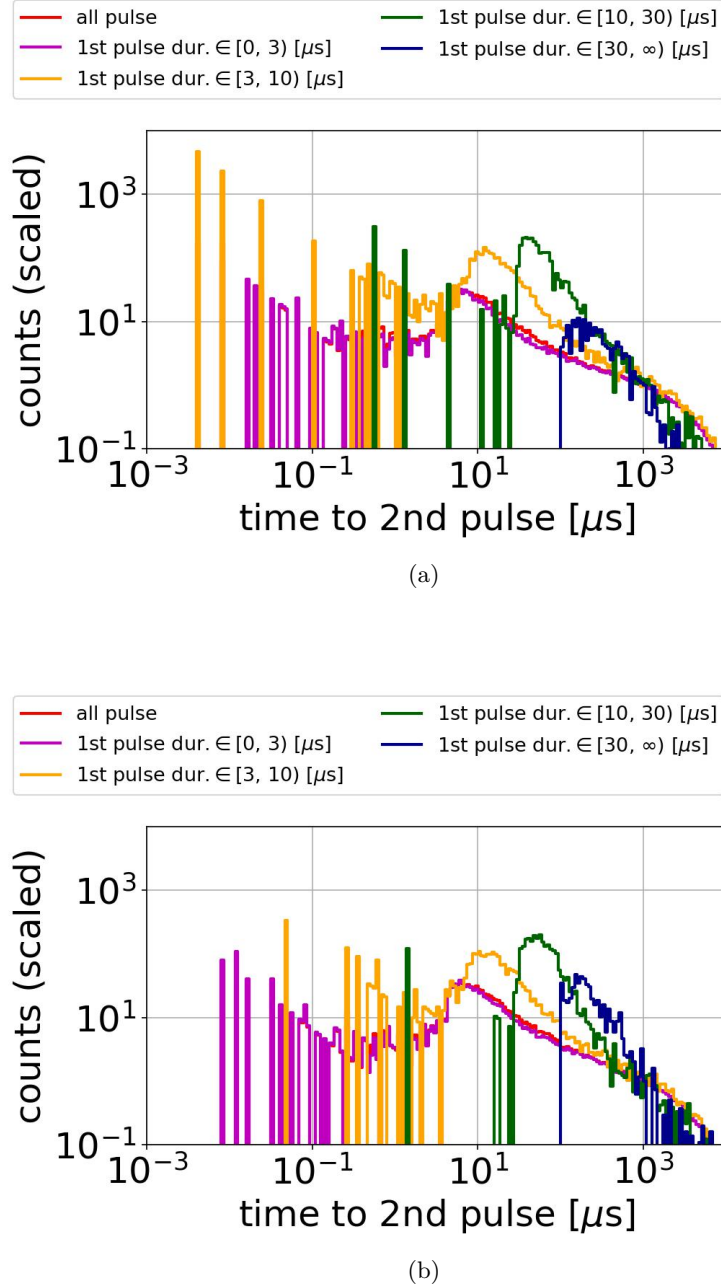


Figure 1.4: Distribution of PMT time differences between pulses in one PMT: (a) top PMT; (b) bottom PMT.

372 5 mm and wire diameter $75 \mu\text{m}$, this correspond to an average wire surface electric field in the range
373 of 65 kV cm^{-1} to 110 kV cm^{-1} . However, since EL yield decreases as the reduced electric field (ratio
374 of electric field to gas density) in the EL region decreases, the photon yield per electron emission
375 is smaller for a lower ΔV_{T-B} . This prevents us to have enough sensitivities for electron emission
376 for a lower operating voltage and wire surface electric field . So electron emission rate for a lower
377 wire surface electric field is measured at a lower gas density to get an increasing on the reduced
378 electric field, which leads to a higher the EL photon production in gas. The dependence of EL light
379 production on reduced electric field is described in Section 1.8.

380 Two PMTs normally operate at -1.5 kV . This guarantees both PMTs having enough gain and
381 signal to noise ratio. Before safely turning on the PMTs to measure the light emission from the
382 grids, a series of sparking tests are done to figure out the high voltage behavior and high voltage
383 weak points in the system. Improvements are done to improve the maximum grid voltages V_T and
384 V_B . These improvements include cleaning the surface of discharging spots, increasing the smooth-
385 ness and rounding radius on the corner of metal surfaces, and increasing the discharge distance
386 between electrodes and the ground. Touching grid wires are avoided during these improvements.
387 The maximum grid voltages V_T and V_B that these grids can hold are measured with different gas
388 and different pressures. Dark current of both PMTs in stable running condition are approximately
389 500 Hz to 1000 Hz. Runs with any PMT dark current rate above 2500 Hz are excluded.

390 The high voltage power supply is capable to bias both grids separately in the range of -8 kV to
391 8 kV . The current between the power supply and the grid is monitored to guarantee stable operation
392 of grid bias voltages. An unstable grid biasing usually shows as a spike in the monitored current,
393 and a spike on PMT recording rates. Segments of time with this monitored current unstable are
394 excluded.

395 **Operating data taking** The most common operating voltage pairs we choose for electron emission
396 measurement at xenon gas density 0.137 mol L^{-1} are $V_T = -V_B$ at $\pm 4 \text{ kV}$, $\pm 4.5 \text{ kV}$, $\pm 5 \text{ kV}$, $\pm 5.5 \text{ kV}$,
397 $\pm 6 \text{ kV}$, $\pm 6.5 \text{ kV}$, $\pm 7 \text{ kV}$, $\pm 7.5 \text{ kV}$, and $\pm 8 \text{ kV}$. This allows us to measure electron emission rate vs.
398 ΔV_{T-B} curves for most grids we study. Measurements in other conditions are also performed to
399 understand the detector better. However, their results usually are not included for the electron
400 emission studies.

401 The typical duration of data taking is three minutes. An increasing trend of light production is
402 seen during the operations when data taking is longer than three minutes. This is probably from
403 the increasing of EL light production from the more ionized chamber environment and increasing
404 of fluorescence light emission from PTFE reflector cones in the detector. Usually, after each 3 min
405 dataset, high voltage power for both grids are set back to 0 kV and rest for at least 30 s before the
406 next measurement. Data taking at each voltage configuration is handled by using scripts in Ignition
407 slow control software, as described in Ref. [Ignition2018]. This is to make sure data taking is done
408 in a consistent reproducible way.

409 Datasets with the cathodic grid bias voltage > -2.5 kV are explicitly excluded for electron emis-
 410 sion measurements. The reason is because this configuration allows electrons created by external
 411 particle in the cone region drifting to the EL region. These electrons will produce EL light in the
 412 EL region. This could introduce a background for electron emission rate study. The process is
 413 illustrated in Fig. 1.5.

414 1.4 Data processing

415 Data processing is to save the useful information of data by reducing the amount of extraneous
 416 information. This reduces size of analysis works. The useful information of a pulse are characterized
 417 by Reduce Quantities (RQs) of a pulse.

418 The data processing framework include three parts: (1) single pulse processing, (2) coincidence
 419 event building and coincidence pulse processing, and (3) random segment sampling of the dataset.

420 This section explains the main part of data processing framework. It does not mean to explain
 421 all the RQs that have been computed. A full documentation of the RQs used in *Gas Test* analysis
 422 is summarized in Appendix. A.

423 **Single pulse processing** A single pulse of digitization, POD, is defined to be the individual pulse
 424 recorded by DAQ system in only one PMT channel. Two steps are done for this processing: (1)
 425 waveform reconstruction, and (2) pulse shape characterization.

426 The waveform is reconstructed with the following method. First, the baseline voltage of the pulse
 427 (RQ name: ‘baselines’) is found from the average DC voltages of the pulse of the first 10 samples.
 428 The baseline voltage represents the voltage at the time when the pulse is recorded assuming no pulse
 429 occurs. Samples used for baseline finding are 80 ns ahead the trigger time of the pulse. Therefore,
 430 these samples provide a reliable measure of the baseline since they are close in time with the rest
 431 of the pulse and unaffected by the rest of the pulse. There are some smaller fluctuation of baseline
 432 voltages for both PMTs. The amplitude of fluctuation ~ 0.36 mV is very small comparing to SPHE
 433 pulse amplitude, which is 15 mV to 35 mV. After baseline finding, the baseline value was subtracted
 434 from the digitized data to get the waveform for the pulse. The waveform is then scaled back from
 435 ADC counts to mV to get the reconstructed waveforms. Along this process, RQs for the voltage of
 436 the trigger sample (RQ name: ‘trigvals’), the voltage of the first sample (RQ name: ‘firstvals’) are
 437 also calculated.

438 From the reconstructed waveform, the maximum positive amplitudes(RQ name: ‘waveampli-
 439 tudes’) and the pulse area (RQ name: ‘waveareas’), which is the time integral of the pulse amplitude
 440 are calculated. However, because of the long post-delay duration ($2 \mu\text{s}$, 500 sample) from the DAQ
 441 pulse recording, baseline fluctuation during the post-delay era is included in the total time integral
 442 of the pulse area. This biases our understanding of pulse area. Thus, another revised pulse area RQ

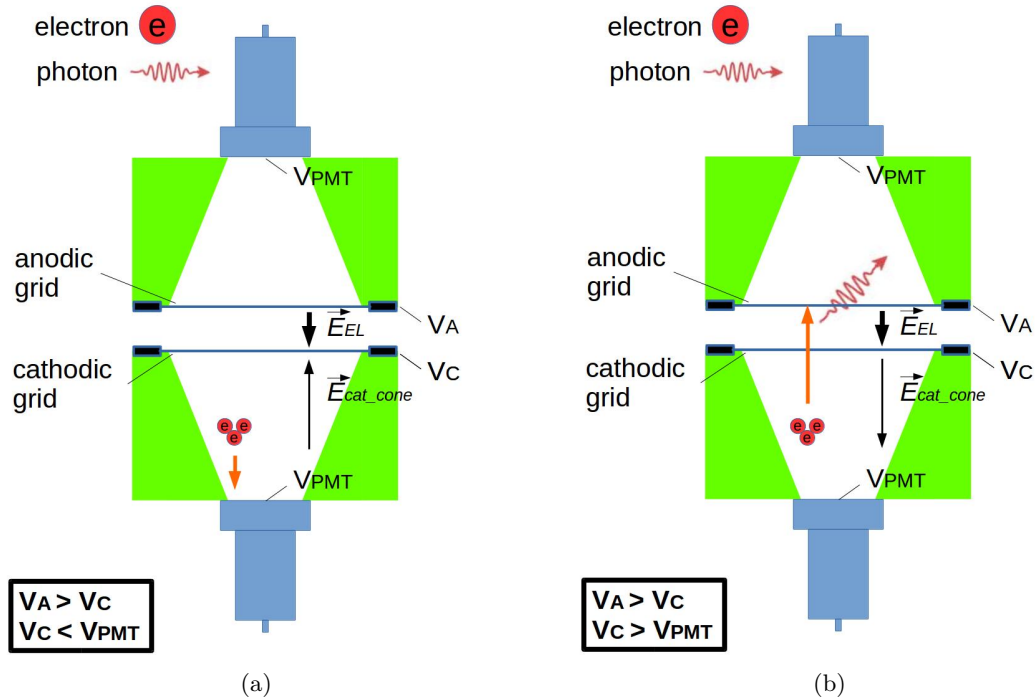


Figure 1.5: (a) Good configuration ($V_C < V_{PMT}$): drift fields pointing from PMT to the grids. Electrons created in the cone region will drift to PMT. This process does not create numerous photons as electron emission signal. (b) Bad configuration ($V_C > V_{PMT}$): drift fields pointing from grids to the PMT. Electrons created in the cone region will drift to EL region. This process creates plenty of EL photons which could look like an electron emission signal.

443 (RQ name: ‘waveareas.trim.end’) is calculated from integrating the waveform with removing the
 444 last $1.8\ \mu\text{s}$, 450 sample from the end of the waveform. This revised pulse area RQ is used in main
 445 analysis instead for PMT pulse area calibrations.

446 Series of pulse shaping parameters are also calculated. Time weighted integral of waveform (RQ
 447 name: ‘wtimeN’) is used to study the skew and kurtosis of the pulse. Also, time difference between
 448 the start time of the pulse and time that the 90th percentile of the pulse waveform are calculated.
 449 They are the characteristic time differences of the pulse (RQ name: aft_tXX). They are very useful
 450 for understanding the pulse shape, pulse duration, and pulse center of mass. These help pulse
 451 selection and classification discussed in the following sections.

452 **Coincidence event building and coincidence pulse processing** The DAQ system records
 453 pulses in each PMT channel independently. A true electron emission signal usually can produce
 454 enough quantity of photons to be recorded by both PMTs. RQs of coincidence pulses between two
 455 PMTs contain more useful information for electron emission signals. So, for each dataset we take,
 456 we do a coincidence event building and a coincidence event processing to help us separating electron
 457 emission signals from other background events, such as dark currents in one PMT.

458 The coincidence event building is done with the following method, requiring records in both
 459 PMTs within a short period of time. The PODs are grouped in a pending searching, which is not
 460 just two but all PODs that are recorded close in time are grouped together.

461 First, a POD time subtraction is done to preserve only the useful part of the POD signal. For all
 462 single PODs, two segments of time were subtracted from the beginning and end of a POD to reduce
 463 the influence from the baseline fluctuation in the PMT. The default values for post-POD subtraction
 464 and pre-POD subtraction is 1800 ns (450 sample) and 0 ns (0 sample). The time subtraction preserves
 465 120 ns before the first pre-threshold crossing time, and 200 ns after the last post-threshold crossing
 466 time, where between the two crossing time is the signal dominant time period. Now, this beginning
 467 and ending time of the remained part of the POD is called the start (t_{start}) and the stop time (t_{stop})
 468 of the POD.

469 Second, a POD searching is performed between a certain segment of time before the start of
 470 a single POD and the same amount of time after the stop time of the POD. The value of ad-
 471 ditional segments of time looking for coincidence is coincidence window width (CWW, RQ name
 472 ‘window_width’). The value of CWW for this analysis is $1.7\ \mu\text{s}$, if not otherwise specified. If no
 473 other pulse is found in this time region, no coincidence is found for this particular single POD. If
 474 another pulse is found in this time region, we say these two pulses are connected.

475 Third, we group all connected pulses to form undividable coincidence pulse groups. A coincidence
 476 pulse group contains all pulses that are connected to any element in the group, and cannot be divided
 477 to subgroups that match the same criterion.

478 Then, we check whether the coincidence pulse group contains PODs from both PMTs. If so, we
 479 determine a coincidence event building is successful.

480 Last, we characterize coincidence pulse RQs from forming coincidence pulse waveforms. A co-
 481 incidence pulse waveform is defined as the addition of normalized pulse waveforms in each channel.
 482 The normalization is done by dividing the pulse waveform amplitude by the SPHE pulse area in
 483 that channel. A similar pulse characterization is performed for the coincidence pulses as in single
 484 POD processing.

485 Coincidence pulse RQs are the fundamental parameters for electron emission signal analysis
 486 framework, which will be described later. Some commonly used coincidence pulse RQs are listed
 487 below. They are

- 488 • coincidence pulse area: RQ name ‘coin_pulse_areas_norm’, pulse area of coincidence pulse,
 489 measured in phe.
- 490 • t_{XX} : RQ name ‘coin_pulse_areas_tXX’, time difference between the start of the coincidence
 491 pulse and integrated pulse area reach XX % of the total coincidence pulse area, measured in
 492 ns. XX = 01, 05, 10, 15, 25, 50, 75, 85, 90, 95, 99.
- 493 • signal t_{01-99} duration (t_{01-99}): $t_{99} - t_{01}$.
- 494 • signal t_{10-90} duration (t_{10-90}): $t_{90} - t_{10}$.
- 495 • signal t_{25-75} width (t_{25-75}): $t_{75} - t_{25}$.
- 496 • signal t_{50} width (t_{50}).
- 497 • top-bottom asymmetry (TBA): TBA $\equiv (T-B)/(T+B)$, where T is the pulse area in the top
 498 PMT; and B is the pulse area in the bottom PMT.

499 **Random segment sampling** The event rates are checked by looking at pulses around a random
 500 sample of times during the operation. In each dataset, 10,000 random times are chosen. From each
 501 random time, total pulse area in the preceding and the succeeding 10 μ s, 20 μ s, 50 μ s, and 100 μ s
 502 windows are calculated. These values of random sampling represent the average photon density
 503 in the detector in this dataset. They are compared to other segments of time of interest to study
 504 correlation light production.

505 1.5 PMT Calibration

506 PMT calibrations are performed for understanding the trigger efficiency, pulse amplitude, and pulse
 507 area of a SPHE for each PMT. SPHE trigger efficiency of a PMT, the probability of SPHE signal
 508 recording, determines the event recording efficiency. SPHE pulse amplitude of a PMT determines
 509 the capability of DAQ to record the full height of a sized pulse. SPHE pulse area of a PMT is the

510 fraction denominator we use to calculate the counts of photon electrons in each pulse. Counts of
 511 photoelectrons in each pulse are roughly estimated by,

$$\# \text{ photoelectrons in a pulse [phe]} \sim \frac{\text{total pulse area}}{\text{single photon electron pulse area}} \quad (1.2)$$

512 Datasets that are used in the calibration are taken at vacuum and grid voltages V_T and V_B at
 513 0 kV. The detector in this condition will have the minimum influence from events from internal and
 514 external sources. Thus, a cleaner population of SPHE can be selected.

515 **PMT trigger efficiency** PMT trigger efficiency is estimated by comparing its trigger voltage
 516 (pre-threshold voltage) to its SPHE amplitude distribution. A simple Gaussian distribution is used
 517 to represent the distribution of SPHE amplitude. A fit range in the pulse amplitude of is chosen to
 518 avoid the influence from noise and overlapping of multiple photo electrons. The fit range is 12 mV to
 519 28 mV for the top PMT, and 22 mV to 38 mV for the bottom PMT. The range choices are $\sim \pm 8$ mV
 520 from the center peak values of the SPHE pulse amplitude. The trigger voltage of each PMT is
 521 compared to the survival function (complementary cumulative distribution function) of the fitted
 522 Gaussian distribution to get the trigger efficiency. Results of curve fittings are shown in Fig. 1.6.
 523 The figures show a close to unity trigger efficiency of both PMTs.

524 **PMT SPHE pulse area** PMT SPHE pulse area is calibrated with fitting the pulse amplitude
 525 and integrated area to a two dimensional Gaussian distribution. A fit range in the pulse amplitude
 526 and area is chosen to avoid the influence from noise and overlapping of multiple photo electrons
 527 this time. The fit ranges are 12 mV to 28 mV, 0 mV ns to 800 mV ns for the top PMT, and 22 mV to
 528 38 mV, 0 mV ns to 1000 mV ns for the bottom PMT. These chosen ranges contain the SPHE peaks
 529 of particular PMTs ,which is identified as the brightest feature above the noise and attributed to
 530 dark current. The used fitting function is,

$$z = A \exp \left(- \left(\frac{1}{2\sigma_x^2} ((x - \mu_x) \cos \theta - (y - \mu_y) \sin \theta)^2 + \frac{1}{2\sigma_y^2} ((x - \mu_x) \sin \theta + (y - \mu_y) \cos \theta)^2 \right) \right) \quad (1.3)$$

531 where x is the pulse area;
 532 y is the pulse amplitude;
 533 z is the total counts at each pulse area and amplitude, represented in the color scale;
 534 A is the amplitude of the fit;
 535 μ_x is the position of the center of the peak on x axis;
 536 σ_x is the standard deviation on rotated x axis;
 537 μ_y is the position of the center of the peak on y axis;
 538 σ_y is the standard deviation on rotated y axis;

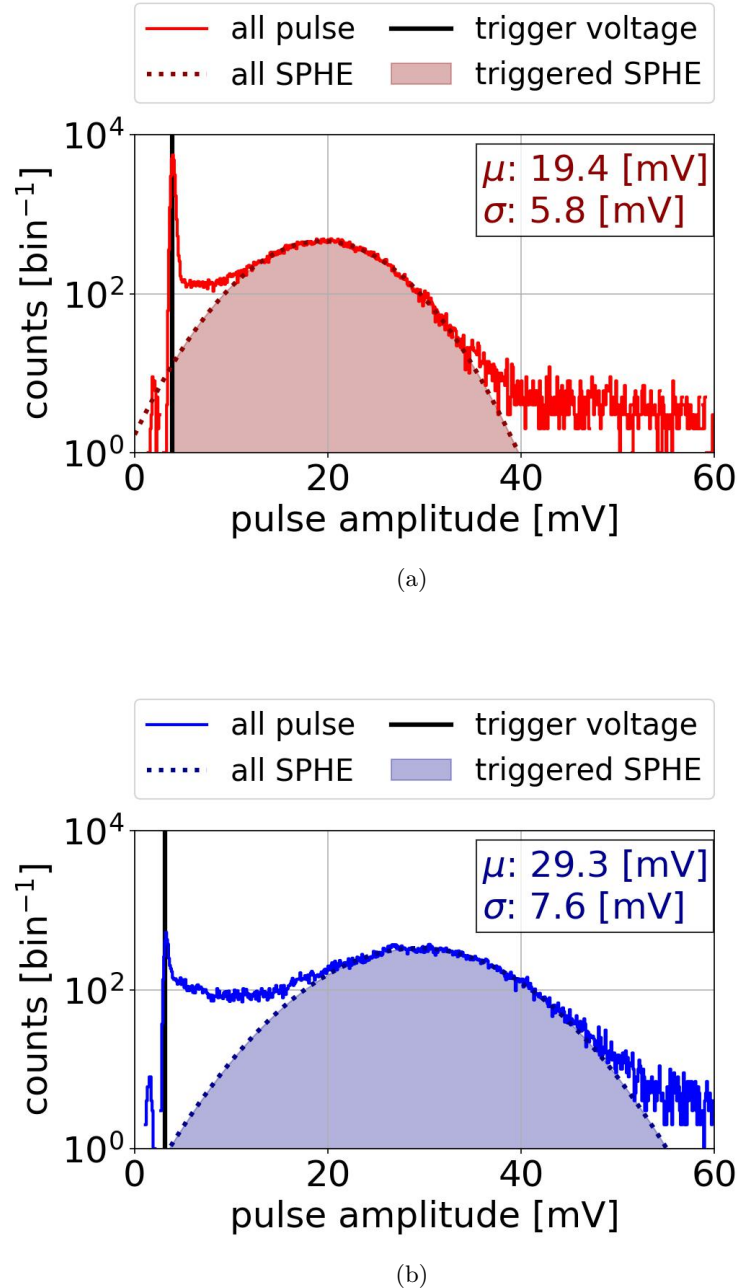


Figure 1.6: PMT pulse amplitude distribution: (a) top PMT (b) bottom PMT. Data were taken at 2018-03-12 11:41.

539 and θ is the rotated angle.

540 The mean values for pulse area and pulse amplitude are μ_x and μ_y . The standard deviation
 541 values for pulse area and pulse amplitude are $\sigma_x \cos \theta - \sigma_y \sin \theta$ and $\sigma_x \sin \theta + \sigma_y \cos \theta$. Results of
 542 these fits are shown in Fig. 1.7. Results from PMT calibrations are summarized in Table 1.4. Fitting
 543 values of different dataset show an agreement within 1 % on the mean PMT single photon electron
 544 pulse area and pulse amplitude.

545 The values of SPHE pulse amplitudes are approximately 20 mV for the top PMT and 30 mV for
 546 the bottom. Thus, a naive estimation based on the dynamic range 1260 mV noted previously shows
 547 the DAQ system allows approximately 60 SPHEs to be simultaneously recorded by the top PMT
 548 without distortion of pulse shape, and 40 for the bottom PMT. This dynamic simultaneous photon
 549 recording range is large enough for record electron emission signal without pulse shape distortion in
 550 most situations.

551 Degrading of PMTs is not noticed during the run, even though the possibility of degrading of
 552 PMTs is discussed in their manual (Ref. [1]). However, since this effect is not observed during the
 553 tests. For consistency of studying, the same value for PMT SPHE pulse area is used through all the
 554 studies.

555 There are two revisions of these values of SPHE pulse area. In revision 1 (Rev1), the values used
 556 are 426 mV ns for the top PMT and 638 mV ns for the bottom PMT. This is from analyzing pulse
 557 area on datasets taken with the detector filled with xenon gas and grid voltages V_T and V_B higher
 558 than 0 kV. These datasets contains more multiple photon electron pulses and biased the estimation.
 559 In revision 2 (Rev2), data taken at vacuum condition with grid voltages V_T and V_B at 0 kV are used.
 560 The values used are 413 mV ns for the top PMT and 610 mV ns for the bottom PMT. Rev2 gives a
 561 better estimation on SPHE pulse area. SPHE pulse area is noted as PHE below.

time	PMT name	trigger voltage [mV]	trigger efficiency	pulse amplitude [mV]	pulse area [mV ns]
2018-02-3 13:21	top	3.762	0.997	19.4 ± 3.3	413 ± 132
	bottom	3.103	1.000	27.9 ± 4.6	607 ± 161
2018-03-12 11:41	top	3.853	0.996	19.3 ± 3.5	411 ± 130
	bottom	3.130	1.000	29.2 ± 5.1	607 ± 161
2018-05-15 12:03	top	3.713	0.997	19.4 ± 3.5	413 ± 131
	bottom	3.091	1.000	29.5 ± 5.4	615 ± 167
adopted value (Rev1)	top	-	1	-	426
	bottom	-	1	-	638
adopted value (Rev2)	top	-	1	-	413
	bottom	-	1	-	610

Table 1.4: PMT SPHE calibration.

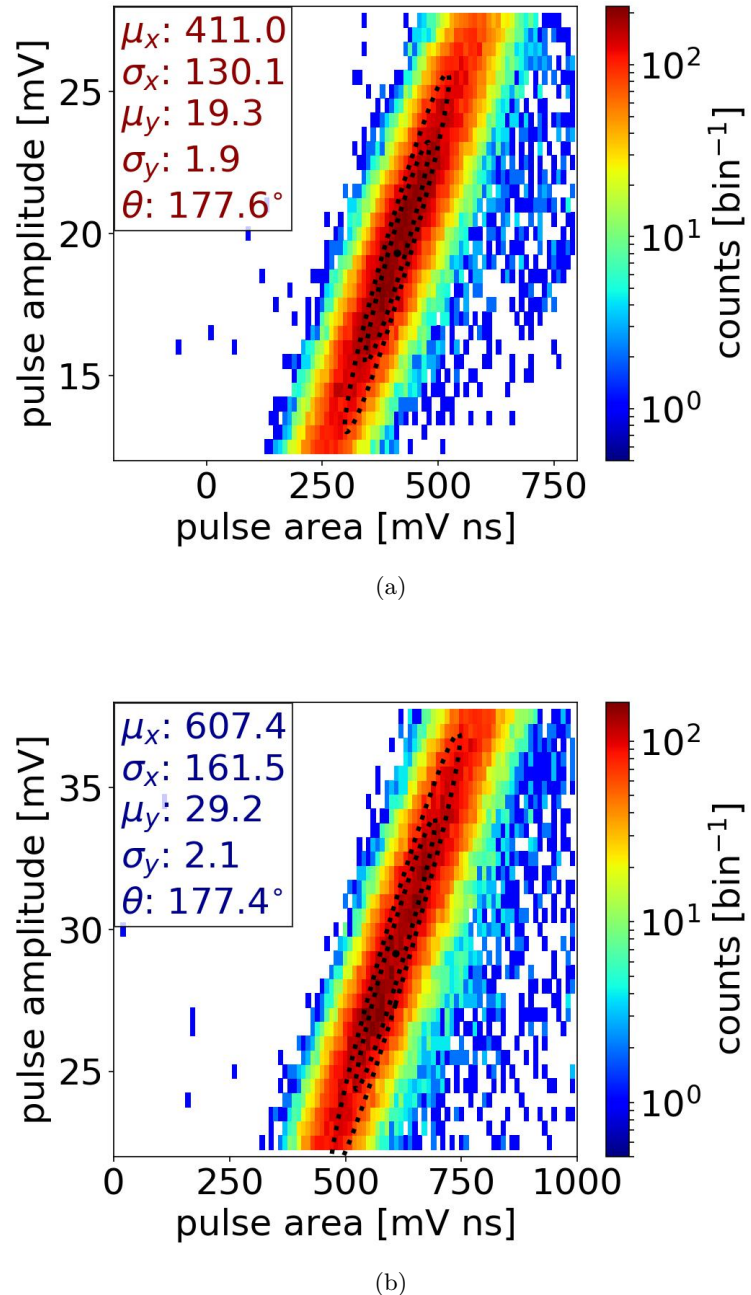


Figure 1.7: PMT SPHE pulse amplitude vs. pulse area distribution: (a) top PMT (b) bottom PMT. The black dot, and the dashed line are mean, 68 %, and 95 % contours of the Gaussian fits. Data were taken at 2018-03-12 11:41.

562 1.6 Light Collection

563 *Gas Test* studies event-based primary scintillation light and EL light. Light collection efficiency is
 564 important to understand the overall sensitivity of the detector.

$$\text{light collection efficiency} = \frac{\# \text{ photoelectrons observed for an event}}{\# \text{ photon created during an event}} \quad (1.4)$$

565 Light collection efficiency includes geometric collection efficiency and PMT overall quantum effi-
 566 ciency. Geometric collection efficiency describes the efficiency of photon propagation to reach PMT
 567 photocathode surfaces, which includes photon propagation in the gas medium, photon reflection by
 568 the detector material surfaces, and photon propagation in PMT window materials. PMT overall
 569 quantum efficiency describes the efficiency of how many photons are absorbed by the photocathode
 570 surfaces and turn into measurable current or voltage signals.

571 **Geometric collection efficiency** Geometric collection efficiency is studied by photon propaga-
 572 tion simulation software Light Guide, as described in Ref. [5]. In the simulation software, a simplified
 573 *Gas Test* detector boundary with cylindrical symmetry is drawn to represent the real detector ma-
 574 terial surfaces. This simplified geometry includes the photocathode surfaces of PMTs, inner surfaces
 575 of the PTFE cones, and surfaces of the grid rings. In addition, each grid is represented by two
 576 planes of parallel wires with the same diameter and the same pitch distance as in the real detector.
 577 The two planes are parallel to each other and close in distance to represent two distinct sets of
 578 wires interlacing each other. Photon absorption and reflection, which takes into account the proba-
 579 bility of specular reflection and Lambertian diffusion reflection, are simulated at material surfaces.
 580 The empty space inside the simplified detector geometry is filled with a transparent or translu-
 581 cent medium. The simulation of photon propagation through the medium includes scattering and
 582 absorption effects.

583 The uncertainty of the reflectivity of detector surface materials has a major influence on the total
 584 light collection. Among these materials, PTFE reflectivity has the largest uncertainty reported, the
 585 value of which for xenon scintillation photons at room temperature are in the range of 0.4 to 0.75.
 586 This difference in reflectivity may be a result of different fabrication processes or different material
 587 density, as discussed in Ref. [6].

588 The geometric collection efficiency is evaluated as a function of (r, z) in the detector. To under-
 589 stand geometric collection efficiency at one specific location, 10^5 to 10^7 simulations of single photons
 590 are generated from this specific location. Each simulated photon is stepped either to transport
 591 through the detector medium or to interact with the detector surface materials. Each simulation
 592 ends when the simulated photon is absorbed by either the detector medium or detector surface ma-
 593 terials. The counts of photons reaching PMT photocathode surfaces are used to estimate geometric

594 collection efficiency,

$$\text{Geometric collection efficiency} = \frac{\# \text{ photons reaching PMT photocathode surfaces}}{\# \text{ photons simulated}} \quad (1.5)$$

595 **PMT overall quantum efficiency** The overall quantum efficiency of a PMT includes (1) the
596 PMT photocathode quantum efficiency (QE), (2) the PMT electron collection efficiency, and (3) the
597 PMT electron gain.

598 The PMT photocathode QE is the probability per incident photon to produce a photoelectron.
599 For 175 nm xenon scintillation light, there is a \sim 20 % probability for 2 photoelectrons to be produced
600 rather one, so called the double photoelectron effect. We use the term photons detected (PHD) to
601 refer to the number of photons that produced at least one photoelectron. The term PHE refers to
602 the number of photoelectrons produced at the photocathode. The photocathode quantum efficiency
603 for the top and bottom PMTs, as quoted by Hamamatsu, are 36.3 % and 36.0 %, respectively, for
604 175 nm light, see Table 1.1. The Hamamatsu QE does not account for the double photoelectron
605 effect; that is, it is the average number of photoelectrons produced per incident photon, different
606 from the average number of photons that produce a measurable signal per incident photon.

607 PMT electron collection efficiency is the probability that these output photoelectrons land on the
608 effective area of the first dynode; the mechanism of how the PMT works is described in Section 1.1.
609 PMT electron collection efficiency depends on the mechanical design of a PMT and the voltage
610 difference between the PMT photocathode and the PMT first dynode. The exact value of electron
611 collection efficiency of the PMTs used in *Gas Test* at their operating voltage are not measured. We
612 estimate PMT electron collection efficiency to be 90 % based on measurement of other PMTs of the
613 same model at a higher PMT operating voltage, as described in Ref. [Lung2012].

614 PMT electron gain describes the multiplication process of the output photoelectrons in dynode
615 stages. The current that results from this multiplication process is translated to voltage using a
616 50Ω load resistor. The multiplication process amplifies the useful signal and eases the signal noise
617 selection. The voltage then is digitized by the DAQ, as described in Section 1.2. The digitized
618 voltage is the measured PMT signals. Observed signals are translated to units of PHE by dividing
619 out the mean SPHE area for each PMT. The coefficient of variation (CV, the ratio of the standard
620 deviation to the mean value) of PHE is \sim 30 %, as described in Section 1.5.

621 Therefore, to understand the spatial dependence of light collection efficiency in the ELD, we
622 start with 500 000 simulations of single photons every 5 mm in r and z dimension in the ELD, and
623 record the geometric collection efficiency of each location. This number is then multiplied by PMT
624 overall QE to obtain the total light collection efficiency. There are two light collection efficiency
625 estimation of two different grid wire configurations that we used for grid emission tests, labeled
626 grid configuration 1 (grid config. 1) and grid configuration 2 (grid config. 2). Run 4 to Run 9 use
627 grid configuration 1, and Run 10 to Run 17 use grid configuration 2. These two configurations are

628 identical everywhere else in the ELD except for the top grid wire pitches and diameters. Table 1.5
 629 and Table 1.6 summarize the parameters in the simulation.

parameter	grid config. 1 Run 4-9	grid config. 2 Run 10-17
top grid	wire pitch [mm] wire diameter [μm]	2.5 100
bottom grid	wire pitch [mm] wire diameter [μm]	2.5 75
top/bottom cone (PTFE reflector)	cylinder 1 height [mm] cylinder 1 radius (frustum larger radius) [mm] frustum height [mm] cylinder 2 radius (frustum smaller radius) [mm] cylinder 2 height [mm]	1.17 65 98.8 32 10
top/bottom PMT	photocathode radius [mm]	32

Table 1.5: Light collection simulation geometry parameters

parameter	value
Xe (gas)	refraction index
	Rayleigh scatter length [m]
	absorption length [m]
Quartz (synthetic quartz)	refraction index
PTFE	reflectivity
	specular reflection ratio
	Lambretian diffusion reflection ratio
SS (SS304)	reflectivity
	specular reflection ratio
	Lambretian diffusion reflection ratio

Table 1.6: Light collection simulation material parameters

630 As expected, the geometric collection efficiency varies at different locations in the ELD, which
 631 causes the light collection efficiency to vary, accordingly. The light distribution between the top
 632 and bottom PMT also varies across the ELD. This light distribution helps discriminate the location
 633 where events happened. We use top-bottom asymmetry (TBA) to describe this light distribution,
 634 which is defined as:

$$\text{TBA} = \frac{\text{Top PMT light collection} - \text{Bottom PMT light collection}}{\text{Top PMT light collection} + \text{Bottom PMT light collection}}. \quad (1.6)$$

635 Results in Fig. 1.8 show the light collection efficiency and the TBA in the ELD. Locations that
 636 are in the top cone region usually have a positive TBA, and locations that are in the bottom cone

637 usually have a negative TBA. TBA is close to zero in the EL region.

638 Among all different classes of events, our primary pulse of interest is electron emission events,
639 which happen in the EL region. We estimate the light collection in this region with the same method
640 mentioned before and finer binning. We start with 500 000 simulations of single photons every 2 mm
641 in r dimension in the middle of the EL region. Results of the simulations are shown in Fig. 1.9.
642 Light collection efficiency in the EL region falls away at $r > 65$ mm, which is the inner radius of the
643 PTFE reflector cones. The average top and bottom PMT light collection efficiencies in the EL region
644 are ~ 0.0085 . The average TBA in the EL region is ~ 0 . The average total PMT light collection
645 efficiency in the EL region is ~ 0.017 . For most electron emission events in which photon production
646 is larger than 300, an average number of ~ 5 photoelectrons would be observed. Therefore, this light
647 collection efficiency is sufficient to allow us to detect electron emission events.

648 The uncertainty of PTFE reflectivity has a large influence on the total light collection, which is
649 shown in Fig. 1.10. Higher PTFE reflectivity results in a higher total light collection efficiency. The
650 actual value of reflectivity of the PTFE reflector cones has not been measured directly. We estimate
651 the actual PTFE reflectivity of xenon scintillation photons to be 0.4, according to the material
652 density .

653 1.7 Light production

654 The ELD measures primary scintillation photons and electroluminescence photons in gas. First, I
655 will introduce these two light production processes. Next, I will discuss the light production in noble
656 gas, e.g. xenon, which is the medium that the ELD normally operates in.

657 **Primary scintillation** Primary scintillation is the process in which photons are created directly by
658 energy deposition of external particle events. These photons have two sources: direct excitation, and
659 excitation from recombination after ionization. An external particle travels through the medium in
660 the ELD, transferring its energy to atoms in the medium, e.g. xenon, through exciting and ionizing
661 these atoms. The excited atoms will return to their ground states by emitting photons of series
662 energies corresponding to the energy level of the atoms, which is called relaxation of the excited
663 atom. These photons from direct excitation from external particles are the first source of primary
664 scintillation photons. The ionized atoms are not able to produce photons by themselves. However,
665 they can recombine with the electrons around them and form excited atoms, which deexcite in a
666 similar process as direct excited atoms, and emit photons simultaneously. These photons are the
667 second source of primary scintillation photons. The quantity of second source of primary scintillation
668 photons is dependent on the recombination process, which depends on properties of the atoms, and is
669 influenced by the detector environment, especially the electric field (or reduced electric field) on the
670 recombination site. A strong electric field forces electrons to quickly drift away from the ionization

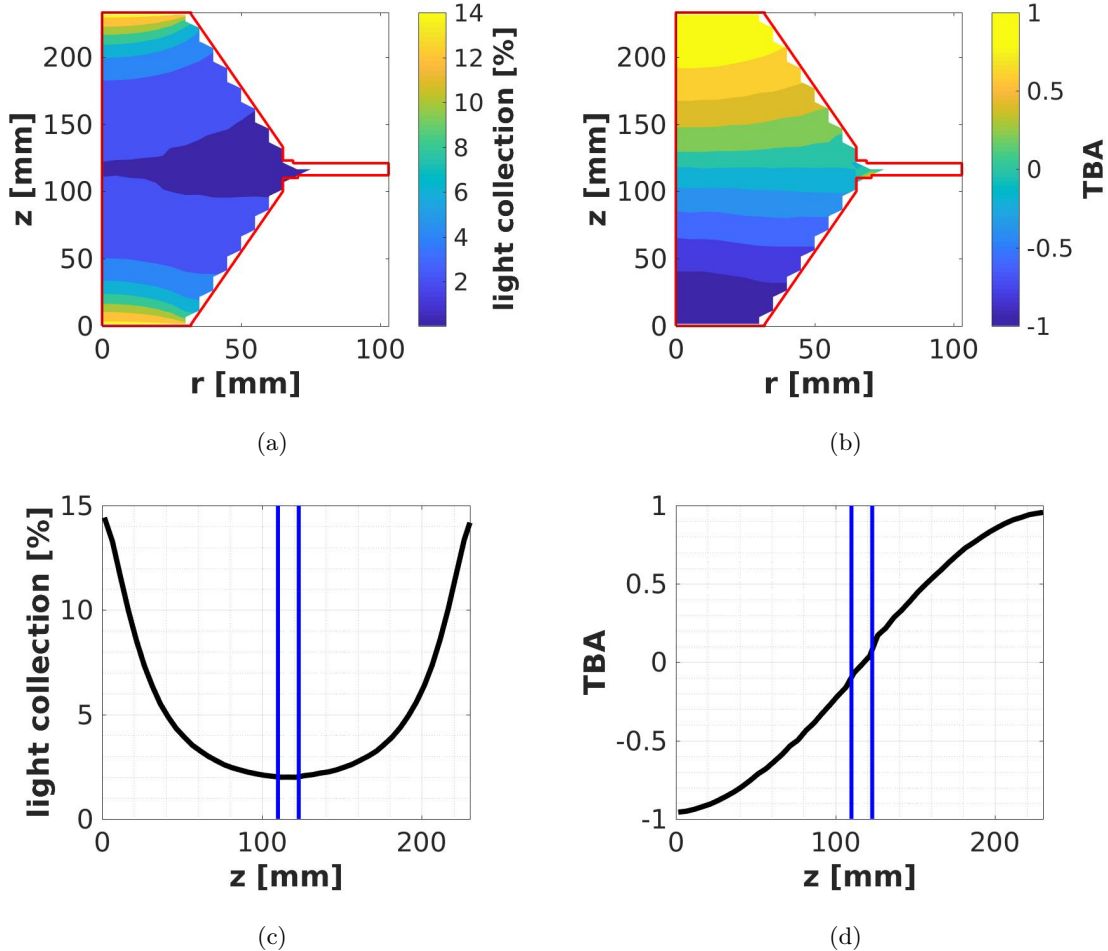


Figure 1.8: Light collection efficiency of (r, z) cross section in the ELD from simulation. (a) Total light collection efficiency. (b) Top-bottom asymmetry (TBA). (c) Total light collection efficiency at $r=0$. (d) TBA at $r=0$. The red solid curve is the edge of the active volume of the ELD. The blue solid curve is the edges of the EL region. This result uses configuration 1, PTFE reflectivity 0.40. $z=0$ is at the bottom PMT photocathode surface.

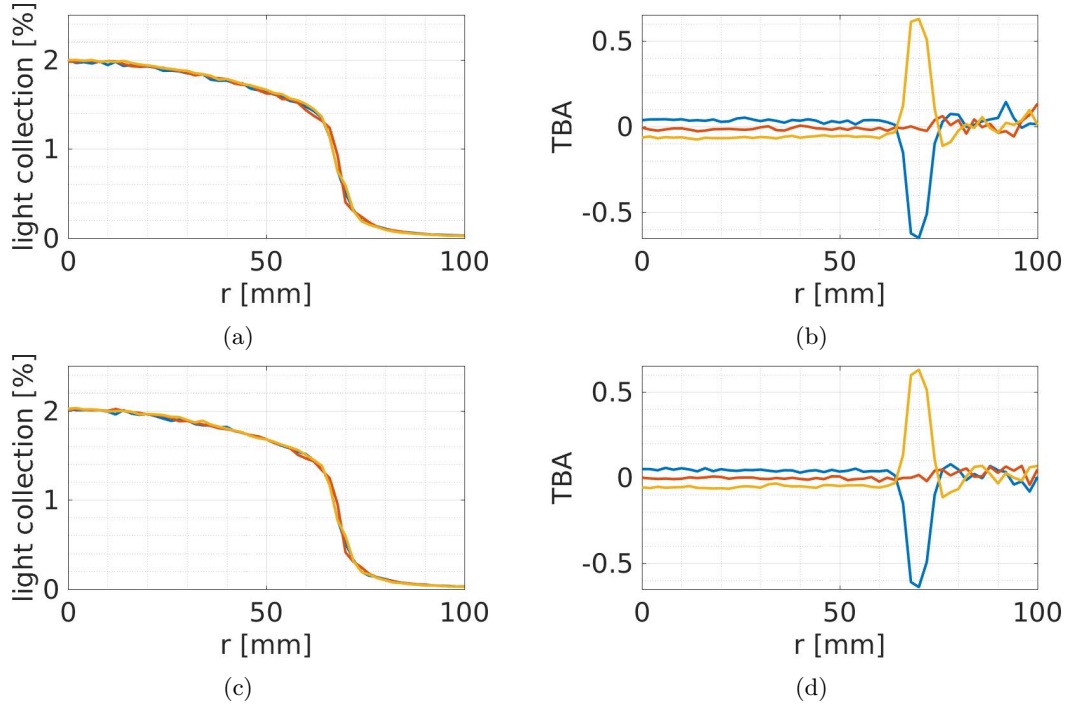


Figure 1.9: Light collection efficiency and TBA in the EL region in different grid configurations from simulation. (a) Total light collection efficiency in grid configuration 1. (b) TBA in grid configuration 1. (c) Total light collection efficiency in grid configuration 2. (d) TBA in grid configuration 2. The blue curve shows the value (light collection efficiency or TBA) as a function of r for fixed 2.09 mm below the top grid. The yellow curve shows the value as a function of r for fixed 2.09 mm above the bottom grid. The red curve shows the value as a function of r at the midpoint between the top and bottom grids. Light collection efficiency decreases and TBA has a sharp feature at $r=65$ mm, which is the inner diameter of the PTFE reflector cones. This result uses PTFE reflectivity 0.40.

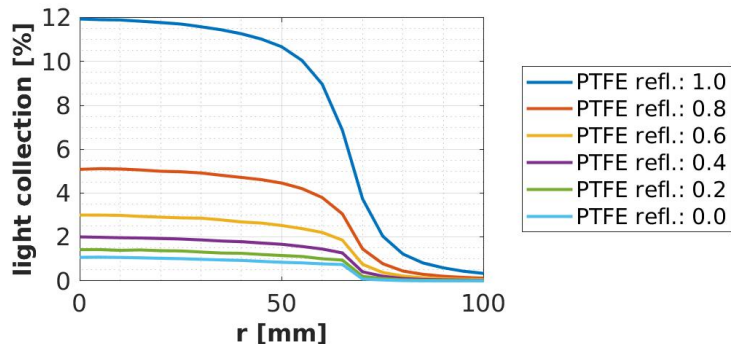


Figure 1.10: Light collection efficiency in the EL region with different PTFE reflectivity from simulation. Light collection efficiency decreases at $r = 65$ mm, which is the inner diameter of the PTFE reflector cones. This result uses grid configuration 1.

671 site and reduce the probability of recombination, thus reducing the quantity of primary scintillation
 672 light production.

673 **Electroluminescence** Electroluminescence (EL) is a phenomenon in which an electron drifts
 674 through a strong electric field in a medium, collides with atoms in the medium, excites them which
 675 will afterwards emit scintillation light. Since EL process is related to electrons in the medium, we
 676 measure EL photons to study the electron production in the detector. The mechanism of EL is
 677 similar to primary scintillation; the electron gains energy from drifting through the strong electric
 678 field and simultaneously loses energy though exciting and ionizing medium atoms. Moreover, the
 679 ionization process are usually associated with electron multiplication (gas gain), which creates more
 680 electrons in the strong electric field region, and produces more EL scintillation light. The quantity of
 681 EL scintillation photons and the probability of electron multiplication, are related to the strength of
 682 reduced electric field of the medium. With proper strength of reduced electric field, EL can produce
 683 more photons than primary scintillation. Because of its association with electrons and its production
 684 quantity, EL photons are the most important signals measured in the ELD.

685 The primary scintillation photons are called S1, and the EL scintillation photons are called S2,
 686 because the primary scintillation photons are produced earlier than the other photons created by
 687 electroluminescence process of uncombined electrons. The same concepts of primary scintillation,
 688 as well as S1 and S2, are also used in liquid noble detectors, as described in Chapter. ??.

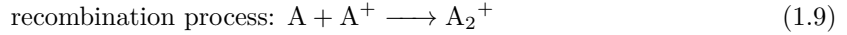
689 **Noble gas scintillation** For most noble gas atoms (A), e.g. neon, argon, krypton, and xenon, the
 690 scintillation process usually forms an intermediate excited excimer state (A_2^*). The emitted photons
 691 from the intermediate excimer state are almost monoenergetic, e.g. 7.1 eV (~ 175 nm) in xenon, which
 692 the medium is transparent to. Because of the existence of the intermediated excited excimer states, it
 693 creates appreciable quantity of monoenergetic photons from the deexcitation of these states. These
 694 features allow us to efficiently collect these monoenergetic photons with specialized devices, e.g.
 695 PMTs, and use these photons to study reactions between external particles and medium atoms.

696 The chemical processes of scintillation are:



697 where A is the noble gas atom; A^* is the noble gas excited state; A_2^* is the excimer state; γ is
 698 the monoenergetic photons from deexcitation of the excimers; and the low energy photons produced
 699 during the process are not shown.

700 The chemical processes of recombination are:



701 where A^+ is the noble gas ionized state; A_2^+ is the ionized dimer state; and the low energy photons
 702 produced during the process are not shown. The recombination process then leads to same channels
 703 as the primary scintillation, with monoenergetic photons as the output signals. These photons,
 704 combined with photons from direct excitations, make primary scintillation light. The quantity of
 705 the monoenergetic photons is related to the reaction energy between external particles and medium
 706 atoms, and properties and physical environment of the medium (especially medium density and
 707 electric field).

708 These two primary scintillation processes happen fast in xenon, the duration of which is dom-
 709 inated by the excimers decay time. The excimers can be separated to two types, the singlet state
 710 (${}^1\sigma_u^+$, ${}^3\sigma_u^+$) and triplet state (${}^3\sigma_u^+$, 1_u), with separate decay times. The singlet state and the
 711 triplet state are known to be created from a three-body deconstruction of noble gas atom excited
 712 state ${}^2P_{1/2}$ state and ${}^2P_{3/2}$ state, which has a different initial quantity from the event. Because
 713 these creation processes are three body reactions, the creation rate of the these two states have
 714 strong dependence on the gas density of atoms. The decay time of both of these two states have
 715 a dependence on the gas density, as described in Ref. [8]. Some other materials also show that the
 716 decay time is very different between liquid noble gas and very dense noble gas. The decay time for
 717 the singlet state and the triplet state in liquid xenon are 4.3(6) ns and 22.0(20) ns, as measured in
 718 Ref. [9]. For dense xenon with pressure in the range of 2.7 atm to 32 atm, the decay time for singlet
 719 states varies from 15(3) ns to 5.5(10) ns. The decay time for triplet state is 96(5) ns in the same
 720 pressure range.

721 **think about should I take about ionization/scintillation ratio here?**

722 EL photons in gaseous xenon from the energy-loss of fast-moving electrons are one of the most
 723 important signals that we measure. This EL process is driven by the electrons gaining energy in the
 724 electric field. This chemical process is,



725 in which a electron directly excite a xenon atom. These excited-state atoms (A^*) then deexcite
 726 through the same chemical process as Eqn.1.7, Eqn.1.8 and emitted EL photons at a similar energy
 727 as scintillation photons.

728 The EL reduce photon production quantity (ratio of photon production quantity to gas density)
 729 per electron trajectory length of direct excitation is found to have a linear dependence on the reduced

⁷³⁰ electric field (E_s/N), as described and summarized in Ref. [Santos1994, Fonseca2004, 10, 11]:

$$\frac{dL_s}{dx} = a \frac{E_s}{N} + b, \quad (1.13)$$

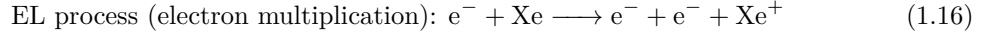
⁷³¹ where L_s is the reduced photon production quantity; x is the electron trajectory length; E_s is
⁷³² the electric field strength (at the scintillation site); N is the density of gas; a and b are constant
⁷³³ parameters, which are measured in Ref. [Fonseca2004, 11] to be:

$$a = 0.137(2) \text{ photon electron}^{-1} \text{ V}^{-1}, \quad (1.14)$$

$$b = -4.7(1) \times 10^{-18} \text{ photon cm}^2 \text{ electron}^{-1} \text{ atom}^{-1}. \quad (1.15)$$

⁷³⁴ The measurement also suggests that EL light is typically not produced below 3.4 Td¹, which is
⁷³⁵ referred as the EL threshold.

⁷³⁶ The EL process is usually associated with simultaneous electron multiplication. This process
⁷³⁷ describes an electric accelerated by electric field, collides with gas molecules, ionize them generating
⁷³⁸ additional free electrons. The chemical process is,



⁷³⁹ The probability of electron multiplication per electron per unit length is also quoted as the first
⁷⁴⁰ Townsend ionization coefficient (α), which depends on the strength of reduced electric field, as mea-
⁷⁴¹ sured in Ref. [Kruithof1940, Derenzo1974]. Conventionally, reduced first Townsend ionization
⁷⁴² coefficient is measured with E/p_0 instead of reduced electric field, where E is the electric field; p_0 is
⁷⁴³ pressure of the gas reduced to 0 °C. The reduced first Townsend ionization coefficient $\eta \equiv \alpha/E$ is also
⁷⁴⁴ frequently used. The measured reduced first Townsend ionization coefficient is shown in Fig. 1.11.

⁷⁴⁵ The duration of EL process is related electron drift velocity (v), which also depends on reduced
⁷⁴⁶ electric field (E/n), as measured in Ref. [English1953, Pack1962, Brooks1982, Berghofer2004,
⁷⁴⁷ 12]. In the range of 5 Td to 25 Td, a naive linear fit from Ref.[Brooks1982] shows in xenon,

$$v [\text{mm } \mu\text{s}^{-1}] \approx 0.556 E/n [\text{Td}] \quad (1.17)$$

⁷⁴⁸ Therefore, xenon is a good scintillation medium for its quantity of photon production and its
⁷⁴⁹ transparency to these photons. With its well characterized quantities, we chose it as the major
⁷⁵⁰ operating medium for the ELD.

¹A Townsend, or Td, is defined as $1 \text{ Td} = 10^{-21} \text{ V m}^2 = 10^{-17} \text{ V cm}^2$.

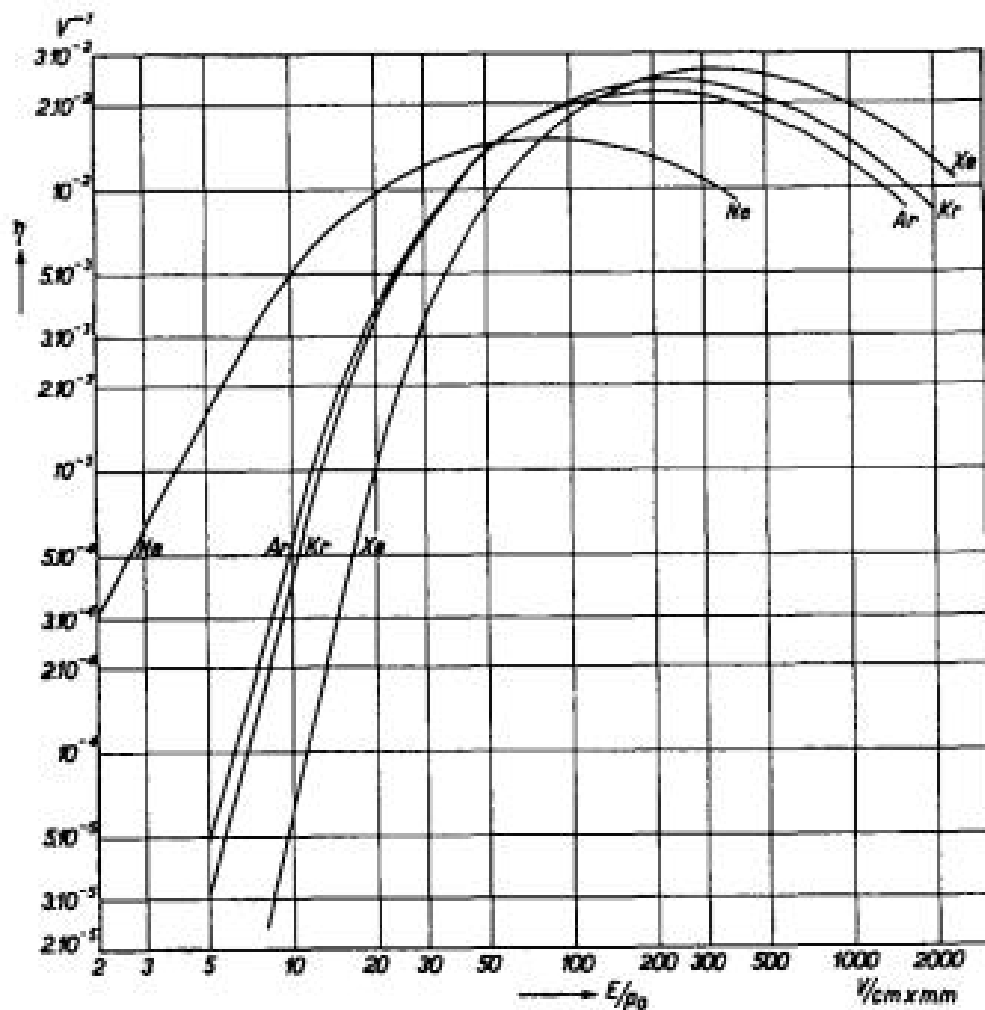


Figure 1.11: The reduced first Townsend ionization coefficient $\eta \equiv \alpha/E$ for neon, argon, krypton, and xenon, from Ref. [Kruithof1940].

751 1.8 Signals

752 Signals, PMT photon pulses that we record, are the fundamental elements of to understand detector
 753 activities. A variety of process can give rise to signals in the detector. Based on their source origin,
 754 signals are separated to four different categories:

- 755 • electron emission (from both the grid wires and grid rings)
- 756 • particle radiation from radioactive materials (both inside and outside the ELD),
- 757 • cosmic ray,
- 758 • and other miscellaneous sources, which includes:
 - 759 – electronic noise (from the electrical ground of the building and other powered devices,
 760 e.g. the KNF circulation pump.)
 - 761 – PMT dark current,
 - 762 – PMT afterpulsing,
 - 763 – PTFE cone reflector fluorescence,
 - 764 – Cherenkov radiation (created in the PTFE cone reflectors and the PMT windows when
 765 a charge particle, most likely an electron or a muon, passes through),
 - 766 – discharge, as in a short-lived plasma in the medium, i.e., breakdown.

767 1.8.1 Electron emission

768 Electron emission signals, especially those from the grid wires, are our signals of interest. A cartoon
 769 for the physical process and an example waveform of electron emission signal are shown in Fig. 1.12.
 770 An electron leaves the cathodic electrode from various types of emission processes. After the elec-
 771 tron left the wire surface, the high electric field around the cathodic wire will quickly energize the
 772 electrons. The high energy electron ionizes and excites the atoms around it. This process in which
 773 more drifted electrons are produced is called electron multiplication; since in this particular case, it
 774 happens near the cathodic electrode, it is also called cathodic gas gain. In this region, more EL light
 775 is produced per unit time compared to a lower electric field region. This is the cause of the “peak”
 776 at the beginning of the electron emission signal. Then, these electrons drift to the anodic electrode
 777 because of the operation voltage difference between the two grids. EL light is produced along this
 778 drift. This correspond to the majority of EL light seen in the electron emission signal. There is a
 779 clear start and stop time for the electron emission signal. Duration of the electron emission signal is
 780 roughly the duration of this drift. After this, drifted electrons get close to the anodic electrode. Since
 781 the electric field around the anodic wires are also high, drifted electrons also go through a similar
 782 electron multiplication process, which is also called anodic gas gain. This process also creates more

783 electrons and a higher production rate of EL light. This is the cause of the “peak” at the ending of
 784 electron emission signal. The peak at the end of the signal is lower than the peak at the beginning of
 785 the signal. This is because of dispersion of the arrival times of drifted electrons on anodic electrode.
 786 This dispersion is because of the different microscopic trajectory each drifted electron takes to reach
 787 the anodic electrode. Different arrival times of the drifted electrons cause the final increment of EL
 788 light production from different electrons do not happen coincidentally. This lowers the height of the
 789 peak at the ending of the electron emission signal. Another reason for the different height of the
 790 peak is because the electric field on the anodic wire is smaller than cathodic wire with regard to the
 791 wire diameter of the anodic wire are larger, thus resulting in a smaller production of EL light.

792 Of the features described above, the most important features of the electron emission signal is
 793 the EL duration. The other signal shape features including the early and late gas gain peaks are not
 794 apparent because the light collection efficiency is not high enough. The EL duration is approximately
 795 equal to the duration of electron drift between the two electrodes. The deviation of electric field
 796 between the two electrode is much smaller than the average value of it. So the drift duration can be
 797 roughly estimated by,

$$\text{drift duration} = \frac{\text{distance between two electrodes}}{\text{drift velocity at the average electric field between two electrodes}} \quad (1.18)$$

798 The other important feature of the electron emission signal is the quantity of its EL production.
 799 EL light production in the majority part of electron emission signal is uniform, except for the
 800 beginning and the ending of the signal. Since the electron multiplication around the cathodic wires
 801 happens early in the process before the major era of EL light production, the total counts of photons
 802 created in an electron emission signal can be estimated as,

$$\# \text{ EL photons} \approx \# \text{ EL photons per drifted electron} \times \text{cathodic gas gain}. \quad (1.19)$$

803 We will estimate the number of EL photons per drifted electron and the cathodic gas gain below.

804 The number of EL photons per drifted electron and the cathodic gas gain are related to the
 805 reduced electric field in the EL region and surface reduced electric field on the cathodic wire. The
 806 value of both reduced electric field can be derived from the gas density and the electric field, which
 807 can be estimated from the operation voltage, wire diameter and wire pitch of the two grid. The
 808 electrostatic solution of the electric field in the ELD is solved by COMSOL, as described in Ap-
 809 pendix ???. The results of the electric fields in the EL region (drift fields) and the average surface
 810 electric fields vs. ΔV_{T-B} are shown in Fig. 1.13a. Because of the grid has a woven pattern, the
 811 surface electric field in the middle of the wire between two woven knots are higher than average
 812 by $\sim 16\%$, which is also discussed in Appendix ???. The average photon yield per EL distance is a
 813 known function of reduced electric field, as discussed in Section 1.7.

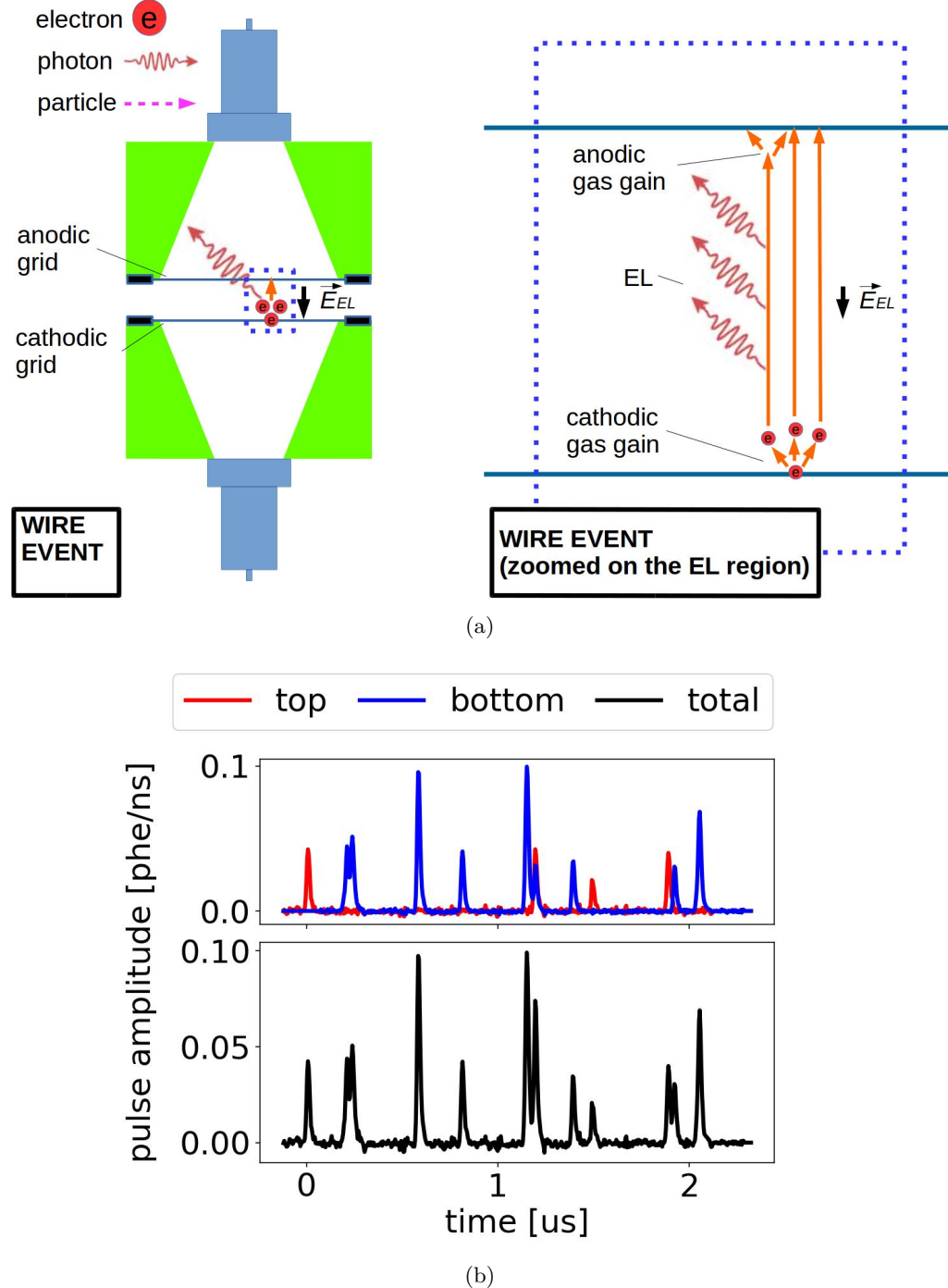


Figure 1.12: *Gas Test* electron emission event from grid wires. (a) Cartoon of the process. (b) An example waveform. Data were taken at 2017-12-8 14:02, with grid voltages V_T and V_B at +6 kV and -6 kV, operating gas density at 0.137 mol L^{-1} . See text for details.

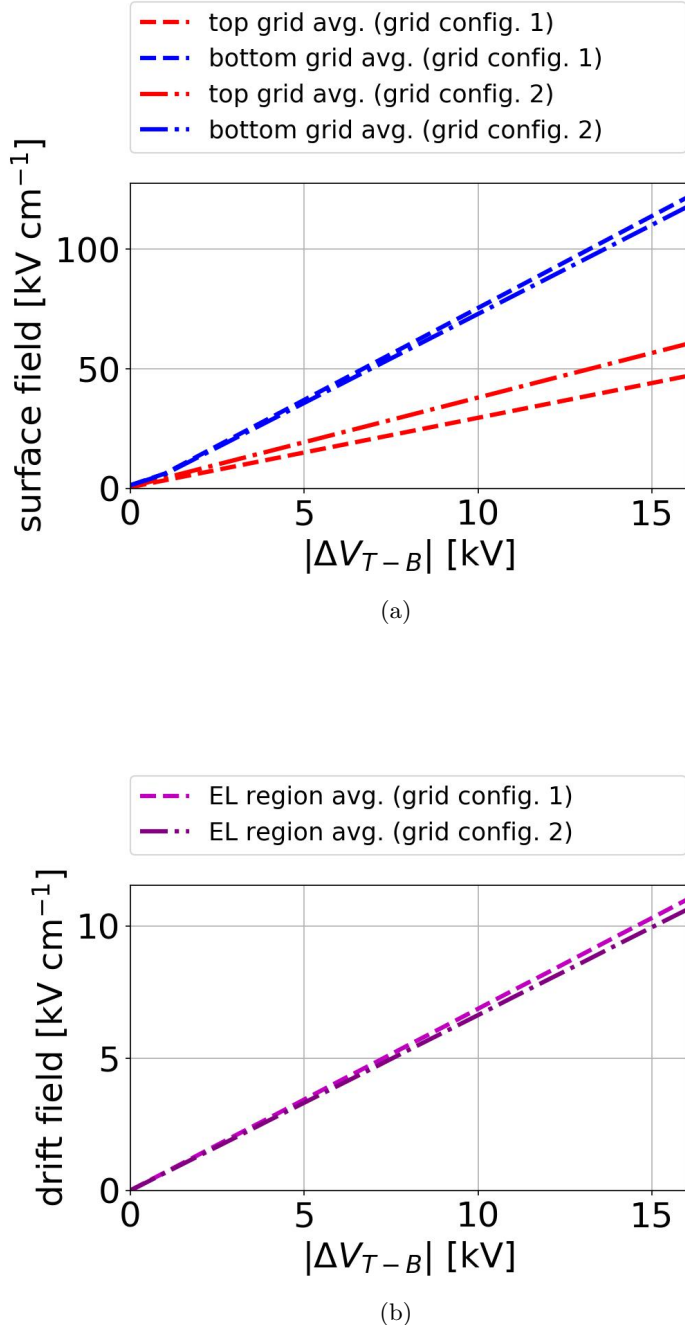


Figure 1.13: *Gas Test* detector electric field. (a) *Gas Test* wire surface electric field vs. ΔV_{T-B} for the top and bottom grid in different grid configurations. (b) *Gas Test* EL region drift electric field vs. ΔV_{T-B} in different grid configurations.

With the known surface reduced electric field, electron multiplication (cathodic gas gain) is studied using gas simulation softwares. A simple geometry is build and meshed in GMSH, as described in Ref. [13]. This software is capable of defining 3D finite element mesh, which interfaces with softwares like ElmerSolver and Garfield++ to solve the electric field in a defined geometry. Fig. 1.14a shows the defined geometry. This geometry includes a thin cylinder surface in the center representing the grid wire as the electron emission surface, and a thick cylinder surface outside representing the cut off distance of electron multiplication. The cut off distance is chosen to be sufficiently long so that the electric field beyond this distance is too small to allow significant electron multiplication. The diameter of the two cylinders are $75\ \mu\text{m}$ and 1 cm. Voltages are assigned to two cylinders to create a chosen electric field on the surface of the wire. Then, the electric field map in this full geometry is solved by Elmer, as described in Ref. [14, 15]. The gas simulation under such electric field map is done with Magboltz in Garfield++ interface, as described in Ref. [16, 17]. These softwares implement light yield and charge yield, aka the photon and electron production, for electrons moving in gas medium as a function of reduced electron field. By including the electric field map, choosing the corrects gas density, these softwares simulate the photon and electron production with an electron that initiate from the wire surface.

An example of electron multiplication simulation in the simple geometry is shown in Fig: 1.14b. As the electron moves further away from the wire surface, both light production and electron production reduce. Results of the counts of electron multiplication vs. surface electric field at different gas density is shown in Fig. 1.15. The number of collected EL photons of the electron emission signal signals are shown in Fig. 1.16. Together with the EL duration, the number of collected EL photons are the important features of electron emission signal signals that we used in the signal classification.

Therefore, electron emission signals have a known EL duration, and EL photons production dependence on the detector operating gas density and ΔV_{T-B} . We use these two important appearance to distinguish electron emission signals in the future signal classification.

1.8.2 Particle radiation

Particle radiation is the high energy particle originating from radioactive decay of unstable atoms in materials inside and outside the detector. The high energy particle enter the detector and deposit energy there through different processes. A high energy photon (gamma radiation) loses energy through thermal elastic scattering, photoelectric process, Compton scattering, and other particle energy loss processes; A high energy charged particle, e.g. electron (beta radiation), ${}^4_2\text{He}$ (alpha radiation), predominately loses it energy through ionizing atoms in detector materials, as described in Ref. [18]. These processes produce excited xenon atoms and free electrons thus producing primary scintillation and EL photons. The primary scintillation photons (S1) are collected and seen immediately. The free electrons, on the other hand, drift according to the electric field in the detector,

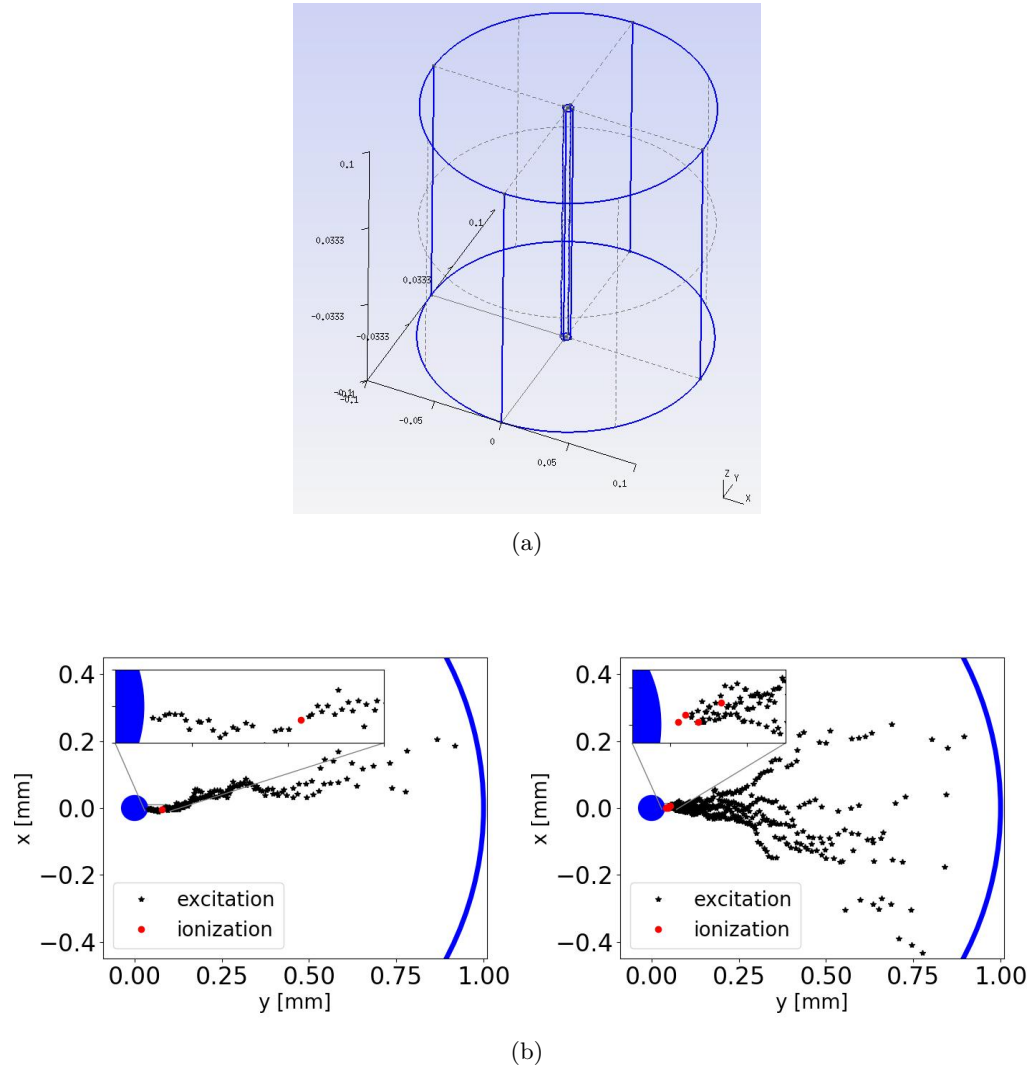


Figure 1.14: A 3D simulation of an electron drifting in an axial symmetric electric field in xenon gas. (a) Geometry defined in GMSH (unit in cm) [13]. Electrons are emitted at one point from the wire in the center. (b) Example simulation results, which is taken at operating gas density 0.137 mol L^{-1} ($T = 295 \text{ K}$, $P = 3.3 \text{ bara}$), showing the excitation and ionization sites. The blue curves are the boundary of the outer edge of simulation (diameter : 2 mm) and the wire surface (diameter: 75×10^{-3} mm). Left: a simulated event with a single ionization site. Right: a simulated event with four ionization sites. This simulation is conducted with Elmer and Garfield++, as described in Ref. [14–17].

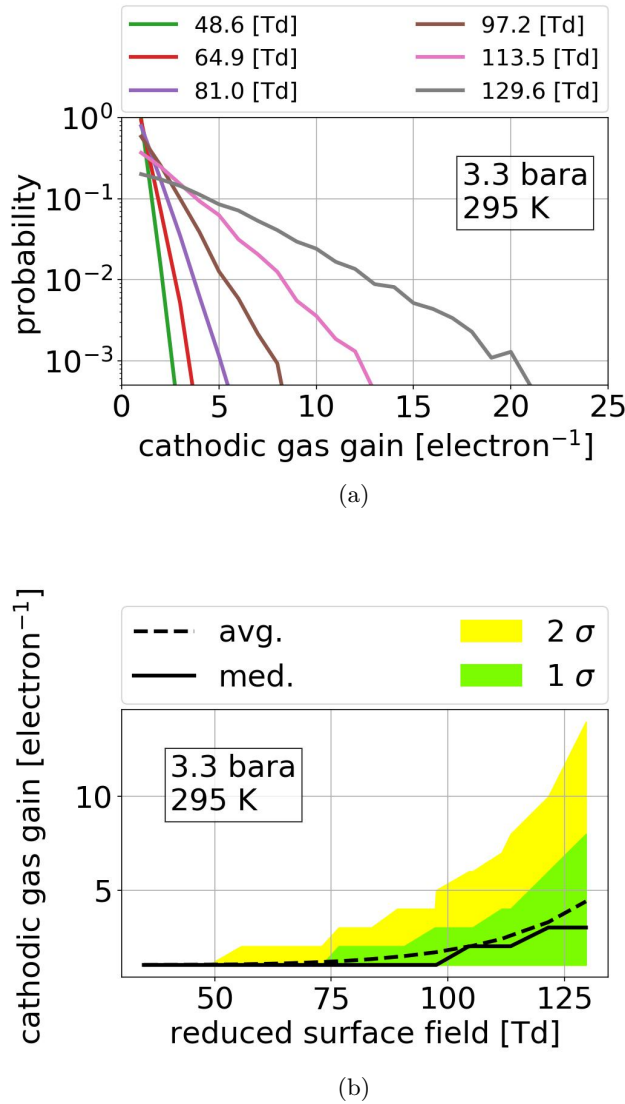


Figure 1.15: Simulated cathodic electron gas gain vs. reduced surface electric field. (a) Simulated cathodic gas gain probability distribution in different reduced surface electric fields. (b) The average, median, 1σ band (15.9 % to 84.1 %), and 2σ band (2.3 % to 97.7 %) of cathodic gas gain vs. the reduced surface electric field. Simulation is taken at operating gas density 0.137 mol L^{-1} ($T = 295 \text{ K}$, $P = 3.3 \text{ bara}$).

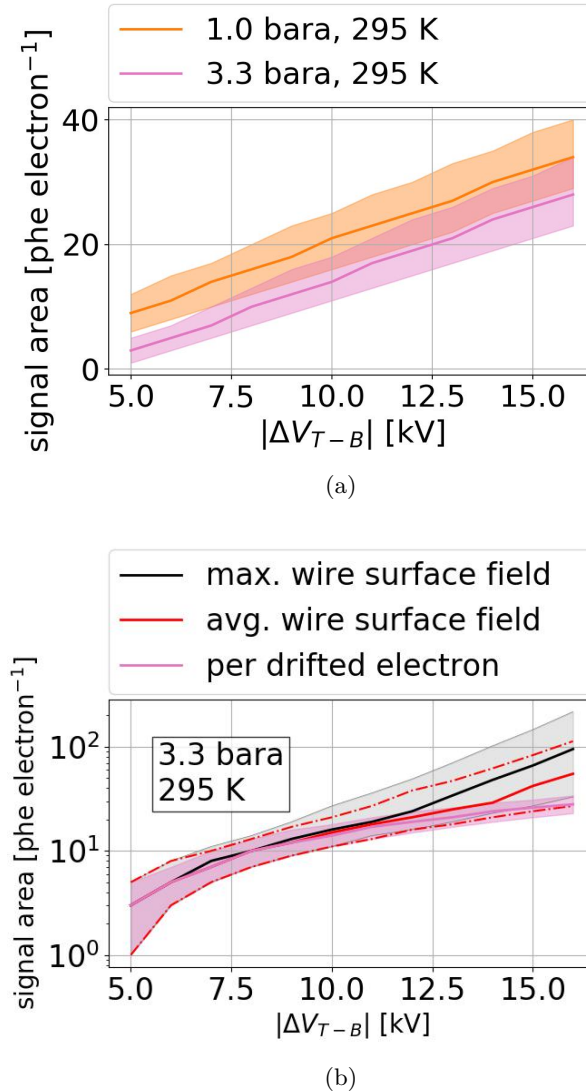


Figure 1.16: Simulated signal areas vs. ΔV_{T-B} . (a) Simulated signal area of a single drifted electron from the bottom grid at different gas densities. (b) Simulated signal area of an electron generated at different locations on the bottom grid. The black line corresponds to locations with maximum electric field on the grid. The red line corresponds to locations with average electric field on the grid. The green line shows the simulated signal area of a single drifted electron. Simulation is taken at operating gas density 0.137 mol L^{-1} ($T = 295 \text{ K}$, $P = 3.3 \text{ bara}$). The solid lines are the medians. The dashed lines, color shaded bands are 1σ bands (15.9 % to 84.1 %), respectively.

850 produce different signals.

851 A high energy gamma event can enter the ELD since its energy loss in detector skin materials is
 852 small. The photon attenuation length, which characterizes how far a photon can go, usually decrease
 853 as we have denser materials, higher average atomic mass in the materials, and lower incident particle
 854 energy. The photon attenuation length in xenon is shown in Fig. 1.17. Along photon attenuation,
 855 high energy electrons can be produced from gamma radiation through some kind of energy loss
 856 process, like Compton scattering, Auger electron emission. These high energy electrons can be
 857 produced inside the ELD, deposit its energy, and raise signals in the detector. The energy deposition
 858 length depends on the material, especially its density and its average atomic mass, and the energy
 859 of the incident particle. Similar to the photon attenuation process, denser material, higher average
 860 atomic mass, and lower incident particle energy usually results in smaller energy deposition length.
 861 The energy deposition length in xenon is shown in Fig. 1.18. For an electron with energy in the range
 862 of 10 keV to 1000 keV, which is the common energy for beta radiation, the continuous slowing down
 863 approximation range (CSDA range), also known as the average path length traveled by the charged
 864 particle (electron), is in the range of $6 \times 10^{-4} \text{ g cm}^{-2}$ to 1 g cm^{-2} , corresponding to $1 \times 10^{-5} \text{ cm}$ to
 865 $2.0 \times 10^{-2} \text{ cm}$ with xenon gas density at 0.137 mol L^{-1} ($18.0 \times 10^{-3} \text{ g cm}^{-3}$). The number of free
 866 ionization electrons in this event is associated with the energy-loss of the incident particle. During
 867 the measurement, a population associated with xenon K shell X-ray (K_α : 29.8 keV, K_β : 33.6 keV,
 868 from Ref. [Dulieu2007, TabRadv8]) is observed to be one of the byproduct of particle radiation
 869 energy loss process, confirming that this type of signal is associated with external radiation.

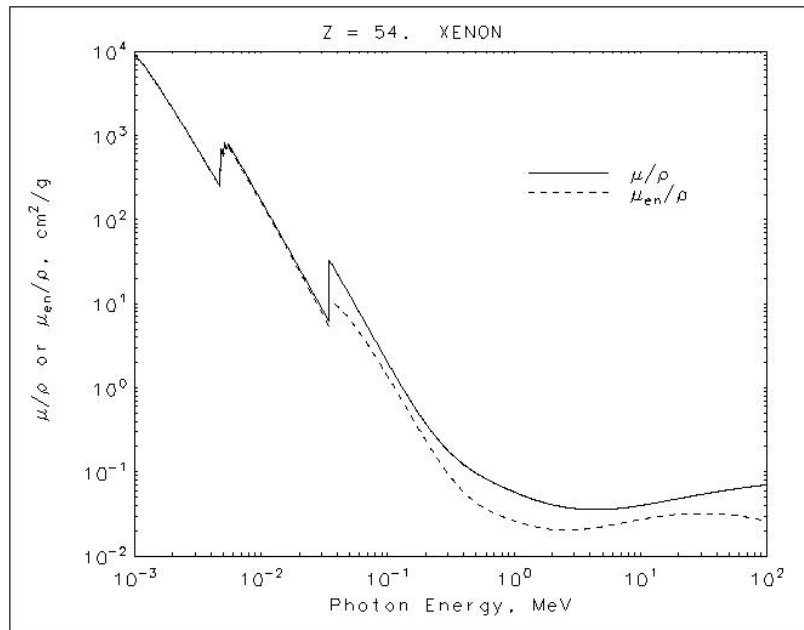


Figure 1.17: Attenuation length of photon in xenon, from Ref. ??.

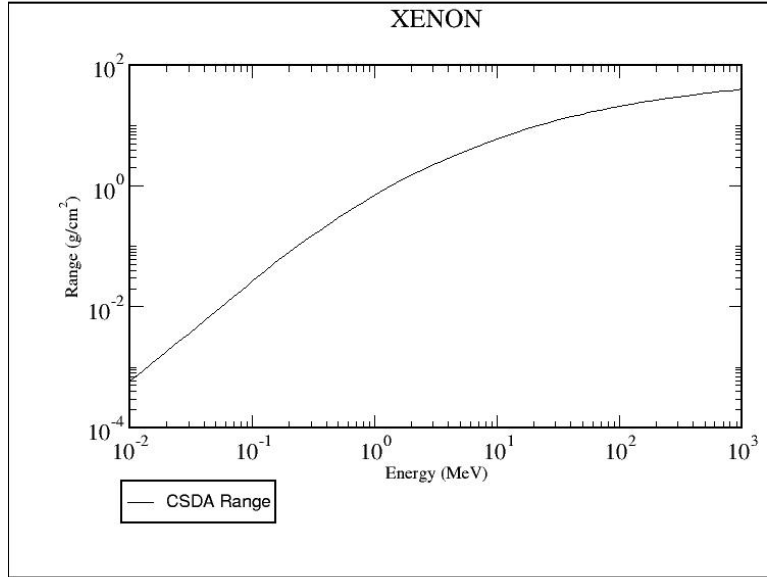


Figure 1.18: CSDA range of electrons in xenon, from Ref. ??.

A high energy external beta radiation, however, is less likely to enter the ELD compared to high energy gamma radiation because the beta radiation penetration length (approximate to the material CDSA range) is shorter than gamma radiation. Since the electron CDSA range is small compared to the thickness of xenon gas skin outside the ELD, with addition stopping power from dense PTFE reflector cone, the beta radiation would be stopped before it enters the ELD.

According to the location of energy deposition site, the high energy particle from radiation produce different look of signals, which will be discussed separately.

Anode cone event Anode cone events are the particle radiation events which have energy deposition location in the PTFE reflector cone close to the anodic grid side (anode cone). A cartoon of the physical process and an example waveform of anode cone event, as well as two zoomed plots of the waveform in different parts of the process, are shown in Fig. 1.19. The cartoon part A in Fig. ?? shows an external particle entering the anode cone region and deposit energy there. This process produce scintillation photons, the signal of which are collected and seen immediately, shown in Fig. 1.19c. The primary scintillation signal normally has a TBA (top-bottom asymmetry) heavier in the anode side PMT than the cathode side, indicating this photon signal is produced in the anode cone (top cone in this case). The free electrons drift to the anodic grid according to the electric field in the anode cone . Even though the electric field in the cone region is too small to produce large quantity of EL light during electron drift, when these electrons get close to the anodic grid wire, the electric field around the anodic grid wires are big enough to produce EL light. This is the

889 source of the secondary photon signal, which follows the preceding signal after the amount of time
 890 that it took electron to drift. The cartoon part B in Fig. 1.19a shows this process, and Fig. 1.19d
 891 shows the corresponding part of the signal. The pulse shape of the secondary photon signals has a
 892 comparably slower rising and falling edge at the beginning and the ending of it. It also has a higher
 893 TBA because EL around the anode wire primarily happens above the anodic wire. The bottom
 894 PMT is in the shadow of grid wires when the top PMT is not. This difference causes a ratio of ~ 2
 895 increment on light collection ratio between the top PMT and the bottom PMT. These characteristic
 896 signatures are useful for veto large-area anode cone events. However, when their signal area get
 897 smaller (probably because of a lower energy deposition of external particles), it becomes difficult to
 898 find these signals by their shape. Therefore, a signal selection based on preceding signal is conducted
 899 to find the secondary signal from the primary scintillation signal. The time separation between these
 900 two signal is estimated by the known measured electron drift velocity in gaseous xenon, as described
 901 in Ref. ???. Electron drift velocity in gaseous xenon is approximately $0.556 \text{ mm } \mu\text{s}^{-1} \text{ Td}^{-1} \text{ E/N}$ for
 902 reduced electric field (E/N) in the range of 5 Td to 25 Td. The maximum separation time for this
 903 detector at xenon gas density 0.137 mol L^{-1} , top grid voltage V_T in the range of +4 kV to +8 kV is
 904 approximately $85 \mu\text{s}$ to $75 \mu\text{s}$. The value of this maximum separation time decreases as decreasing
 905 the operation pressure in the detector. The value of maximum separation time drives the choice of
 906 $100 \mu\text{s}$ preceding signal selections of this type of signals.

907 **Cathodic cone event** Cathode cone events are the particle radiation events which have energy
 908 deposition location in the PTFE reflector cone close to the cathodic grid side (cathode cone). A
 909 cartoon of the physical process and an example waveform of cathode cone event are shown in
 910 Fig. 1.20. Similar to anode cone events, this process produce scintillation photons. However, the
 911 ionization electrons produced drift to cathode PMT. Therefore, EL light typically is produced during
 912 along their trajectories because the electric field in such region is much lower than the EL threshold.
 913 The primary scintillation signal normally has a TBA heavier in the cathode side PMT than the
 914 anode side PMT, indicating this photon signal is produced in the cathode cone (bottom cone in this
 915 case), as expected.

916 **S1 S2 event in the cathode corner** S1 S2 events in the cathode corner (cathode corner events)
 917 are the particle radiation events which have energy deposition location either outside EL region and
 918 very close to the cathodic grid or in the corner between the cathodic grid and the cathodic cone.
 919 A cartoon of the physical process and an example waveform of cathode corner event are shown in
 920 Fig. 1.21. Similar to anode cone events, this process produce scintillation photons, which is shown
 921 in Fig. 1.21a (left) and the waveform of which is shown in the first $0.3 \mu\text{s}$ in Fig. 1.21b. Since the
 922 free electrons produced in this event is really close to the cathode grid, according to electrostatic
 923 study using COMSOL software described in Ref. [19], these electrons drift to cathodic grid, pass
 924 it, then drift in the EL region, the process of which produces EL photons along the trajectories of

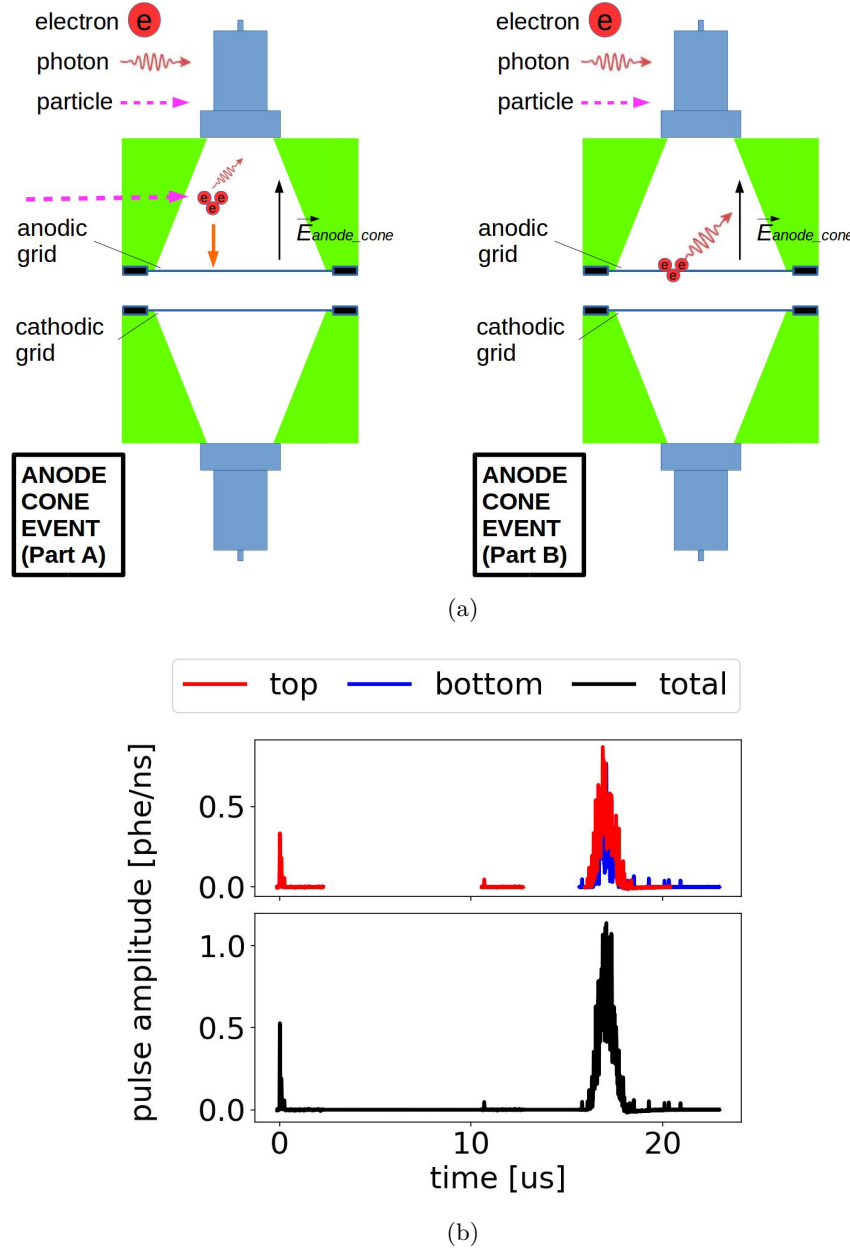


Figure 1.19: *Gas Test* signal: anode cone event. (a) Cartoon of the process. Left: Primary scintillation light ionization electrons are produced from the particle interaction, and the ionization electrons drift to the anodic grid (part A). Right: EL light is produced in the high electric field region around the anodic grid wires (part B). (b) An example waveform of an anode cone event. Data were taken at 2017-12-8 14:02, with grid voltages V_T and V_B at +6 kV and -6 kV, operating gas density at 0.137 mol L^{-1} .

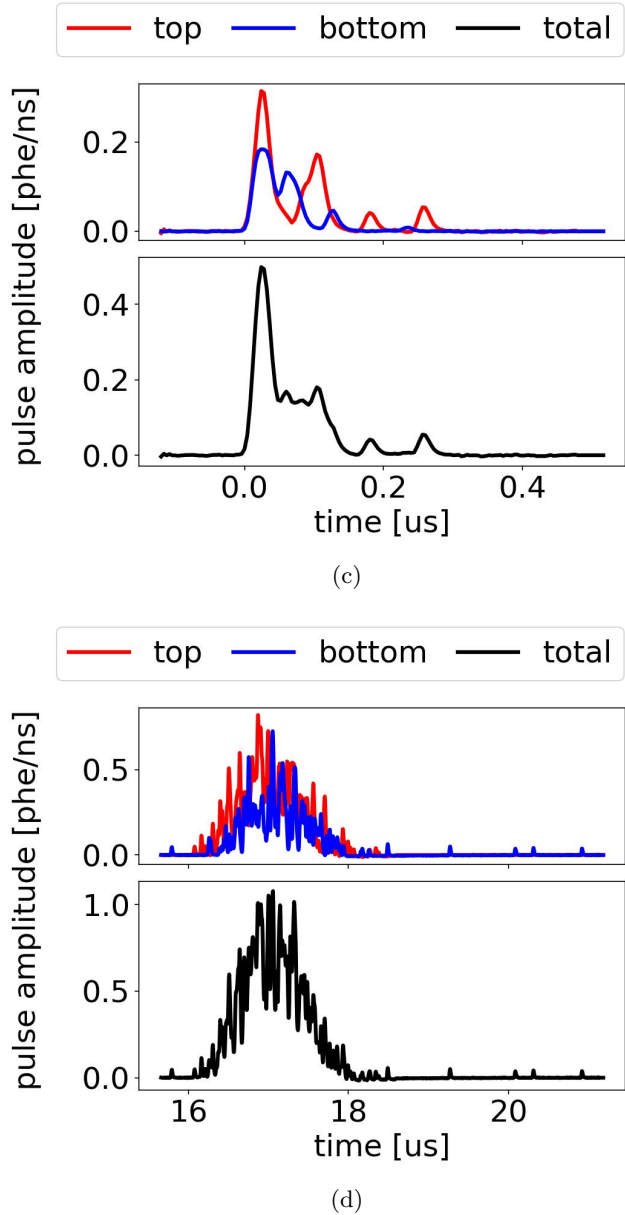


Figure 1.19: *Gas Test* signal: anode cone event (cont.). (c) An example waveform of an anode cone event, zoomed in the range of $0 \mu\text{s}$ to $0.5 \mu\text{s}$, which shows the primary scintillation light (cartoon part A). (d) An example waveform of an anode cone event, zoomed in the range of $15 \mu\text{s}$ to $21 \mu\text{s}$, which shows the EL light produced around the anodic grid wires (cartoon part B).

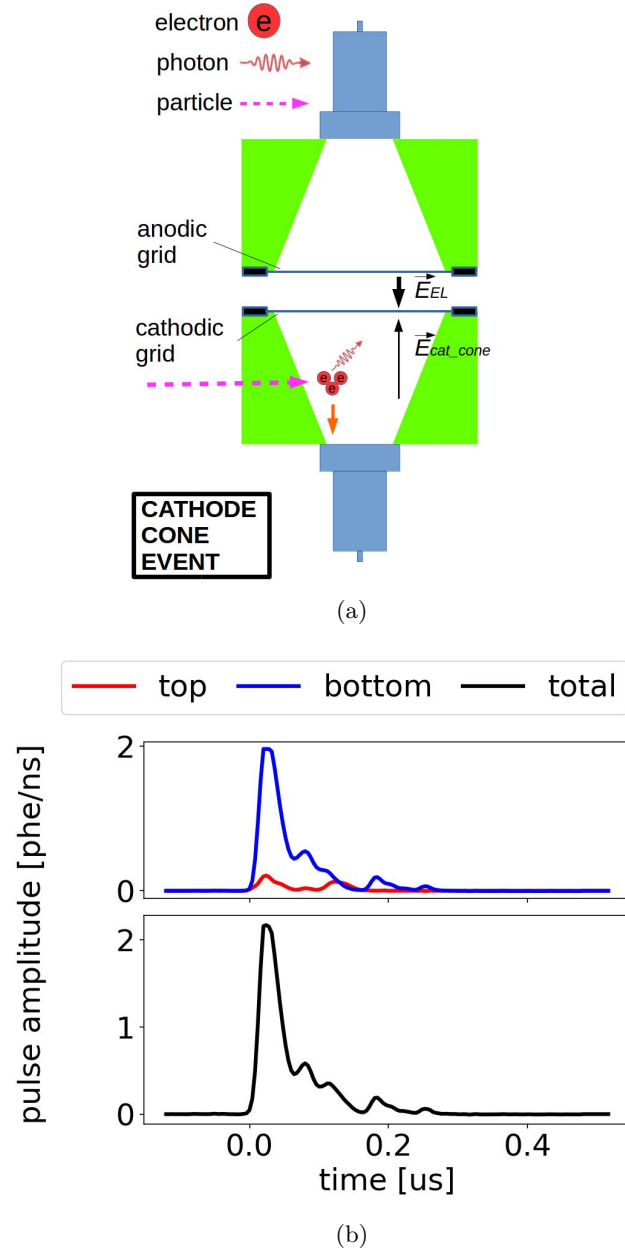


Figure 1.20: *Gas Test* signal: cathode cone event. (a) Cartoon of the process. Primary scintillation light ionization electrons are produced from the particle interaction, and the ionization electrons drift toward the bottom PMT. EL light is typically not produced along the trajectories of the electrons because the electric field in such region is lower than the EL threshold. (b) An example waveform of a cathode cone event. Data were taken at 2017-12-8 14:02, with grid voltages V_T and V_B at +6 kV and -6 kV, operating gas density at 0.137 mol L^{-1} .

the electrons, and finally land on the anodic grid. This EL light production process is illustrated in Fig. 1.21a (right), which corresponds to the waveform after $0.5\ \mu\text{s}$ in Fig. 1.21b. The static electric field from COMSOL solution is shown in Fig. 1.22. Both the primary scintillation signal and the secondary EL signal has a balanced TBA, indicating these photon signals are produced either in or really close to the EL region.

S1 S2 event in the EL region S1 S2 events in the EL region (EL region events) are the particle radiation events which have energy deposition location either in EL region. The process and an example waveforms is shown in Fig. 1.23. Since the electrons are produced in the energy deposition location in the EL region, these electrons drift in the EL region toward the anodic grid, producing EL photons. The duration of these signals are shorter compared to the electron emission signals because of the shorter drift length. The total quantity of photon production in this type of events is usually higher than that of an electron emission event, an anode cone event, and a cathode cone event, because of the free drifted electrons inside the EL region.

High photon count events High photon count events are those particle radiation events that are extremely high on energy, therefore producing plenty primary scintillation photon, free drifted electrons, and EL photons during the events. The photon production rate is so high that it exceeds the digitizing ability of the DAQ system (also called saturate the DAQ), causing distortion on waveform recording thus resulting in difficulty of signal classification. These signals may have various origins. Some of these signals have comparable or shorter duration than electron emission signals, two example waveforms are shown in Fig. 1.24 and Fig. 1.25. These events might be related to the EL region events, described in Section 1.8.2, or grid wire radiation and ring radiation, which are the particle radiation events originated from radioactive elements in grid wire and ring materials.

The radioactive elements in the ring material can be both from the impurities in the material, e.g. ^{238}U , ^{232}Th , and ^{235}U and from the absorption of air on the material surfaces, e.g. ^{222}Rn . Among these sources, air radon absorption draw the most concern because of its abundance. The decay activity of radon induced radiation plating per unit of surface area per unit of time ($RA_{\text{Rn-rad}}$) is estimated as,

$$RA_{\text{Rn-rad}} = RV_{\text{Rn}} h_{\text{eff}} T_{\text{exposure}} \frac{1}{\tau_{\text{eff}}} \quad (1.20)$$

where RV_{Rn} is the radon decay activity in the air per unit of volume per unit of time; h_{eff} is the effective height of radiation plating, in which the radon decay daughter nuclei will plate on material surface; T_{exposure} is the exposure time of plating; and τ_{eff} is the effect decay time constant of radon decay daughter nuclei. With regard to $RV_{\text{Rn}} 48\ \text{Bq m}^{-3}$, from Ref. [20], $h_{\text{eff}} \sim 1\ \text{m}$, $\tau_{\text{eff}} \sim 32\ \text{yr}$, from the decay time constant of ^{210}Pb , the typical daughter nucleus from the radon decay, in Ref. [Dulieu2008], and $T_{\text{exposure}} 1\ \text{d}$, $RA_{\text{Rn-rad}}$ is $\sim 4 \times 10^{-3}\ \text{Bq m}^{-2}$. For a $\sim 40\ \text{cm}^2$ grid wire

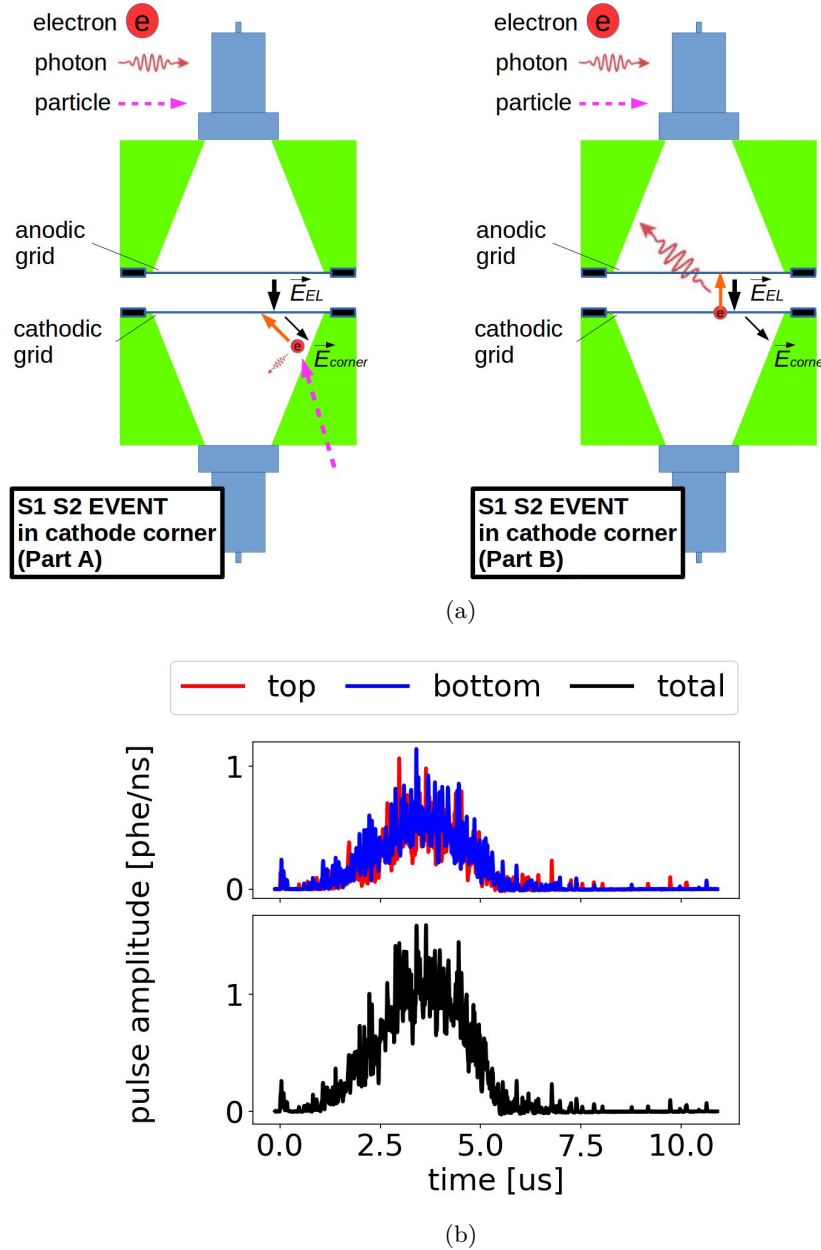


Figure 1.21: *Gas Test* signal: S1 S2 event in the cathode corner. (a) Cartoon of the process. Left: Primary scintillation light and ionization electrons are produced from the particle interaction, and the ionization electrons drift to the cathodic grid (part A). Right: EL light is produced in the EL region during electrons drifting to the anodic grid (part B). (b) An example waveform of an S1 S2 event in the cathode corner. Data were taken at 2017-12-8 14:02, with grid voltages V_T and V_B at +6 kV and -6 kV, operating gas density at 0.137 mol L^{-1} .

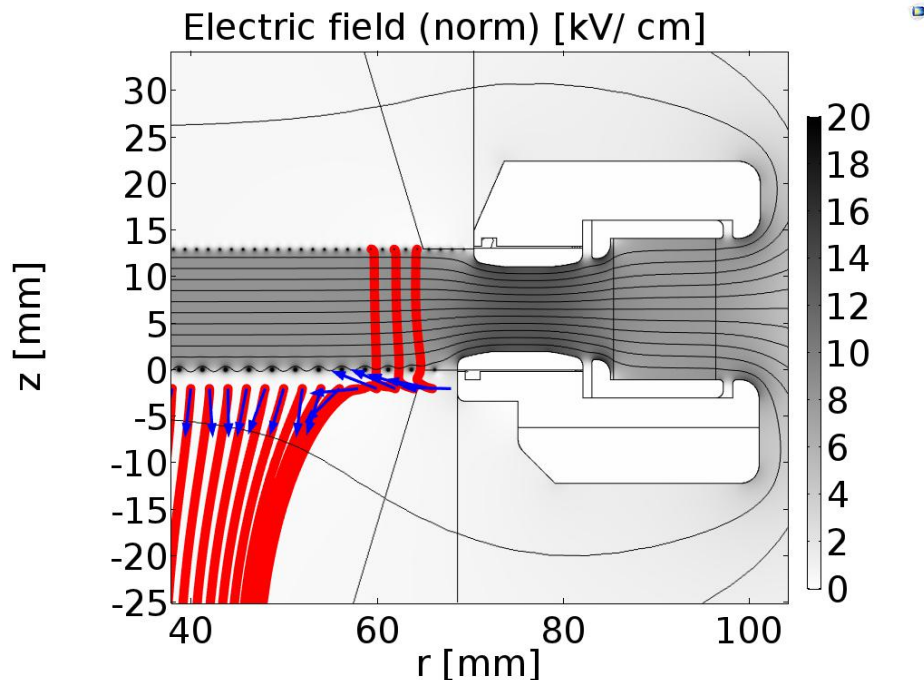


Figure 1.22: Electrostatic solution of the *Gas Test* detector (grid ring region). This result is solved with grid voltages V_T and V_B at +6 kV and -6 kV using COMSOL. The white metal structures in the middle of the figure are the cross sections of the grid rings. The contours show the electric potential; the color scales show the norm of electric field; the blue arrows shows the directions of the initial electron drift; the red lines shows the trajectory of electrons that start drifting at 2 mm below the bottom grid: electrons starting at $r < 60$ mm drift downward, when electrons starting at $r > 60$ mm drift into the EL region (cathode corner event).

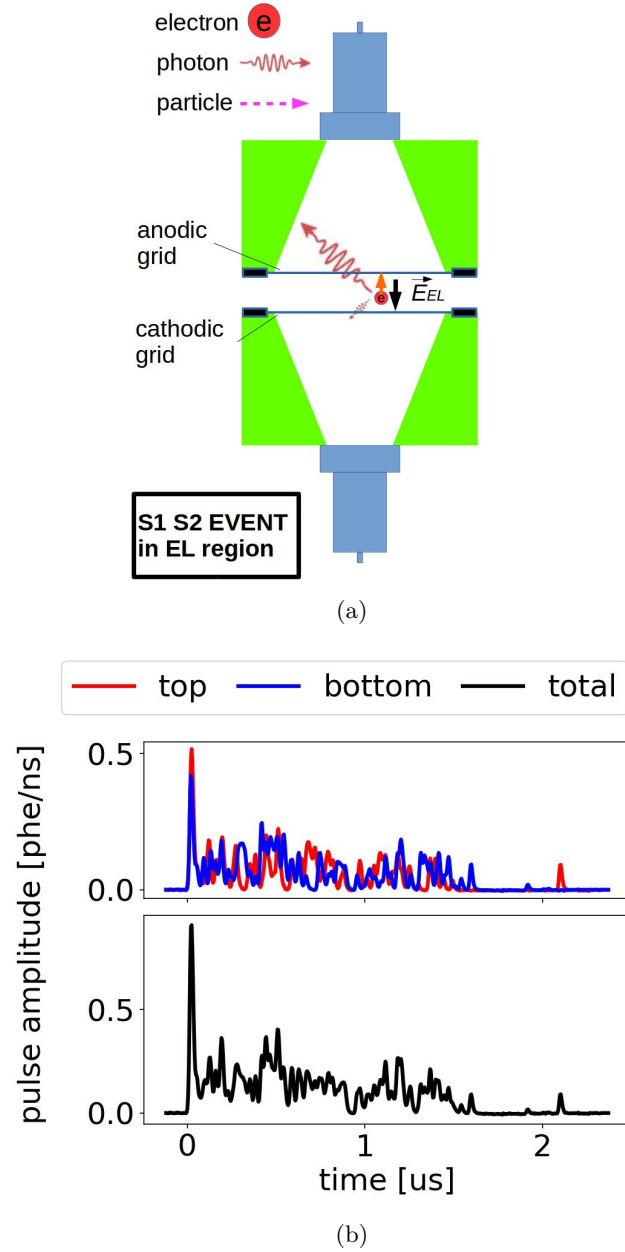


Figure 1.23: *Gas Test* signal: S1 S2 event in the EL region. (a) Cartoon of the process. Primary scintillation light and ionization electrons are produced from the particle interaction. The primary scintillation light and the EL light start to be produced simultaneously. (b) An example waveform of an S1 S2 event in the EL region. The primary scintillation light lies on top of the EL light. Data were taken at 2017-12-8 14:02, with grid voltages V_T and V_B at +6 kV and -6 kV, operating gas density at 0.137 mol L^{-1} .

and grid ring total surface area, The total decay activity of radon induced radiation from the ring surface is $\sim 10^{-5}$ Bq. These event rates should be relatively rare compared to other processes.

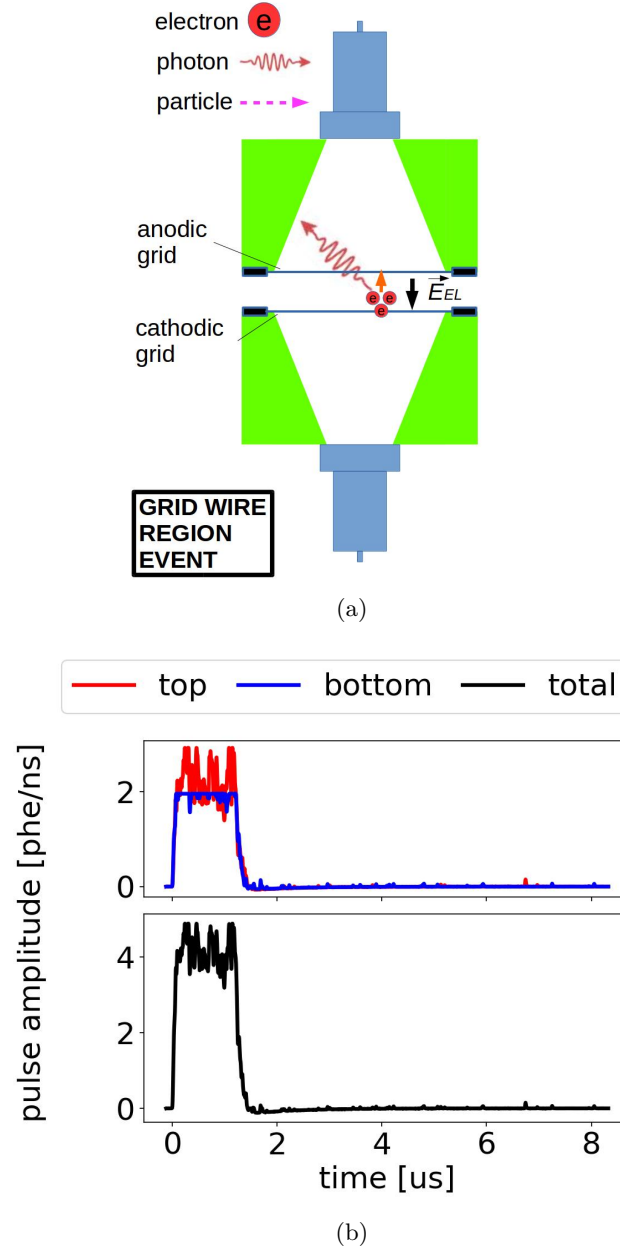


Figure 1.24: *Gas Test* signal: grid wire region event. (a) Cartoon of the process. (b) An example waveform. This might be an S1 S2 event in the EL region between the grid wires, when the primary scintillation light is clipped off because the signal amplitude exceeds DAQ dynamic range (PMT saturation). Data were taken at 2017-12-8 14:02, with grid voltages V_T and V_B at +6 kV and -6 kV, operating gas density at 0.137 mol L^{-1} .

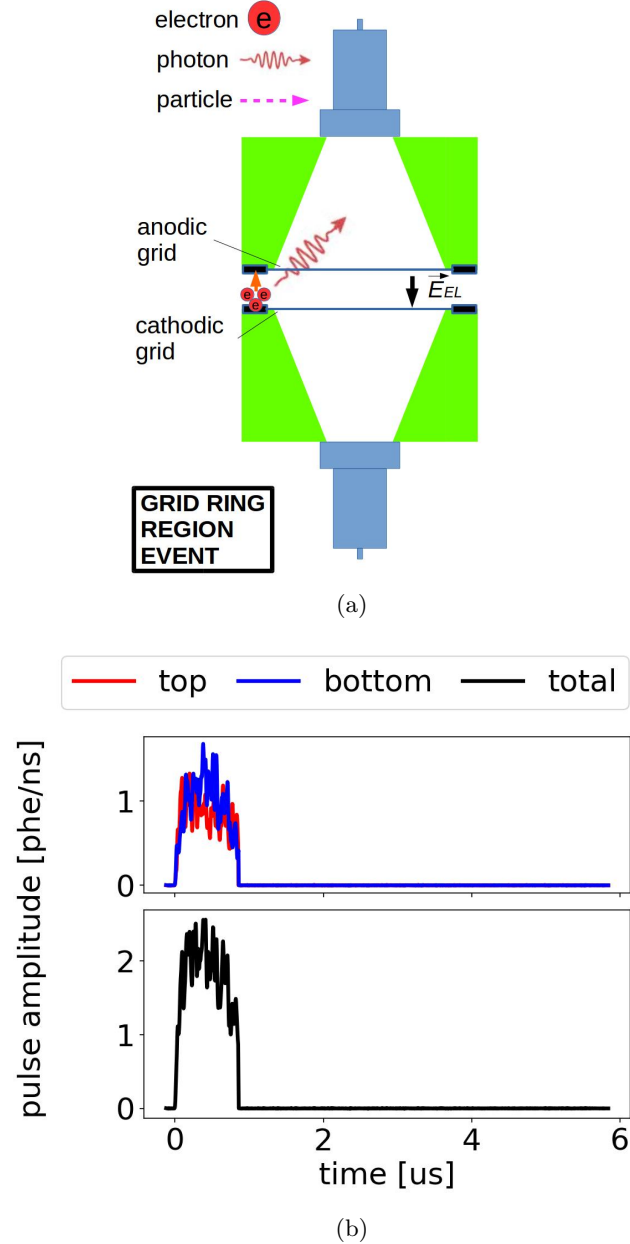


Figure 1.25: *Gas Test* signal: grid ring region event. (a) Cartoon of the process. (b) An example waveform. This might be an S1 S2 event in the EL region between the grid rings, when the primary scintillation light is not visible because the light collection efficiency is poor in this region. Data were taken at 2017-12-8 14:02, with grid voltages V_T and V_B at +6 kV and -6 kV, operating gas density at 0.137 mol L^{-1} .

959 Multiple scattering events Multiple scattering events are those with more than one energy
 960 deposition location. The common source of these events are a high energy gamma radiation, since
 961 it can travel far distance in the detector. The multiple scattering events usually are combinations
 962 of the previous mentioned type of events. Two example waveform are shown in Fig. 1.26: the first
 963 one is a multiple scattering event in the anode cone region; the second one is a multiple scattering
 964 event in the anode cone region and the EL region.

965 1.8.3 Cosmic ray

966 Cosmic rays, originating outside Earth, are capable of producing showers of secondary particles that
 967 reach the *Gas Test* detector and giving rise to signals in the detector. Among all secondary particles
 968 that raise signals, muons are the most common one because of their abundance and high penetration
 969 length in earth atmosphere. Unlike alpha, beta, and gamma particle radiation, a cosmic ray muon
 970 has a longer ionization trajectory which travels crossing the whole detector.

971 The long ionization trajectory leads to a large quantity of primary scintillation light and free
 972 electron production, which results in a large light production. The minimum stop power of muon is
 973 $1.255 \text{ MeV g}^{-1} \text{ cm}^2$ in xenon, from Ref. [21]. In xenon gas, the reported average energy to produce
 974 a primary scintillation photon (W_{sci}) and electron-ion pair (W_{ion}) are $\sim 100 \text{ eV}$ ² and 22 eV ³,
 975 respectively. Therefore, with detector operating gas density at 0.137 mol L^{-1} , a muon event produce
 976 $\sim 2 \times 10^2$ primary scintillation photons and $\sim 10^3$ per centimeter length of muon trajectory. The
 977 large quantity of primary scintillation light and EL light production associated with free electrons
 978 results in large signal area detected for a muon event.

979 Therefore, a cosmic ray muon signal has a different appearance compared to other signals because
 980 of its long ionization trajectory and large quantity of primary scintillation light and electron-ion pair
 981 production. The appearance of muon signals also varies according to their different trajectories in
 982 the detector, which will be discussed below.

983 EL region muon event EL region muon events are those events that crosses the EL region, as
 984 well as the anode cone region and the cathode cone region. A cartoon and an example waveform
 985 are shown in Fig. 1.27. Like particle radiation events, at the very beginning of the signal, primary
 986 scintillation photons are produce in the first 500 ns. Simultaneously, during the first $2.5 \mu\text{s}$, the
 987 shown signal is dominated by EL photons, which decrease in time because the electrons in the EL
 988 region land on the anodic grid thus stopping EL photon production, illustrated in Fig. 1.27a (left).
 989 Since free electrons are generated all the way including the EL region, there is prompt EL light that
 990 masks the primary scintillation, causing difficulty to distinguish light from these two processes. At a
 991 higher absolute value of $\Delta V_{\text{T-B}}$, there is higher photon production per drifted electron, which results

² W_{sci} is $111(16) \text{ eV}$ in Ref. [22], and $72(6) \text{ eV}$ in Ref. [23].

³ W_{ion} is 22 eV in Ref. [24–26].

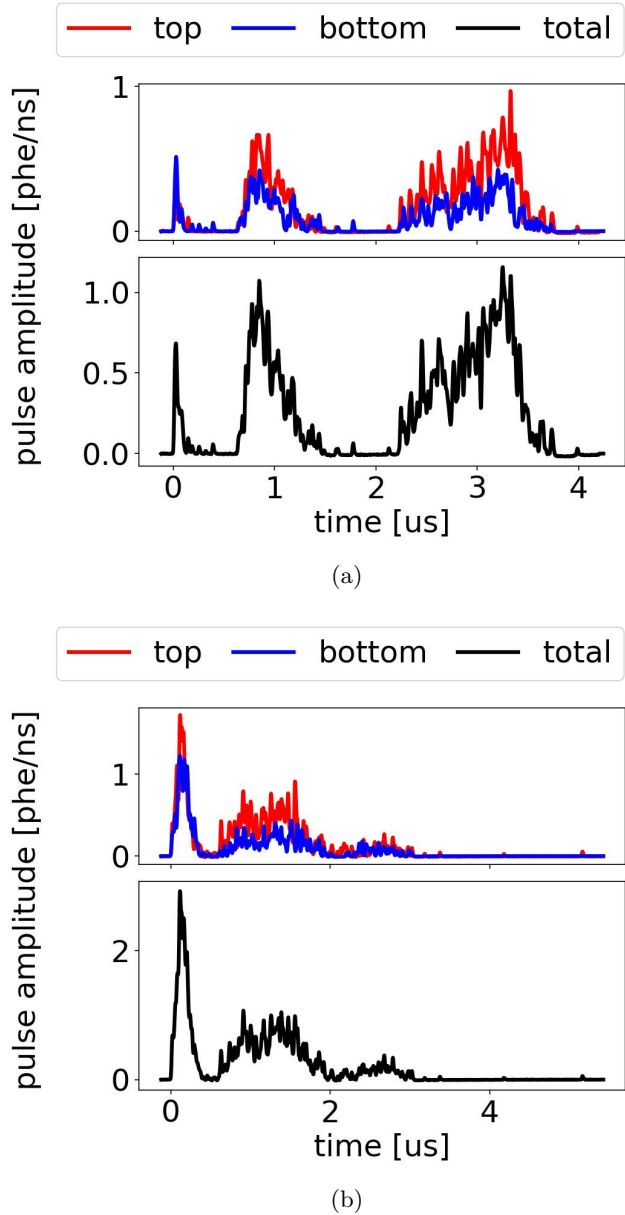


Figure 1.26: *Gas Test* signal: multiple scattering event. (a) An example waveform of a multiple scattering event in the anode cone region. (b) An example waveform of a multiple scattering event in the anode cone region and the EL region. Data were taken at 2017-12-8 14:02, with grid voltages V_T and V_B at +6 kV and -6 kV, operating gas density at 0.137 mol L^{-1} .

in an increase in the signal amplitude and signal area. This high signal amplitude can exceed the dynamic digitization range of the DAQ and results in a clip on the waveform, like in Fig. 1.27b. After all electrons in the EL region reach the anodic grid, the signal is dominated by electrons originally produced in the anode cone drift to the anodic grid and EL photons are produced in the high electric field around the anodic grid, illustrated in Fig. 1.27a (right), which is “long tail” part of the signal in the range of $2.5\ \mu\text{s}$ to $10\ \mu\text{s}$ in Fig. 1.27b.

EL region muon events between grid rings are those events that crosses the EL region between the grid rings, without crossing the anode cone region. The cartoon of this process is shown in Fig. 1.28a. Similar to other EL region muon events, these events produces primary scintillation light and EL light between the grid rings. However, since the muon trajectory does not cross the anode cone region, there are no free electrons produced in such region, which leads to the absence of the “long tail” in the signal, as shown in Fig. 1.28b.

Anode cone muon event Anode cone muon events are those events that crosses only the anode cone region. A cartoon and an example waveform are shown in Fig. 1.29. At the very beginning of the signal, primary scintillation photons are produce in the first 500 ns, the process and waveform of which are shown in Fig. ?? and Fig. 1.29c. Next, electrons originally produced in the anode cone drift to the anodic grid and EL photons are produced in the high electric field around the anodic grid, the process and waveform of which are shown in Fig. 1.29a and Fig. 1.29d.

Cathode cone muon event Cathode cone muon events are those events that crosses only the cathode cone region. A cartoon and an example waveform are shown in Fig. 1.30. At the very beginning of the signal, primary scintillation photons are produce in the first 500 ns, the process and waveform of which are shown in Fig. 1.30a and Fig. 1.30b. Next, electrons originally produced in the cathode cone drift to the cathode PMT associated with few EL photons production in this low electric field cathode cone region.

1.8.4 Other miscellaneous sources

Electrical noise Electrical noise are the disturbance in an electrical system during signal transfer. Electrical noise can come from both internal and external sources to the system, and can add to the systematic fluctuation of other signals from the *Gas Testdetector*. This systematic fluctuation is characterized by the baseline fluctuation, whose amplitude is $\sim 0.36\ \text{mV}$, which is very small compared to signal amplitude of the wanted signals.

Electrical noise from the external electrical grounding of the infrastructures and the KNF pump, however, has an amplitude up to $5\ \text{mV}$ and is capable of start a separate pulse recording sometimes; this type of electrical noise is called electrical noise signals. An example waveform of electrical noise signal is shown in Fig. 1.31. As shown in this figure, an electrical noise signal is likely to have the

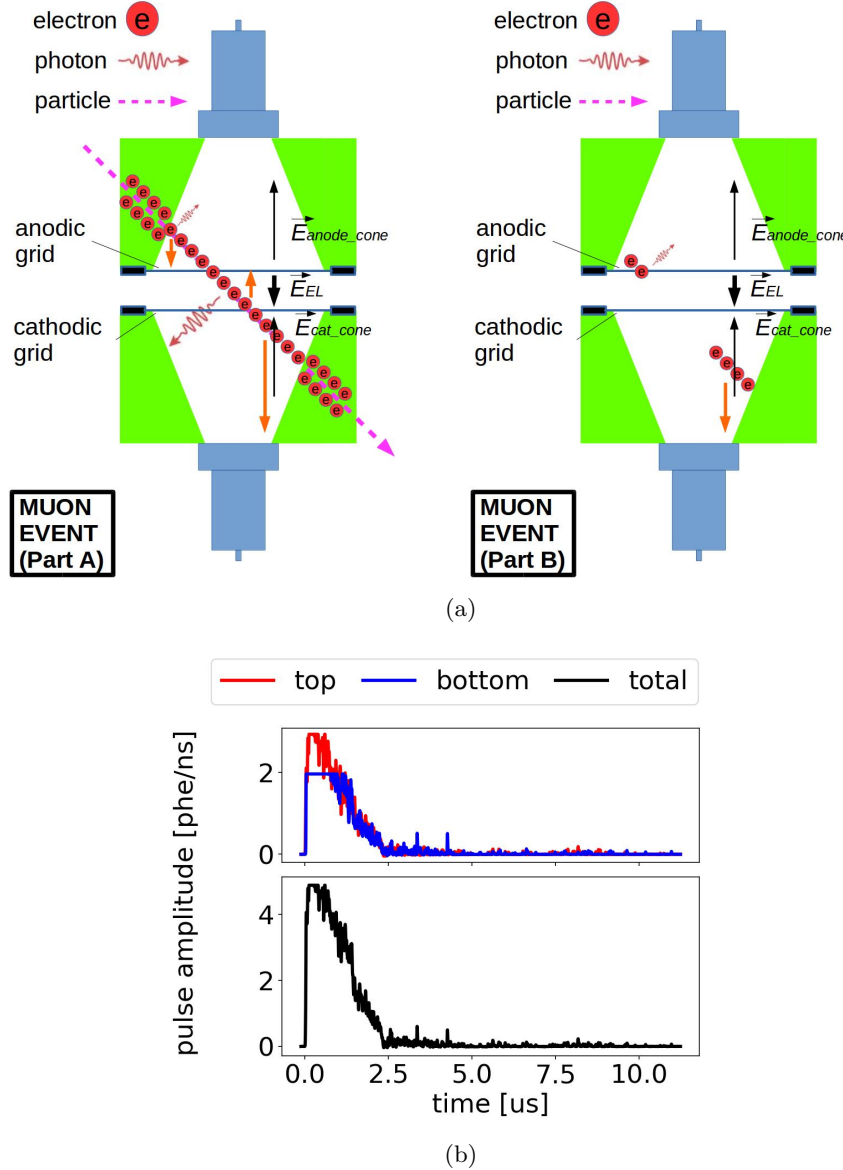


Figure 1.27: *Gas Test* signal: EL region muon event. (a) Cartoon of the process. Left: Primary scintillation light and ionization electrons are produced along the muon trajectory, and ionization electrons drift according to the direction of the electric field. EL light also start to be produced by the ionization electrons in the EL region (part A). Right: EL light is produced in the high electric field region around the anodic grid wires (part B). (b) An example waveform of an EL region muon event. The right-angled triangle shape waveform before $2.5 \mu\text{s}$ is the EL light produced in the EL region (cartoon part A). The primary scintillation light is clipped off because of the PMT saturation. The “long tail” after $2.5 \mu\text{s}$ is the EL light produced around the anodic grid wires (cartoon part B). Data were taken at 2017-12-8 14:02, with grid voltages V_T and V_B at $+6 \text{ kV}$ and -6 kV , operating gas density at 0.137 mol L^{-1} .

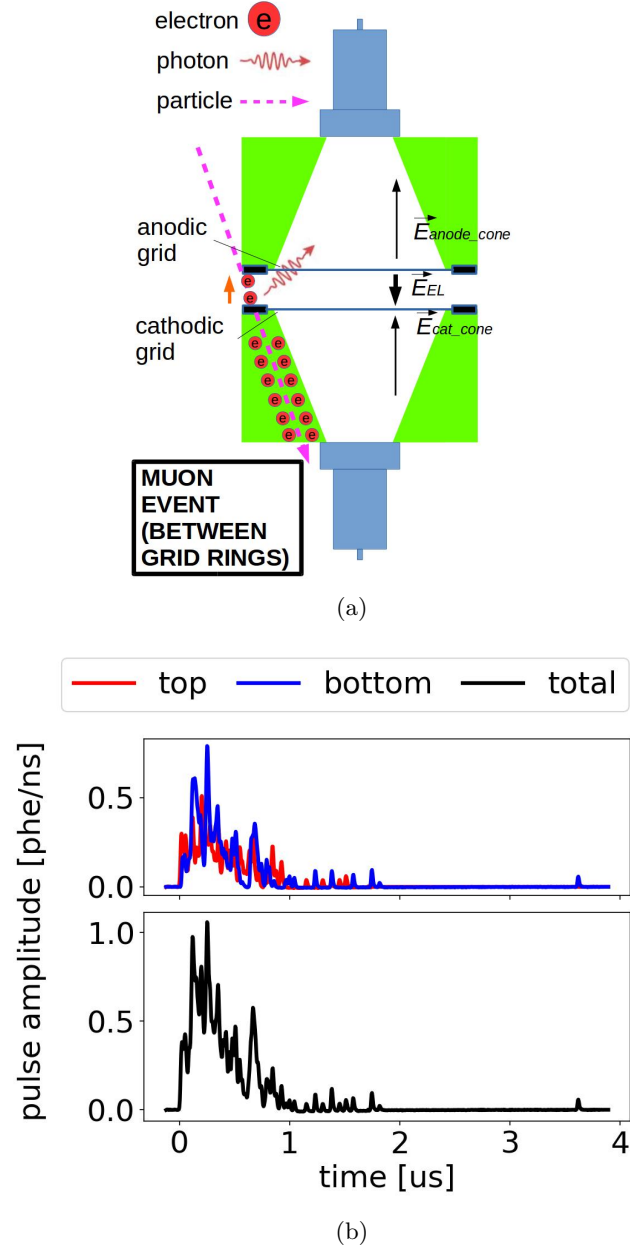


Figure 1.28: *Gas Test* signal: muon event between the grid rings. (a) Cartoon of the process. This process is similar to that of the EL region muon event except there are no electrons produced in the anode cone region. (b) An example waveform. The absence of “long tail” is because of the absence of electrons produced in the anode cone region. Data were taken at 2017-12-8 14:02, with grid voltages V_T and V_B at +6 kV and -6 kV, operating gas density at 0.137 mol L^{-1} .

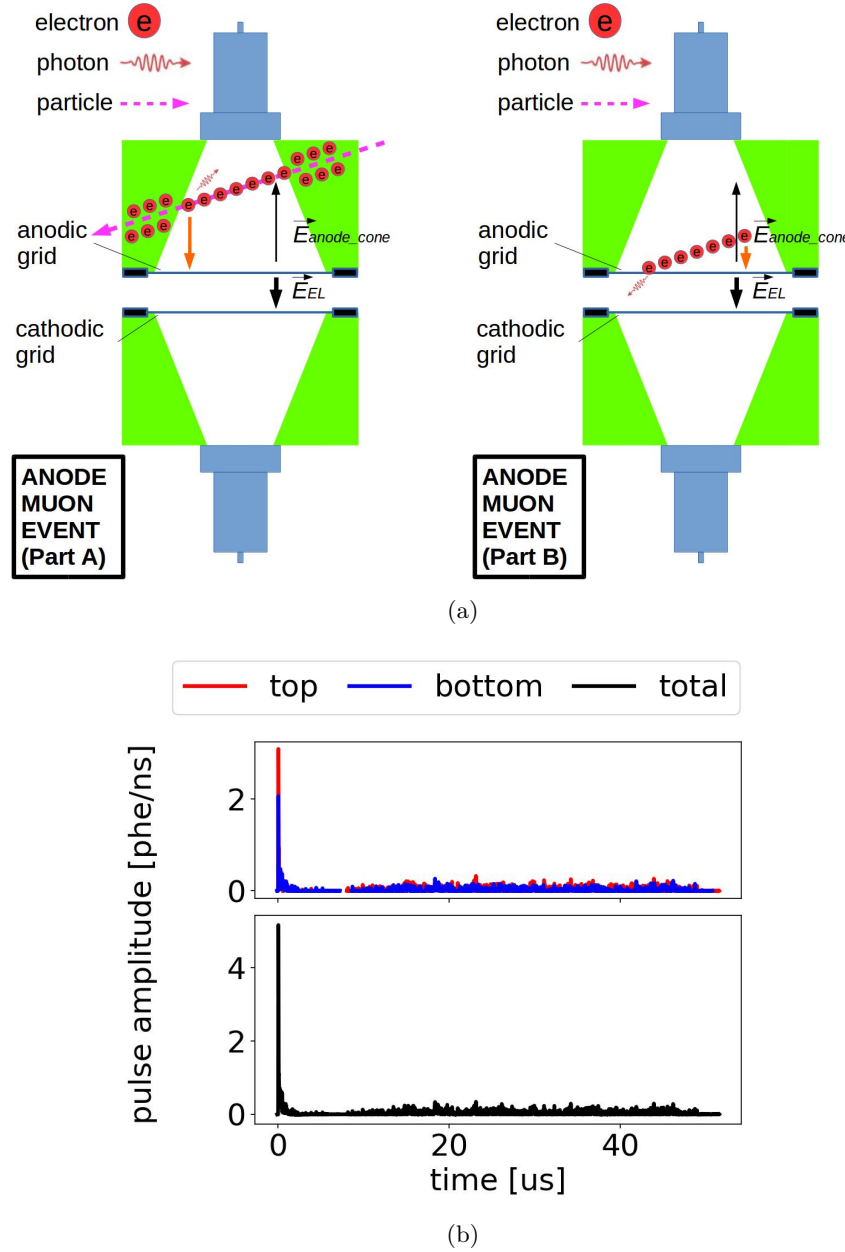


Figure 1.29: *Gas Test* signal: anode cone muon event. (a) Cartoon of the process. This process is similar to that of the EL region muon event except for there are no electrons produced in the EL region. (b) An example waveform of an anode muon cone event. The absence of the “right-angled triangle shape waveform” is because of the absence of electrons produced in the EL region. Data were taken at 2017-12-8 14:02, with grid voltages V_T and V_B at +6 kV and -6 kV, operating gas density at 0.137 mol L^{-1} .

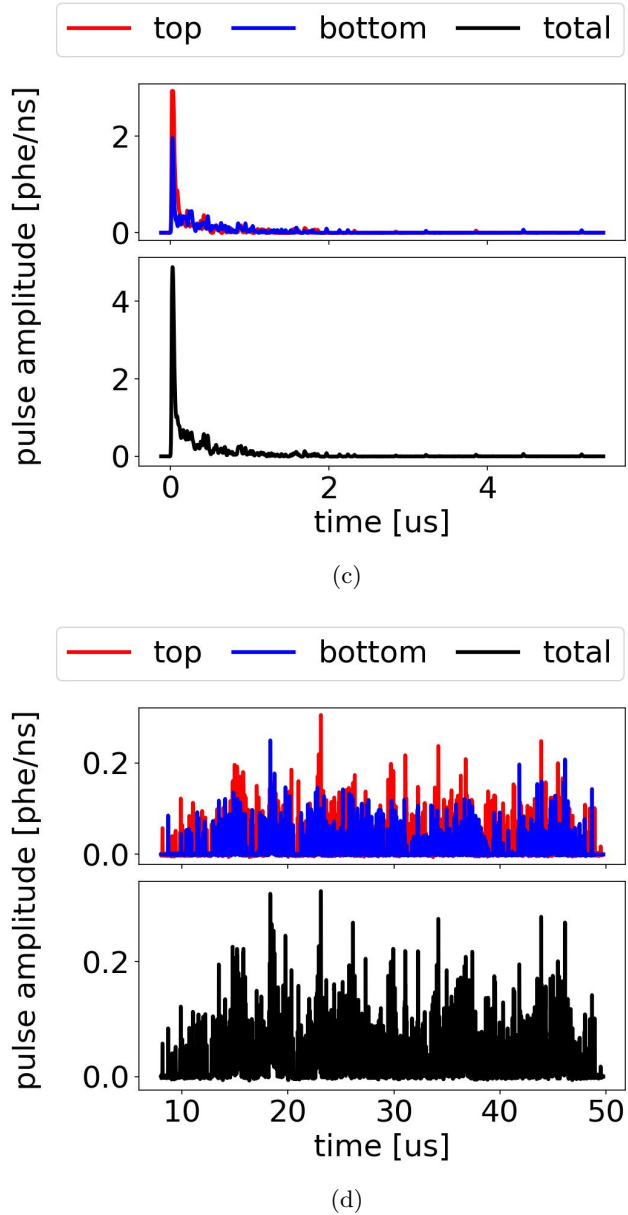


Figure 1.29: *Gas Test* signal: anode muon cone event (cont.). (c) An example waveform of an anode muon cone event, zoomed in the range of $0 \mu\text{s}$ to $5 \mu\text{s}$, which shows the primary scintillation light (cartoon part A). (d) An example waveform of an anode cone muon event, zoomed in the range of $6 \mu\text{s}$ to $50 \mu\text{s}$, which shows the EL light produced around the anodic grid wires (cartoon part B).

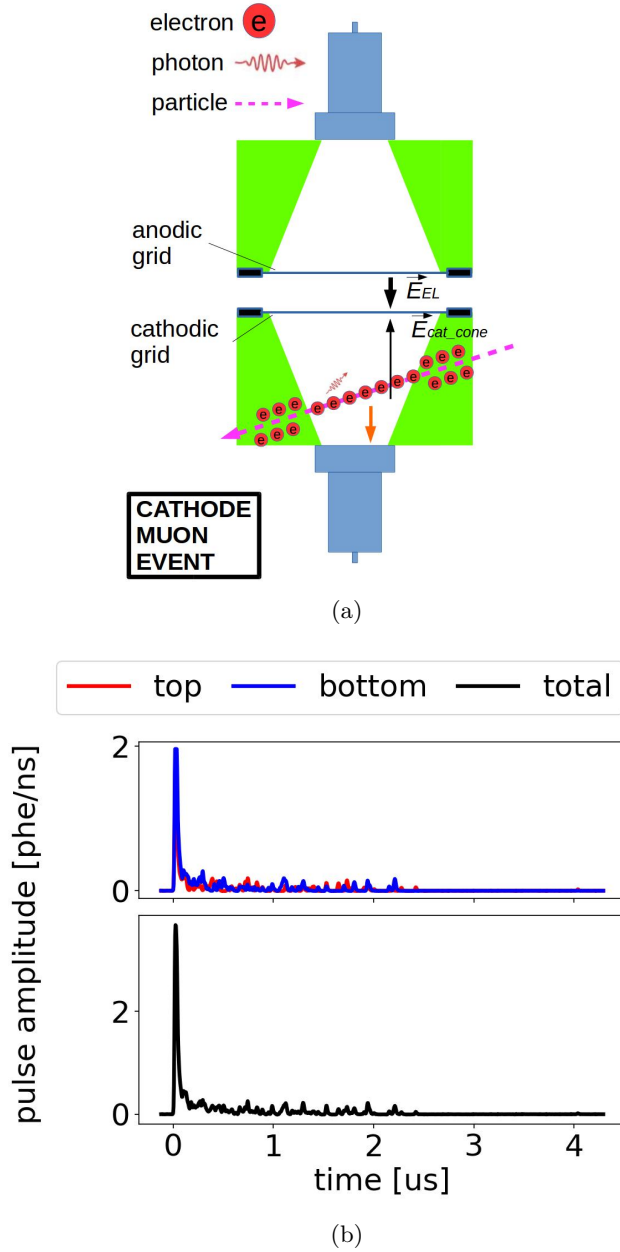


Figure 1.30: *Gas Test* signal: cathode cone muon event. (a) Cartoon of the process. This process is similar to that of the EL region muon event except for there are no electrons produced in the EL region or the anode cone region. (b) An example waveform of a cathode muon cone event. The absence of the “right-angled triangle shape waveform” and the “long tail” is because of the absence of electrons produced in the EL region and the anode cone region. Data were taken at 2017-12-8 14:02, with grid voltages V_T and V_B at +6 kV and -6 kV, operating gas density at 0.137 mol L^{-1} .

1026 waveforms in both PMTs overlapping. The waveform in each PMT is bipolar and symmetric; that
 1027 is, the positive and negative maxima of the waveform amplitude are about the same. The bipolar
 1028 and symmetric aspect of the waveform leads to a near-zero integral of the signal area, which don't
 1029 give a meaningful waveform shape RQs because these RQ algorithms are designed for a unipolar
 1030 signal. Therefore, to reduce the influence of these electrical noise signals, the KNF pump is turn off
 1031 during all measurements and we improved on the electrical grounding of infrastructure. After this
 1032 improvement, electrical noise signals occur at a rate of ~ 2 Hz, which are further addressed by signal
 1033 selections based on the bipolar feature of the noise signals.

1034 **PMT dark current** PMT dark current usually refers to the signal from the thermal electron
 1035 emission from the photocathode and dynode surfaces, which are charges generated in the PMT
 1036 when no photon ejects photoelectrons from the photocathode surface. The thermal electrons from
 1037 the photocathode surface, like photoelectrons, if landing on the effective area of the first dynode, will
 1038 be amplified by the PMT and produce a SPHE-like signal. Such SPHE-like signals of the PMT dark
 1039 current are a major concern, since they are not distinguishable from SPHEs in signals of interest.
 1040 The thermal electrons from other surfaces may also be amplified by the PMT dynode chain and
 1041 produce signals that are distinguishably smaller than SPHE, thus drawing less concern.

1042 A random coincidence of SPHE-like signals (dark current is one of the most common sources of
 1043 SPHE-like signals) between two PMTs, is called an accidental coincidence signal. The PMTs that
 1044 are used in this study have a ~ 1 kHz dark current rate. This rate leads to a ~ 3.4 Hz rate of the
 1045 accidental coincidence signals with regard to CWW of $1.7\ \mu s$.

1046 **should I talk about PMT afterpulsing?**

1047 **PTFE fluorescence** PTFE fluorescence is the phenomenon in which PTFE emits photons that
 1048 it absorbed. This delay emission normally appears in forms of SPHEs following a high quantity
 1049 of photon production, and increase the SPHE rate succeeding. The rate of after emission photons
 1050 (fluorescence rate) roughly follows an exponential decay model:

$$\text{fluorescence rate} = f_{\text{FR}} A \frac{1}{\tau} \exp\left(-\frac{t}{\tau}\right) \quad (1.21)$$

1051 where τ is the decay time constant; t is the time since the previous photon production; A is quantity of
 1052 photons in the previous photon production that are absorb by the PTFE; and f_{FR} is the fluorescence
 1053 ratio, which is the ratio of the number of photons emitted after by the PTFE material to the number
 1054 of photons absorbed by the PTFE material.

1055 Measurements show that fluorescence rates, decay times τ , and fluorescence ratio f_{FR} have a vari-
 1056 ous range. This might be caused by different conditions of synthesis, as described in Ref. [Gachkovskii1969].
 1057 This effect is also believed to cause the slow decay of electron signal in liquid xenon TPCs. A decay
 1058 time of 2.3 ms is reported in Ref.[27]. A decay time of 10 ms is reported in internal review in LUX.

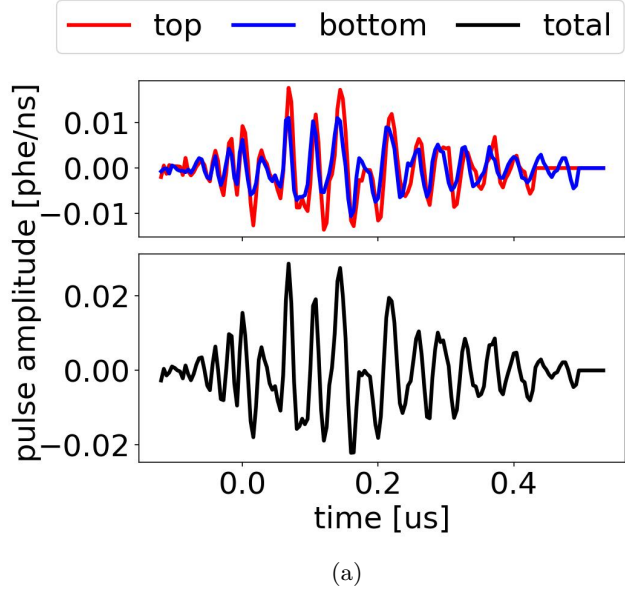


Figure 1.31: *Gas Test* signal: electronic noise signal. (a) An example waveform. Data were taken at 2017-12-8 14:02, with grid voltages V_T and V_B at +6 kV and -6 kV, operating gas density at 0.137 mol L^{-1} .

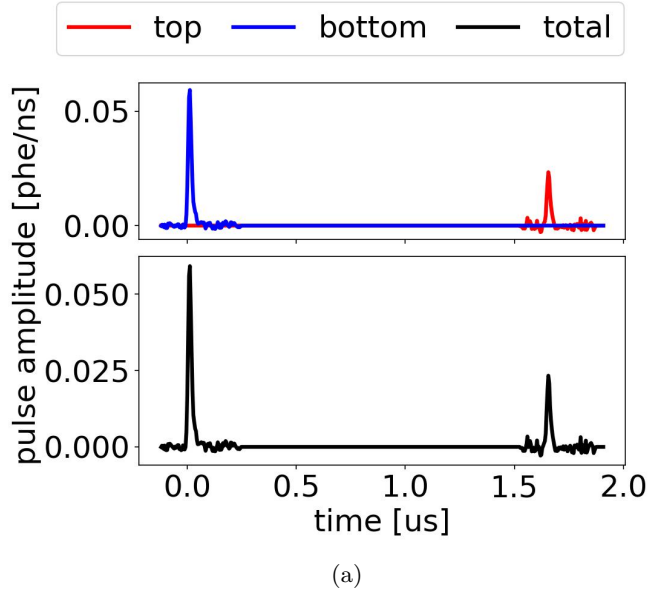


Figure 1.32: *Gas Test* signal: PMT dark current accidental coincidence. (a) An example waveform. Data were taken at 2017-12-8 14:02, with grid voltages V_T and V_B at +6 kV and -6 kV, operating gas density at 0.137 mol L^{-1} .

1059 To illustrate the large rate of SPHEs that follows a large-area signal, we look at 1-ms windows
 1060 before and after a large photon production. In the succeeding 1-ms window after $t = 0$, which is the
 1061 time when the selected large signal happened, as shown with the selected large signal in Fig. 1.33a,
 1062 Fig. 1.33b, we see 33 SPHEs. In comparison, we see only 1 SPHE in the earlier 1-ms window, as
 1063 shown in the same figure before $t = 0$. This increasing rate of SPHE increases the probability of
 1064 accidental coincidence between two PMT channels, as shown in Fig. 1.33c; given the practical choice
 1065 of our CCW, this random accidental coincidence, like PMT dark current, is a potential source of
 1066 background that looks like electron emission signals.

1067 With these examples in mind, we can quantify the fluorescence process by looking at the delayed
 1068 SPHE rate follow large-area signals over different characteristic timescales. The SPHE rate of this
 1069 PTFE fluorescence increase if the ELD has a recent large photon production. Fig. 1.34 shows the
 1070 photon rate after source signals: This photon fluorescence rate increases as the signal area of source
 1071 signals increases; and this photon fluorescence rate decreases over time.

1072 An estimation of fluorescence rate, decay time τ , and fluorescence ratio f_{FR} is carried out by
 1073 studying the photon rate in the waveform after a signal production of larger than 10^4 phe in the range
 1074 of $200 \mu\text{s}$ to $600 \mu\text{s}$ after the end time of signal. The choice of the smaller value of the succeeding
 1075 window is to avoid the influence from the anode cone events correlating signals, whereas the choice
 1076 of the later time of the succeeding window is to avoid the influence the background rate, which is
 1077 mostly contributed by dark current. In the chosen signal ranges, the background rate is $\sim 1 \text{ kHz}$ per
 1078 PMT, mostly contributed by PMT dark current. This rate is small compared to fluorescence rate
 1079 (median $\sim 20 \text{ kHz}$) per PMT, thus negligible in this estimation. Therefore,

$$\text{photon rate} \approx \text{fluorescence rate} (+ \text{background rate (dark current, etc.)}) \quad (1.22)$$

$$\propto \frac{1}{\tau} \exp\left(-\frac{t}{\tau}\right) \quad (1.23)$$

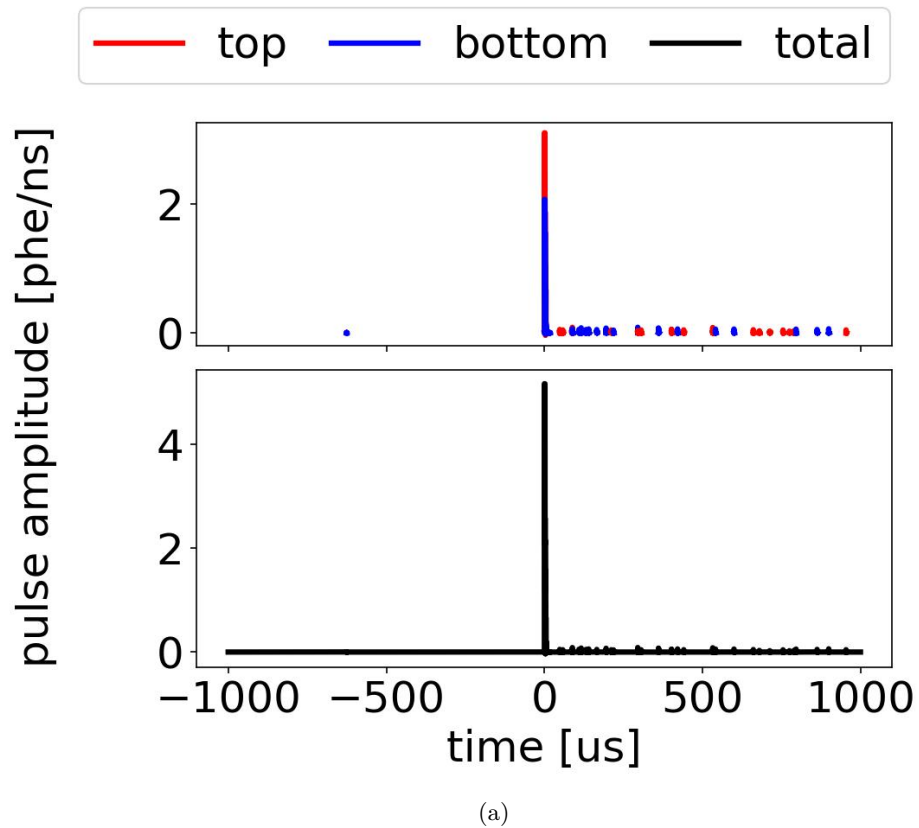
1080 To better estimate the photon rate profile and find the decay time τ , we fit this exponential decay
 1081 profile to binned data in the succeeding window. To combine multiple events to reduce the statistical
 1082 error, individual events are normalized by their signal areas in the range of $0 \mu\text{s}$ to $1000 \mu\text{s}$ and then
 1083 co-added by bin; the resulting graph is fitted, and shown in Fig. 1.35: τ of $(407 \pm 35) \mu\text{s}$.

1084 The fluorescence ratio f_{FR} is defined as,

$$f_{\text{FR}} = \frac{\# \text{ photons reemitted}}{\# \text{ photons absorbed}} \quad (1.24)$$

1085 which is the ratio of the number of photons that are reemitted from the PTFE after a large-area
 1086 event to the number of photons that are absorbed by the PTFE in a large-area event.

1087 The number of photons reemitted is estimated from the exponential decay profile defined above



(a)

Figure 1.33: *Gas Test* signal: PTFE fluorescence after an event with large photon production. (a) An example waveform 1000 μs before and after a large-area signal. There are more SPHEs after an event with large photon production than before. The SPHE rate before this large-area event is representative of the average SPHE rate. Data were taken at 2017-12-8 14:02, with grid voltages V_T and V_B at +6 kV and -6 kV, operating gas density at 0.137 mol L $^{-1}$.

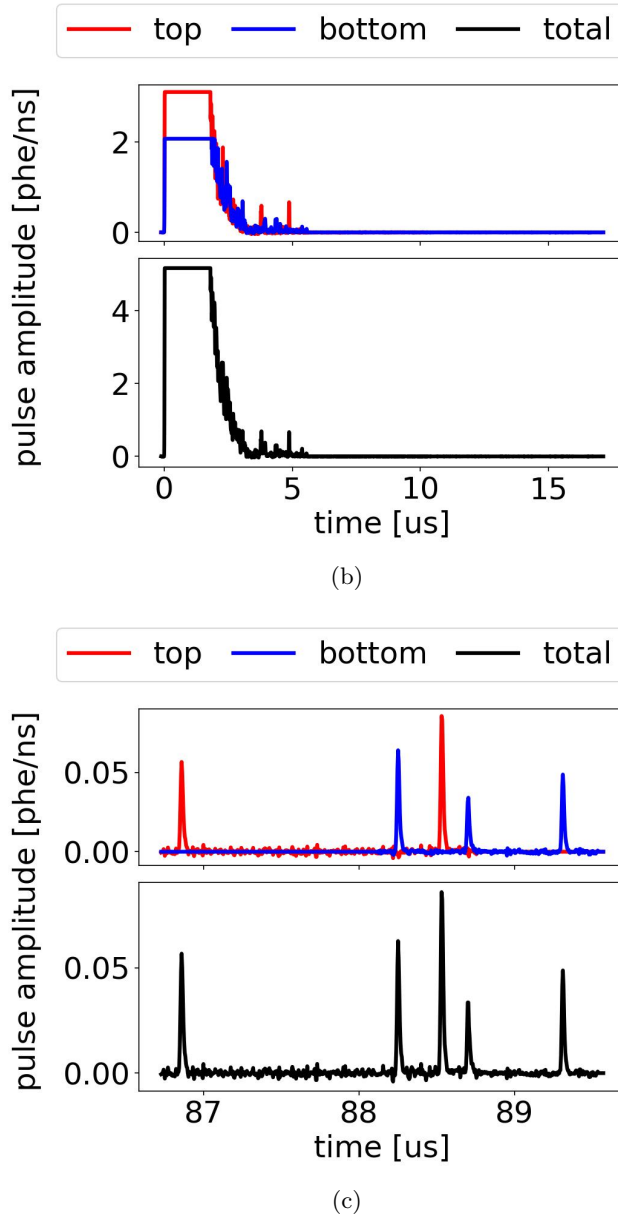


Figure 1.33: *Gas Test* signal: PTFE fluorescence after an event with large photon production (cont.). (b) An example waveform, zoomed in the range of $0\ \mu\text{s}$ to $17\ \mu\text{s}$, which shows the signal with large photon production. (c) An example waveform, zoomed in the range of $87\ \mu\text{s}$ to $89\ \mu\text{s}$, which shows PTFE fluorescence induced SPHEs accidental coincidence between the two PMTs. This accidental coincidence signal looks like an electron emission signal.

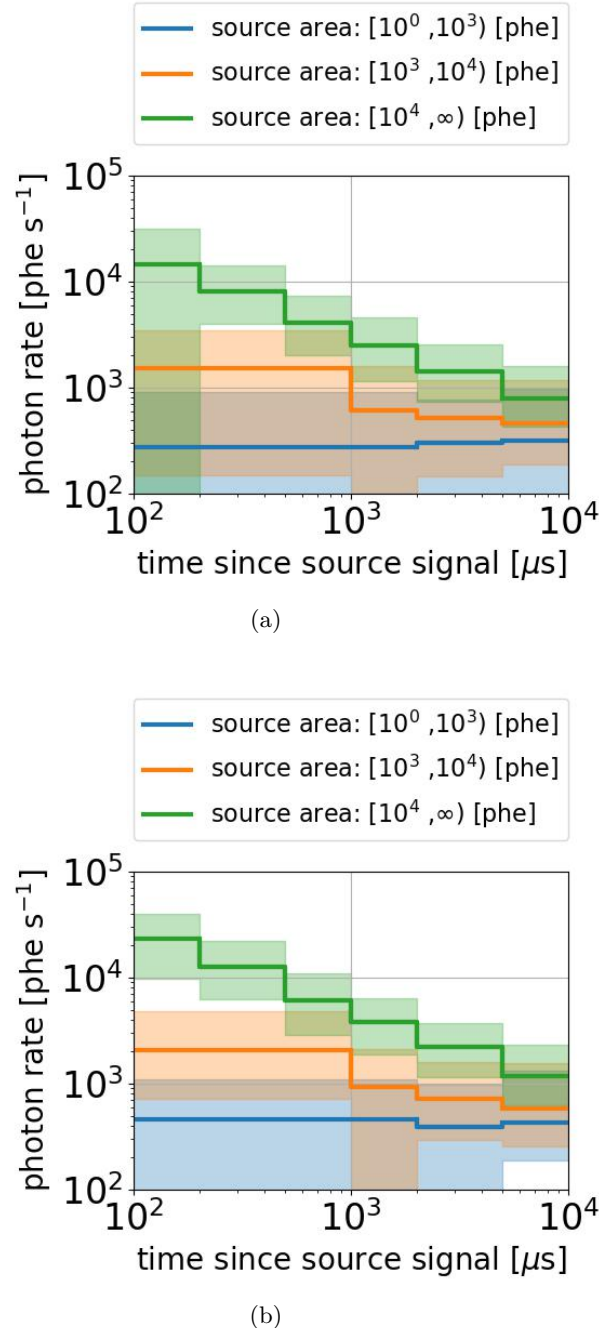


Figure 1.34: Photon fluorescence rate after photon production in the ELD: (a) top PMT; (b) bottom PMT. The solid lines show the medians. The color bands show the 25 % to 75 % bands. The choice of bin edges is made to get enough statistics in each bin.

1088 and the number of photons in the succeeding 200 ns to 600 ns window after the end of the large-
 1089 area signal. From the estimated decay time, the ratio of the number of reemitted photons in the
 1090 succeeding window (N_{SW}) to the total number of reemitted photons is derived, noted as P_{SW} :

$$P_{\text{SW}} \approx \frac{N_{\text{SW}}}{\# \text{ photons reemitted}}. \quad (1.25)$$

1091 The number of reemitted photons in the succeeding window is estimated from the number of
 1092 photons reemitted detected in the succeeding window (A_{SW}) and the light collection efficiency for
 1093 photons starting from PTFE surface:

$$A_{\text{SW}} \approx \text{LCE}_{\text{PTFE}} N_{\text{SW}}. \quad (1.26)$$

1094 where LCE_{PTFE} is the average light collection efficiency for photons starting from PTFE surface.

1095 On the other hand, the number of photons absorbed by PTFE is estimated from the total number
 1096 of photons the source large-area signal (N_{source}) and the light collection simulation of the fraction
 1097 of photons that PTFE absorbed:

$$\# \text{ photons absorbed} \approx \text{LCF}_{\text{EL-PTFE}} N_{\text{source}} \quad (1.27)$$

1098 where $\text{LCF}_{\text{EL-PTFE}}$ is the average fraction of photons absorbed by PTFE in the simulation with
 1099 photons starting in the EL region, the location where the source signals happen.

1100 The total number of photons the source large-area signal (N_{source}) is related to the detected
 1101 signal area (A_{source}) and light collection efficiency of the source signals in the EL region (LCE_{EL}).

$$A_{\text{source}} \approx \text{LCE}_{\text{EL}} N_{\text{source}} \quad (1.28)$$

1102 Therefore, from the measure ratio of signal area in the succeeding window (A_{SW}) to the source
 1103 signal area (A_{source}), the result of which is shown in Fig. 1.36, we can derive the fluorescence ratio
 1104 f_{FR} . P_{SW} is ~ 0.23 with regard to the decay time τ . LCE_{PTFE} is 2.85 % (top PMT: 1.35 %, bottom
 1105 PMT: 1.50 %); LCE_{EL} is 1.70 % (top PMT: 0.85 %, bottom PMT: 0.85 %); and $\text{LCF}_{\text{EL-PTFE}}$ is 79.3 %
 1106 (top cone: 39.0 %, bottom cone: 40.3 %), which are estimated by using the same method as described
 1107 in Section 1.6 using PTFE reflectivity of 0.4. With the ratio of A_{SW} to A_{source} $\sim 0.5 \times 10^{-3}$, f_{FR}
 1108 is $\sim 1.6 \times 10^{-3}$. This result has a big uncertainty (up to 1×10^{-3}) due to statistic errors, and the
 1109 systematic errors in the light collection efficiency and the absorption fraction, resulting from the
 1110 uncertainty in the PTFE reflectivity value.

1111 **Cherenkov radiation** think about gamma particle induced cherenkov, and whether the calcula-
 1112 tion is correct. Cherenkov radiation is the photon radiation process when a charged particle is

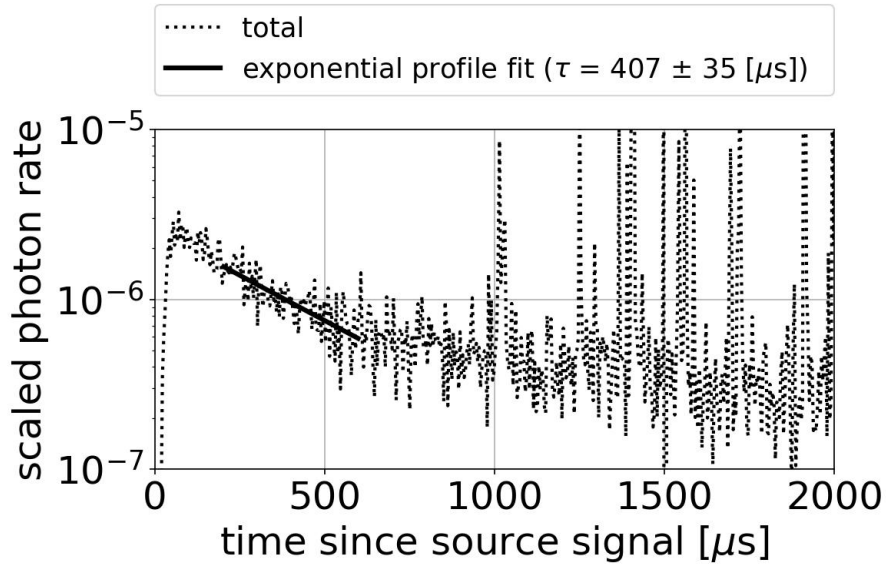


Figure 1.35: The average of scaled waveform in the range of $0 \mu\text{s}$ to $2000 \mu\text{s}$ since source signals. See text for details.

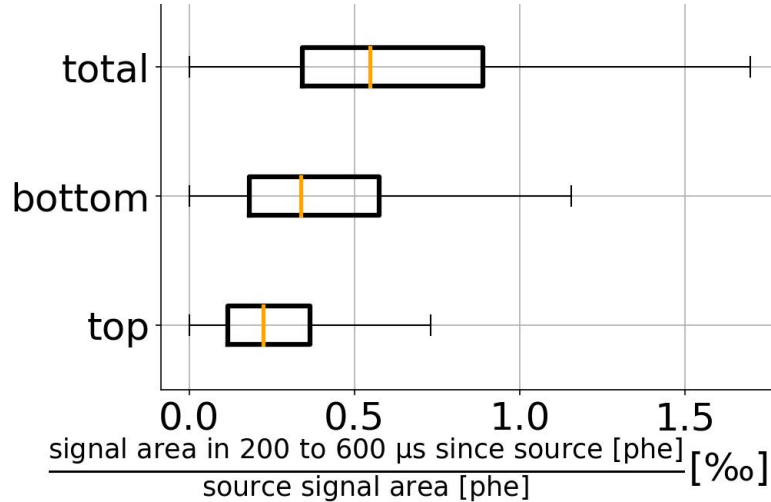


Figure 1.36: The ratio of the number of SPHEs in the range of $200 \mu\text{s}$ to $600 \mu\text{s}$ since source signals to the number of SPHEs in the source signal.

traveling through a medium with its speed higher than the speed of light in the medium. The charged particle could be an external charged particle or electrons that originate from energy loss of external particle in the medium. Because of the photon production in Cherenkov radiation process, especially when this process happens in the PTFE materials (and the PMT windows), it is considered to one of the sources of the signals in *Gas Test*. A cartoon for the physical process and an example waveform of extremely narrow pulse are shown in Fig. 1.37.

The quantity of photon production in Cherenkov radiation process is estimated by its theoretical spectrum following Frank–Tamm formula. A simplified approximation for Frank–Tamm formula from Ref. [Jackson1999] Eqn. 14.133 shows:

$$\frac{dI(\omega)}{dx} = \frac{e^2\omega}{c^2} \left[1 - \frac{1}{\beta^2\epsilon(\omega)} \right] \quad (1.29)$$

where ω is the frequency of Cherenkov radiation, $I(\omega)$ is the energy intensity of frequency ω , $\epsilon(\omega)$ is the relative permittivity of the medium, and β is the speed of the charged particle. ω satisfies that $\beta^2\epsilon(\omega)$ is larger than one, so that the energy intensity is positive. The number intensity $N(\omega)$ can be derived from Eqn. 1.29

$$\frac{dN(\omega)}{dx} = \frac{\alpha}{c} \left[1 - \frac{1}{\beta^2\epsilon(\omega)} \right] \quad (1.30)$$

where $\alpha \equiv e^2/\hbar c \approx 1/137$ is the fine structure constant. The total quantities of photons (N) is the integral over frequency and distance of Eqn. 1.30.

A portion of these Cherenkov radiation photons can be seen by the PMTs, since PTFE is partially transparent to these photons. The duration of Cherenkov radiation event light production is the duration of charged particle energy loss process, which is typically very short (~ 1 ns to 10 ns). The number of photons (A_{Che}) detected by the PMTs for a typical 1 MeV electron is estimated using the following parameters:

$$A_{\text{Che}} \approx N_{\text{Che}} f_{\text{to-surface}} \exp(-d_{\text{to-surface}}/d_{\text{atten}}) \text{LCE}_{\text{PTFE}} \quad (1.31)$$

where N_{Che} is the number of produced Cherenkov radiation photons which the PMTs are sensitive to; $f_{\text{to-surface}}$ is the fraction of Cherenkov radiation photons going toward the PTFE surface; $d_{\text{to-surface}}$ is the distance from the location of Cherenkov radiation produce to the PTFE surface; d_{atten} is the attenuation length of PMT sensitive Cherenkov radiation photons; and LCE_{PTFE} is the light collection efficiency for photons exiting PTFE surfaces.

N_{Che} is related to PMT sensitivity, we take the PMT sensitive photon wavelength in the range of 160 nm to 650 nm (the spectral response range for PMT R11410-10, as described in Ref. [1]). N_{Che} is also related the PTFE refractive index, and electron stopping distance, which are approximately 2 ($\epsilon \sim 4$), and $\sim 10^{-1}$ cm for a 1 MeV electron in PTFE, respectively. The attenuation distance of

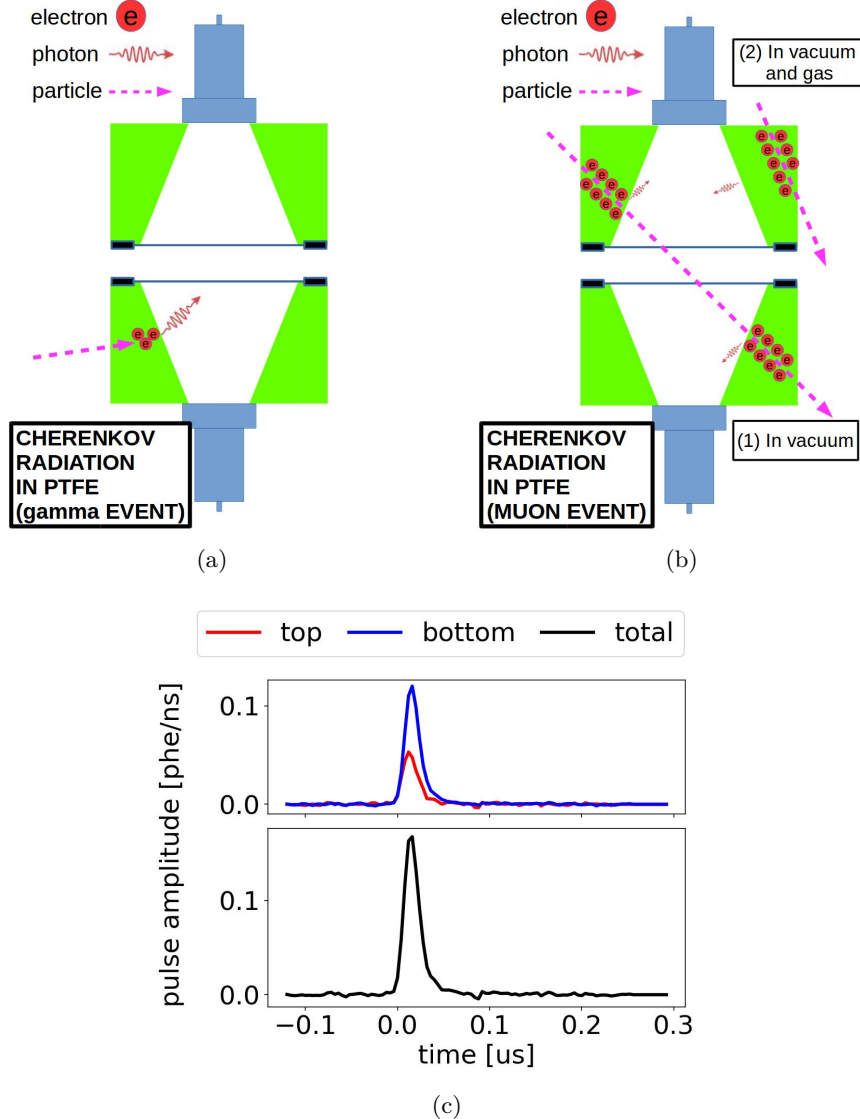


Figure 1.37: *Gas Test* signal: Cherenkov radiation in PTFE. (a) Cartoon of the process in which Cherenkov radiation is produced in PTFE. The Cherenkov radiation comes from the electrons created in a gamma particle event. (b) Cartoon of the process in which Cherenkov radiation is produced in PTFE after a muon particle crossing the detector. (1) If the detector is in vacuum, even though the muon particle crosses the cone regions, there is no primary scintillation or ionization inside the ELD active volume, and only Cherenkov radiation signals from this muon event in PTFE are observed. (2) A muon particle does not cross the cone regions. Cherenkov radiation signals from this muon in PTFE are observed. (c) An example waveform of a Cherenkov radiation event. Data were taken at 2017-12-8 14:02, with grid voltages V_T and V_B at +6 kV and -6 kV, operating gas density at 0.137 mol L^{-1} .

photons d_{atten} is ~ 7 cm for a 1 MeV electron for PTFE, from Ref. [28]. The light collection efficiency LCE_{PTFE} is in the range of 1.5 % to 15 %, as described in Section 1.6. Therefore, taking $d_{\text{to-surface}}$ to be 0 cm to 1 cm, and taking $f_{\text{to-surface}}$ to be 10 % to 50 %, N_{Che} is ~ 150 , and the estimated number of Cherenkov photons detected by the PMTs is in the range of up to ~ 10 phe. Even though this estimated number of photons is not very big, however it is large enough to be seen by both PMTs. For a muon, we can do a similar estimation with changing the stopping distance to the full length of muon trajectory in PTFE, which is ~ 5 cm. Therefore, the estimated number of Cherenkov photons detected by the PMTs in a muon event is in the range of up to ~ 500 phe. The exact number of detected Cherenkov photons is hard to predict precisely because of the complicated geometry of ELD. However, these estimations conclude that Cherenkov events are one of the visible background signals in our detector.

One of the most convincing evidence is the existence of Cherenkov radiation events is that short-duration signals are seen in the detector at vacuum condition. Fig. 1.38a shows the signal t_{01-99} duration vs. signal area plot from a dataset with grid voltages V_T and V_B at 0kV, operating gas density at vacuum. The black box shows the potential events which are considered to be associated with Cherenkov radiation process. Since the detector is at vacuum condition, it is lack of other photon production processes. These potential Cherenkov radiation events may source from both external charged particles and energy loss of external particles, likely an external higher energy photon (gamma radiation), or a cosmic ray muon. This process is described below: An external particle travels through the PTFE cones, lose its energy, ionizes molecules in PTFE and radiates photon along its trajectory. Since muon particles are usually more energetic than other external particles like gamma radiation, the Cherenkov radiation from muon events is usually larger. This is one explanation for the “hot spot” at $(10^2, 10^2)$ in Fig. 1.38a. When the detector is filled with xenon gas, the muon particle can also ionize xenon gas atoms inside ELD active volume. This process produces scintillation photons and ionization electrons, and the EL process associated with ionization electrons usually increases signal duration. It explains the reason that this “hot spot” shifts between vacuum data and xenon gas data. Details for explanations of muon events in xenon gas data are in Section ???. The signals with their area in the range of 0 phe to 10^2 phe and signal duration in the range of 0 ns to 2×10^2 ns in Fig. 1.38a are likely to be Cherenkov radiation events from muons that do not cross the ELD active region and external gamma radiation induced fast electrons in PTFE (and PMT window). The gamma radiation can scatter electrons in PTFE. These fast-moving scattered electrons can also produce Cherenkov radiation light. When the detector is filled with xenon gas, the same physical processes of Cherenkov radiation from muon and gamma radiation remain. Therefore, these processes explain why a similar population of Cherenkov radiation events exist in both vacuum data (Fig. 1.38a) and xenon gas data (Fig. 1.38b).

Discharge Discharges happen inside and outside the ELD could produce signals that can be seen by the PMTs. In sparking tests, we observe discharges on the high voltage feed throughs and cables,

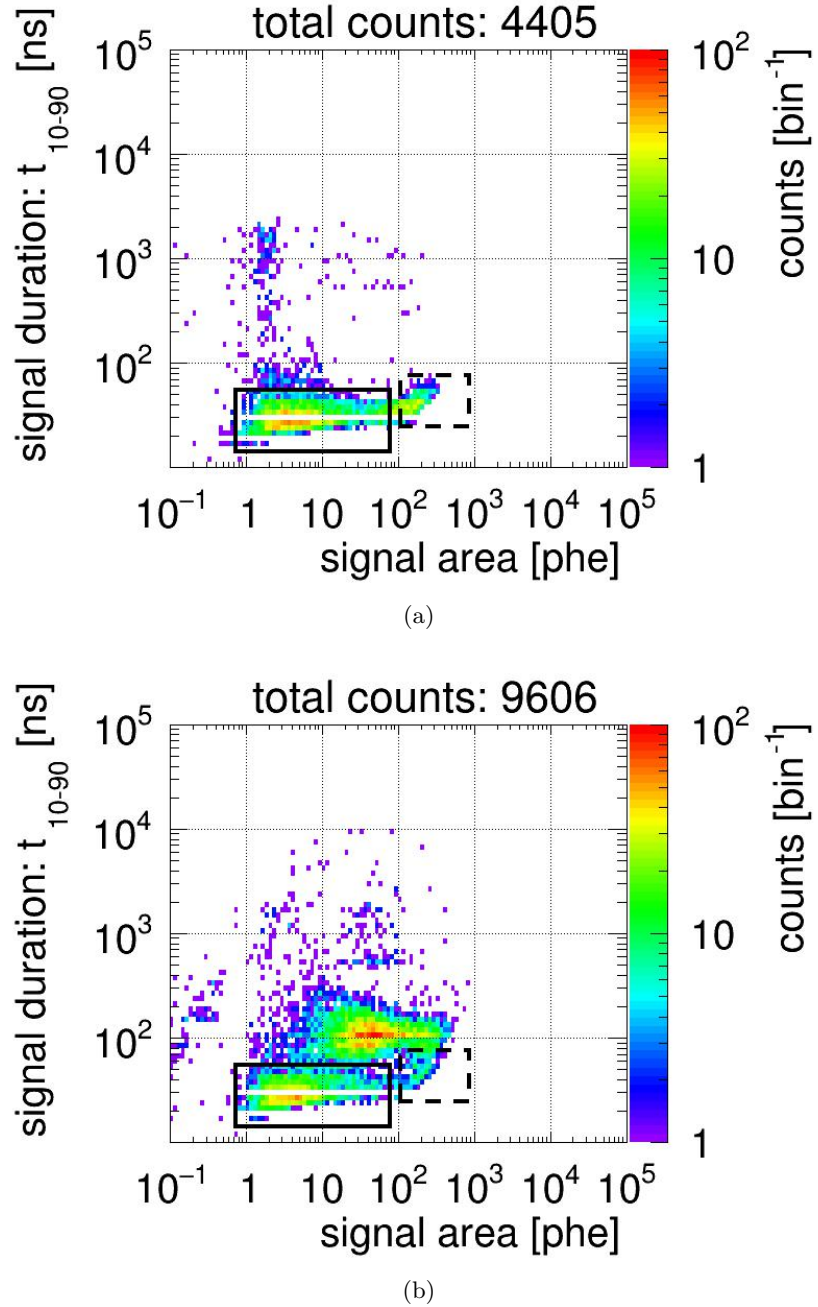


Figure 1.38: *Gas Test* signal t_{10-90} duration vs. signal area. (a) Vacuum data. Data were taken at 2018-03-12 11:41, with grid voltages V_T and V_B at 0 kV, operating gas density at vacuum. (b) Xenon gas data. Data were taken at 2017-12-8 13:12, with grid voltages V_T and V_B at 0 kV, operating gas density at 0.137 mol L^{-1} . The black solid line indicates the muon events which crosses the cone regions. The black dashed line indicates the muon events which do not cross the cone regions, and might also include gamma radiation events in PTFE.

1179 which are caused by the smoothness of the high voltage surfaces (especially metallic surfaces) are
1180 imperfect. This imperfection creates a high field region, and initialized a high
1181 ionization probability of the medium (especially gas medium) surrounding it and causes a discharge.
1182 The quantity of light production of these discharges has a various range and usually are big. However,
1183 depending on the location of the discharge, signals of the discharge have different appearances. The
1184 discharges happening outside the ELD may end up having one or several SPHEs in each PMTs with
1185 regard to the poor light collection at such location. However, the discharges happening inside the
1186 ELD may look like electron emission signals.

1187 1.9 Signal selections

1188 This section discusses signal selections, also known as cuts, that are used in the *Gas Test* analysis.
1189 The purpose of this analysis is searching for electron emission signals from tested grid wires, and
1190 correctly estimating the rate of this process. For this purpose, signal selections on different parameter
1191 spaces are carried out to identify background signals from electron emission signals. **For each signal**
1192 **selection, the possibility of removing electron emission signalis evaluated.** The primary principle of
1193 signal selections is to get a clean population distribution of electron emission signal to get a reliable
1194 estimation of its rate. Other than that, since electron emission signals are in most situation rare in
1195 the detector, signal selections of these electron emission signals are done conservatively; that is to
1196 keep as many candidates for electron emission signals as possible.

1197 An electron emission signal should:

- 1198 • have the correct signal shape.
1199 • be an uncorrelated signal from previous signals in time, and

1200 Based on the characteristics we summarize previously about electron emission signal and other
1201 different signals in the detector, a list of selections to get electron emission signals are carried out
1202 and discussed.

1203 1.9.1 Signal selections based on signal shape

1204 Signal shape is one of the most important signature for electron emission signals . It includes the
1205 aspects of the signal area, the signal duration, and the SPHE rate at different time region during
1206 the event.

1207 Coincidence found

1208 **Definition** Both PMTs have signals that occur within a time difference smaller than CWW.

1209 **Purpose** This is to make sure that the signal of interest is unlikely to be from a dark current
1210 signal in one PMT, or SPHE from other sources in one PMT (e.g. fluorescence light from PTFE,
1211 discharges).

1212 The process of coincidence found and coincidence event building is discussed in the data processing
1213 section in Section 1.4. An example of coincidence event building result is shown in Fig. 1.39a.
1214 The signal area has a various distribution mostly in the range of 10^{-1} phe to 10^5 phe, when the
1215 signal t_{10-90} duration, and the TBA, top-bottom asymmetry, are mostly distributed in the range of
1216 10^1 ns to 10^5 ns and -1 to 1 . Several “hot spots” that are seen in the figure correspond to different
1217 activities in the detector, which will be explained later in each separate section of signal selection.
1218 Among these “hot spots”, the horizontal strap shape spot at signal area in the range of 10^1 phe to
1219 10^2 phe, signal t_{10-90} duration in the range of 10^3 ns to 10^4 ns, is likely to contain the potential elec-
1220 tron emission signals. The locations and the counts of different “hot spots”, including the “hot spot”
1221 of electron emission signals, change as varying ΔV_{T-B} and operating gas density, mainly because of
1222 the changes of the duration and the intensity of the EL process.

1223 Coincidence found and coincidence event building are the fundamental part of this analysis.
1224 Signal selections defined later are based on the classification of coincidence-found signals.

1225 Not a noise-like signal

1226 **Definition** A coincidence-found signal has a positive signal area in all PMT channels, a higher
1227 than 0.5 positive to negative amplitude ratio, and a positive signal t_{10-90} duration.

1228 **Purpose** This is to make sure the signal of interest is not an electrical noise signal, which usually
1229 has a close to zero signal area, a close to unity positive to negative amplitude ratio, or a zero signal
1230 t_{10-90} duration, as described in Section 1.8.4. The effect of this selection is shown in Fig. 1.39b.
1231 Noise-like signals, mostly at signal area in the range of <1 phe, signal t_{10-90} duration in the range
1232 of $<10^3$ ns, are rejected.

1233 Not a narrow (S1-like) signal

1234 **Definition** A coincidence-found signal has a signal t_{25-75} width (time difference between the time
1235 of 25th percentile of the signal waveform and the time of 75th percentile of the signal waveform)
1236 larger than 250 ns, and a signal t_{50} width (time difference between the signal start time and the time
1237 of 50th percentile of the signal waveform) larger than 320 ns; in other words, the major width of the
1238 coincidence-found signal is not narrow.

1239 **Purpose** This is to make sure the signal of interest is not a potential (1) Cherenkov radiation event,
1240 or (2) primary scintillation light (S1) from an external particle (e.g. gamma radiation, muon), as
1241 described in Section 1.8.4, Section 1.8.2, and Section 1.8.3. The effect of this selection is shown in

1242 Fig. 1.39c. The narrow signals can generally be separated to two categories, corresponding to the
 1243 two “hot spots” in the figure. The first “hot spot” at signal area in the range of 1 phe to 10^2 phe,
 1244 signal t_{10-90} duration in the range of $<5 \times 10^1$ ns, may results from Cherenkov radiation events and
 1245 primary scintillation light of low energy gamma radiation events. The second “hot spot” at signal
 1246 area 10^1 phe to 10^3 phe, signal t_{10-90} duration in the range of 5×10^1 ns to 2×10^2 ns are likely from
 1247 primary scintillation light of gamma radiation events and muon events.

1248 **Not a two-SPHE accidental coincidence signal**

1249 **Definition** A coincidence-found signal has a signal area larger than 2.5 phe, and at least one PMT
 1250 has a signal t_{25-75} width larger than 35 ns, which is approximately twice the signal width of a SPHE.

1251 **Purpose** This is to make sure the signal of interest is not a accidental coincidence of two SPHEs,
 1252 which are likely from PMT dark current and other SPHE sources (e.g. PTFE fluorescence, dis-
 1253 charges), as described in Section 1.8.4, Section 1.8.4, and Section 1.8.4. The effect of this selection
 1254 is shown in Fig. 1.39d. Two-SPHE accidental coincidence signals, mostly at signal area in the range
 1255 of <2.5 phe, signal t_{10-90} duration in the range of up to $\sim 2 \times 10^3$ ns (this upper edge results from
 1256 coincidence window width (CWW) in coincidence building), are rejected.

1257 **Not a top-heavy signal**

1258 **Definition** A coincidence-found signal does not have a ”top-heavy” TBA regarding its signal area.
 1259 A signal area dependent cut on TBA is used rather than a fixed TBA value is to account for the
 1260 statistically fluctuation of the TBA at low signal area region, because the counts of photons that
 1261 the top and bottom PMT detected are low.

1262 A ”top-heavy” TBA is defined as assuming the photon counts in top PMT (T) has a binomial
 1263 distribution of parameter p (success probability in a single trial) and N (number of trials), the
 1264 survival function (SF) at $T = T_{\text{detected}}$ is smaller than 10^{-5} :

$$SF(T_{\text{detected}}) \equiv P(T > T_{\text{detected}}) = \sum_{T_{\text{detected}}}^{\infty} P(T) dT < 10^{-5} \quad (1.32)$$

$$P(T; p, N) = \binom{N}{T} p^T (1-p)^{N-T} \quad (1.33)$$

1265 where $p = B_{\text{detected}} \times 1.025/N$; T_{detected} , B_{detected} are the top and bottom PMT measured signal
 1266 area in phe; N is a sufficiently large number, chosen to be 10^6 . A low SF (T_{detected}) indicates a high
 1267 TBA.

1268 **Purpose** This is to make sure the signal of interest is not from (1)an anode cone event, (2) an
 1269 anode muon cone event, (3) a PMT saturation event, or (4) a signal which misses part of the

recording in the bottom PMT (likely because of PMT dead time), as described in Section 1.8.2, Section 1.8.3, and Section 1.2. The effect of this selection is shown in Fig. 1.39e. The four categories of background events, correspond to the four “hot spots” in the figure.

The “hot spot” at signal area in the range of 10^2 phe to 10^3 phe, signal t_{10-90} duration in the range of $\sim 10^3$ ns to 10^4 ns, and TBA ~ 0.3 , results from EL light in the anode cone gamma radiation events. This “hot spot” is a combination of two smaller “hot spots”. The “hot spot” on the left (signal area $\sim 2 \times 10^2$ phe, signal t_{10-90} duration $\sim 2 \times 10^3$ ns, and TBA ~ 0.3) may result from xenon X-rays events with typical energy of 33 keV in the anode cone . A xenon X-ray event in average can create $\sim 1.5 \times 10^3$ drifted electrons ⁴, which produce EL light in the high electric field region around the anodic grid wires. The “hot spot” on the right corresponds to other higher energy gamma radiation.

The location of this “hot spot” in the figure moves as varying ΔV_{T-B} . As ΔV_{T-B} increases, the electric field strength around the anodic grid wires also increases, which causes higher quantity of EL light production and signal area. At a low ΔV_{T-B} , the small area signals cannot be rejected by this selection. Therefore, another signal selection based on the time correlation between the signal of primary scintillation and the signal of EL of these events, is carried out, as described later in Section 1.9.2.

The “hot spot” at signal area $\sim 10^4$ phe, signal t_{10-90} duration $\sim 10^4$ ns, results from EL light in the anode cone muon events. Similar to anode cone event from gamma radiation, these events also free drifted electrons, which produce EL light in the high elelctric field region around the anodic grid wires. The duration of these muon events are much longer than that of gamma events is because the longer ionization track of a muon event causes the drifted electrons created in the muon event arrive the anodic grid and produce EL light in a wider time span, as described in Section 1.8.3. The location of this “hot spot” in the figure moves to high signal area as increasing ΔV_{T-B} . Therefore, the same argument holds for the signal selection based on the time correlation is used to reject these signals.

The “hot spot” strap at signal area $\sim 10^4$ phe, signal t_{10-90} duration $\sim 10^3$ ns, and TBA ~ 0.1 results from high energy particle and muon events which saturate the DAQ. Because the average SPHE amplitude in the bottom PMT is higher, it exceeds the upper limit of the DAQ dynamic range at a smaller counts of SPHE than the top PMT. Therefore, the reconstructed signal area in the bottom PMT is lower after it reaches the DAQ saturation limit, which leads to a higher signal TBA because of this DAQ saturation issue.

The “hot spot” at TBA ~ 1 results from missing part of the recording in the bottom PMT ,which is most likely because of PMT dead time. In these signals, the top PMT records the full event, when the bottom PMT only records the beginning or the end of the event. This results in a close to unity signal TBA.

⁴The average energy to create an electron-ion pair in xenon gas (W_{ion}) is 22 eV for a gamma particle, estimated from W_{ion} for an alpha particle and a beta particle in Ref. [24–26].

1306 **Not a bottom-heavy signal**

1307 **Definition** A coincidence-found signal does not have a "bottom-heavy" TBA regarding its signal
1308 area.

1309 Similar to the "top-heavy" TBA, a "bottom-heavy" TBA is defined as assuming the photon
1310 counts in bottom PMT (B) has a binomial distribution of parameter p (success probability in a
1311 single trial) and N (number of trials), the survival function (SF) at $B = B_{\text{detected}}$ is smaller than
1312 10^{-5} :

$$SF(B_{\text{detected}}) \equiv P(B > B_{\text{detected}}) = \sum_{B_{\text{detected}}}^{\infty} P(B) dB < 10^{-5} \quad (1.34)$$

$$P(B; p, N) = \binom{N}{B} p^B (1-p)^{N-B} \quad (1.35)$$

1313 where $p = T_{\text{detected}}/0.825/N$; T_{detected} , B_{detected} are the top and bottom PMT measured signal area
1314 in phe; N is a sufficiently large number, chosen to be 10^6 . A low SF (B_{detected}) indicates a low TBA.

1315 **Purpose** This is to make sure the signal of interest is not a signal which misses part of the recording
1316 in the top PMT (likely because of PMT dead time), as described in Section 1.2, which is similar to
1317 the situation described in Section 1.9.1.

1318 The effect of this selection is shown in Fig. 1.39f. Signals with TBA close to -1 are rejected
1319 because they are likely to be a signal missing part of the recording in the top PMT.

1320 In reverse polarity operation when the top grid is cathodic and the bottom grid is anodic, the
1321 roles of "top-heavy" and "bottom-heavy" signal selections switches from normal polarity operation.

1322 **Not a extremely long duration signal**

1323 **Definition** A coincidence-found signal has a signal t_{01-99} duration 4 times longer than the pre-
1324 dicted EL duration from the estimated average EL region electric field and Eqn. 1.17.

1325 **Purpose** This is to make sure the signal of interest is not a muon event or a multiple scatter event,
1326 as described in Section 1.8.3, and Section 1.8.2. The effect of this selection is shown in Fig. 1.39g.
1327 The "hot spot" at signal area $\sim 10^4$ phe, signal t_{10-90} duration $\sim 3 \times 10^3$ ns, and TBA ~ 0 results
1328 from EL region muon events.

1329 **Not a right-angle triangle shape signal**

1330 may be remove this cut.

1331 **Definition** A coincidence-found signal does not have a large skewness of signal waveform and a
1332 higher photon rate at the beginning of the signal than that at the end of the signal.

1333 The skewness statistics of a electron emission signal waveform is close to zero because the shape is
 1334 close to a uniform distribution, when the skewness of a right-angle triangle shape is ~ 0.96 . Therefore,
 1335 this statistics is used to distinguish the right-angle triangle waveform. The skewness statistics
 1336 between 5th percentile time and 95th percentile time (skew_{0595}) and the skewness statistics between
 1337 15th percentile time and 85th percentile time (skew_{1585}) are used to effect from the outlier. A large
 1338 skewness is defined as $\text{skew}_{0595} > 0.2$ and $\text{skew}_{1585} > 0.1$.

1339 Since the skewness statistics are sometimes effected by outlier, another method is carried out
 1340 based on comparing the photon rate the beginning of the signal and that at the end of the signal
 1341 as a supplement. A higher photon rate at region A than region B is defined below. The detected
 1342 signal area and duration of region A and region B is noted as A_{detected} , B_{detected} , t_A , t_B . Assuming
 1343 the photon counts in region A in a simulation (A_{sim}) has a binomial distribution of parameter p
 1344 (success probability in a single trial) and N (number of trials), the survival function (SF) at $A_{\text{sim}} =$
 1345 A_{detected} is smaller than 10^{-6} :

$$SF(A_{\text{detected}}) \equiv P(A_{\text{sim}} > A_{\text{detected}}) = \sum_{A_{\text{detected}}}^{\infty} P(A) dA < 10^{-6} \quad (1.36)$$

$$P(A; p, N) = \binom{N}{A} p^A (1-p)^{N-A} \quad (1.37)$$

1346 where $p = 1.2 \times B_{\text{detected}} \times t_A / t_B / N$; N is a sufficiently large number, chosen to be 10^6 . A low SF
 1347 (A_{detected}) indicates a higher photon rate at region A than region B. If the photon rate between 5th
 1348 percentile time and 15th percentile time, or between 300 ns and 800 ns since the recording start time
 1349 of the event is higher than that of between 50th percentile time and 85th percentile time, we define
 1350 the signal has the photon rate at the beginning is higher than that at the end.

1351 **Purpose** This is to make sure the signal of interest is not a EL region muon event, or a S1 S2
 1352 event in the EL region, as described in Section 1.8.3, and Section 1.8.2. The muon events happening
 1353 between the grid rings has a lower light production and light collection than those happing between
 1354 the grid wires. These grid ring region events usually does have a "long tail" in the signal because the
 1355 muon track does not pass the anode region creating free drifted electrons. These two reasons make
 1356 it hard to distinguish muon events happening between the grid rings by a long signal duration or a
 1357 large signal area as that between the grid wires. The effect of this selection is shown in Fig. 1.39h.
 1358 Therefore, this pulse selection is used.

1359 **Not an S1 S2 like signal**

1360 **may be remove this cut.**

1361 **Definition** A coincidence-found signal does not have a low photon rate in the range of 300 ns to
1362 800 ns since the recording start time of the signal.

1363 Since in this type of events, the photon rate is low between the S1 and S2 signal, we compare the
1364 photon rate in the time region immediately after S1 to other time region to distinguish these events.
1365 An S1 signal usually lasts less than 180 ns, therefore ending 300 ns after the recording start time
1366 of the signal, because of the pre-delay recording described in Section ???. The compared region are
1367 between 800 ns since the recording start time of the signal and 90th percentile time, between 25th
1368 percentile time and 90th percentile time, between 50th percentile time and 75th percentile time, and
1369 between 50th percentile time and 95th percentile time.

1370 **Purpose** This is to make sure the signal of interest is not from an S1 S2 event in the cathode
1371 corner, as described in Section 1.8.2. The effect of this selection is shown in Fig. 1.39i.

1372 Not a saturated signal

1373 **Definition** A coincidence-found signal does not have any PMT saturated.

1374 **Purpose** This is to make sure the signal of interest is not from a particle or muon event that have
1375 large signal area, unlike electron emission signal which usually does not produce large signal that
1376 saturate any PMT. The effect of this selection is shown in Fig. 1.39j.

1377 Not a long duration signal

1378 **Definition** A coincidence-found signal has a signal t_{10-90} duration 1.5 times longer than the
1379 predicted electron emission signal signal t_{10-90} duration from the estimated average EL region
1380 electric field and Eqn. 1.17.

1381 **Purpose** This is to make sure the signal of interest is not a muon event or a multiple scatter event,
1382 as described in Section 1.8.3, and Section 1.8.2. The effect of this selection is shown in Fig. 1.39k.

1383 Not a short duration signal

1384 **Definition** A coincidence-found signal has a signal t_{10-90} duration shorter than 0.64 times the
1385 predicted electron emission signal duration from the estimated average EL region electric field and
1386 Eqn. 1.17, and shorter than 5 sigma from the predicted electron emission signal signal t_{10-90} duration
1387 duration.

1388 **Purpose** This is to make sure the signal of interest is not a grid ring region event (likely originating
1389 from muon or particle), as described in Section 1.8.3, and Section 1.8.2. The effect of this selection
1390 is shown in Fig. 1.39l. An event happening in the grid ring region has a low light collection therefore

1391 hard to be distinguished by its shape. However, it usually has a shorter duration, therefore can be
1392 rejected by this pulse selection.

1393 1.9.2 Signal selections based on previous signals

1394 Previous signals may correlate with the later signals. There are two major types of correlation
1395 signals. One type of correlation signals is between primary scintillation light and EL light from
1396 the ionization electrons. In an anode cone region event, primary scintillation light are produced
1397 immediately after a particle interaction, when the ionization electrons take time to drift to the
1398 anodic grid to produce EL light, as described in Section 1.8.2 and Section 1.8.3. Therefore, we
1399 can the correlation between primary scintillation light and EL light to determine these events. The
1400 second type of correlation signals is fluorescence signals succeeding large-area signals, as described in
1401 Section 1.8.4. Since the fluorescence signals may look like electron emission signals, the correlation
1402 between the fluorescence signals and the large-area signals is the only method to distinguish these
1403 fluorescence signals. Therefore, we use signal selections based on the previous signal area to reject
1404 these background events.

1405 Moreover, previous signals also introduce PMT dead time issue, as described in Section 1.2.
1406 PMT dead time issue causes an incomplete recording of the signals immediately following another
1407 signal. To address this issue, we subtract a segment of time after each recorded pulse from the live
1408 time of study and eliminate all signals that is recorded in this time period. Therefore, we use signal
1409 selections based on the previous signal duration to reject these background events.

1410 These two signal selections previously mentioned may veto good candidate electron emission
1411 signals . Therefore, the survival ratio of the candidate electron emission signals from these signal
1412 selection is estimated.

1413 Veto based on signal area of previous signal

1414 **Definition** A coincidence-found signal (1) is not following another pulse in any PMT with pulse
1415 area larger than 3.5 phe within $150\ \mu s$, (2) is not following another pulse in any PMT with pulse
1416 area larger than 10^3 phe within $300\ \mu s$, and (3) is not following another pulse in any PMT with pulse
1417 area larger than 10^4 phe within $1000\ \mu s$.

1418 **Purpose** The 100-us veto is to make sure that the signal of interest is not the EL light from an
1419 anode cone region event, as described in Section 1.8.2 and Section 1.8.3. Primary scintillation light
1420 signal in an anode cone region event mostly has its pulse area larger than 3 phe in at least one
1421 PMT. Therefore, this veto can reject the anode cone region event background. The 200-us veto and
1422 the 1000-us veto are to make sure that the signal of interest is not fluorescence signals succeeding
1423 large-area signals, as described in Section 1.8.4. With the segment of time cut off, the fluorescence
1424 induced SPHE rate is below 10^4 Hz, therefore the rate of accidental coincidence with more than

1425 3 phe is below 4 Hz for the chosen CWW. The effect of this selection is shown in Fig. 1.39m. Even
1426 though not shown in this figure, this selection is also effective in removing the “hot spot” at signal
1427 area in the range of 10^2 phe to 10^3 phe, signal t_{10-90} duration in the range of $\sim 10^3$ ns to 10^4 ns, and
1428 TBA ~ 0.3 , resulting from EL light in the anode cone gamma radiation events, which is shown in
1429 Fig. 1.39e. This selection is necessary when ΔV_{T-B} is small because the signal selection based on
1430 TBA is less effective in such ΔV_{T-B} , as discussed in Section 1.9.1 .

1431 **Veto based on signal area of previous signal**

1432 **Definition** A coincidence-found signal (1) is not following another pulse in any PMT within $10\ \mu s$,
1433 (2) is not following another pulse in any PMT with pulse duration longer than $3\ \mu s$ within $20\ \mu s$, (3)
1434 is not following another pulse in any PMT with pulse duration longer than $10\ \mu s$ within $40\ \mu s$, and
1435 (4) is not following another pulse in any PMT with pulse duration longer than $30\ \mu s$ within $200\ \mu s$.

1436 **Purpose** This is to make sure the PMT dead time issue is addressed. The effect of this selection
1437 is shown in Fig. ??.

1438 **Survival ratio of the candidate electron emission signals**

1439 These two cuts previously mentioned may veto good candidate electron emission signals . Therefore,
1440 survival ratio of the candidate electron emission signals need to be estimated. The survival ratio is
1441 estimated by how much is the fraction of a careful selection of coincidence pulses survive these cuts.
1442 The careful selection of coincidence pulses also need to be uncorrelated from preceding pulses. The
1443 careful selection is the coincidence pulses in t_{25-75} range 0 ns to 200 ns, pulse area range 25 phe to
1444 250 phe. This selection is a conservative selection of S1 pulses that has few contaminations from other
1445 sources. Since S1 is from the primary light production of external particle sources, this selection of
1446 pulses are uncorrelated from preceding pulses. Thus, it can be used for estimating the survival ratio.
1447 The survival ratio is called quiet fraction (QF). For normal operation, QF is in the range of 0.6 to
1448 0.9. Details of this physical sources of S1 pulses will be discussed in the following Section. 1.9.1: S1
1449 conservative population.

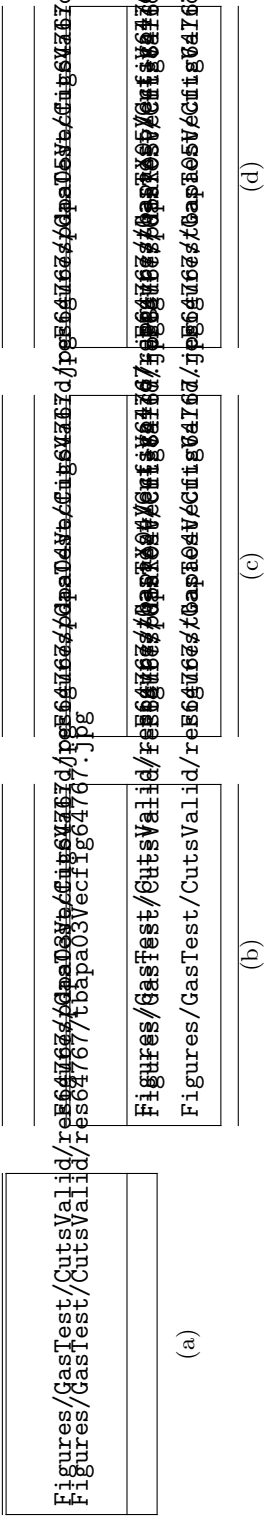


Figure 1.39: *Gas Test* signal selection (part 1): (row one) distribution of t_{10-90} duration vs area after signal selections; (row two) distribution of TBA vs area after signal selections; (row three) distribution of t_{10-90} duration vs area of removed signals; (row four) distribution of TBA vs area of removed signals; (a) coincidence event building; (b) applying signal selections up to “not a noise-like signal”; (c) applying signal selections up to “not a narrow (S1-like) signal”; (d) applying signal selections up to “not a two-SPHE accidental coincidence signal”. Data were taken at 2017-12-8 14:02, with grid voltages V_T and V_B at +6 kV and -6 kV, operating gas density at 0.137 mol L^{-1} . The duration of data taking is 180.09 s.

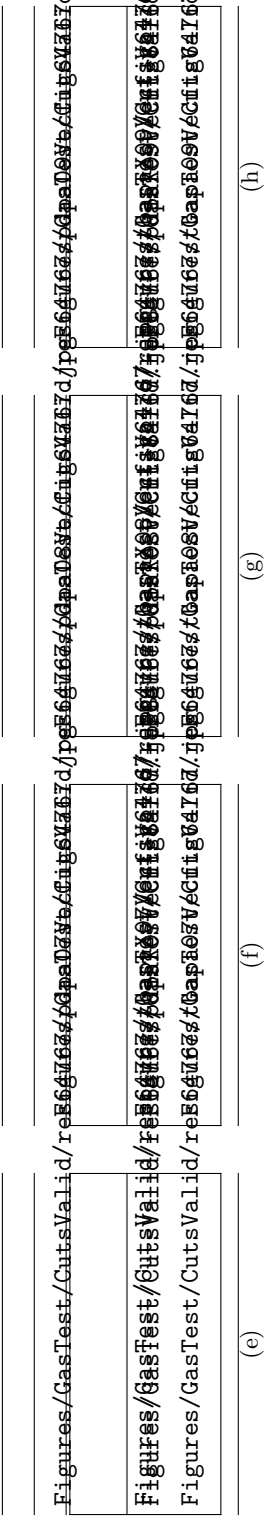


Figure 1.39: *Gas Test* signal selection (part 2): (row one) distribution of t_{10-90} duration vs area after signal selections; (row two) distribution of TBA vs area after signal selections; (row three) distribution of t_{10-90} duration vs area of removed signals; (row four) distribution of TBA vs area of removed signals; (e) applying signal selections up to “not a top-heavy signal”; (f) applying signal selections up to “not a bottom-heavy signal”; (g) applying signal selections up to “not a extremely long duration signal”; (h) applying signal selections up to “not a right-angled triangle shape signal”. The red hatched shaded area indicates the “top-heavy” region. The blue shaded area indicates the “bottom-heavy” region. Data were taken at 2017-12-8 14:02, with grid voltages V_T and V_B at +6 kV and -6 kV, operating gas density at 0.137 mol L^{-1} . The duration of data taking is 180.09 s.

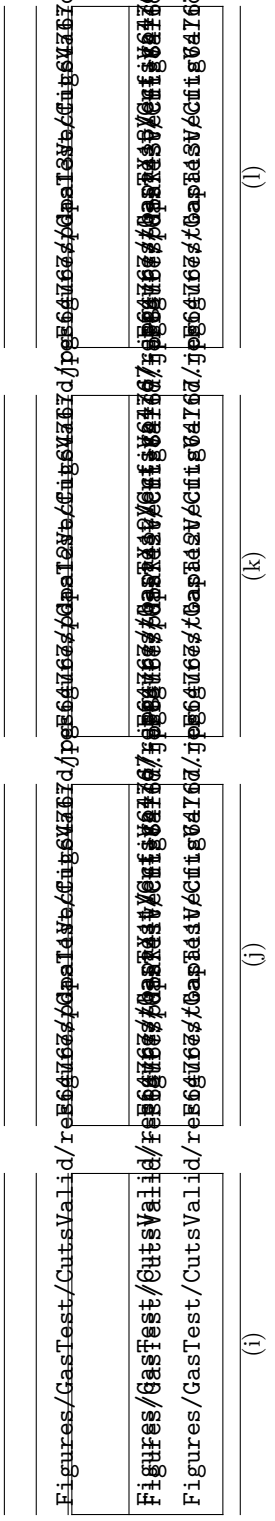


Figure 1.39: *Gas Test* signal selection (part 3): (row one) distribution of t_{10-90} duration vs area after signal selections; (row two) distribution of TBA vs area after signal selections; (row three) distribution of t_{10-90} duration vs area of removed signals; (row four) distribution of TBA vs area of removed signals; (i) applying signal selections up to “not an S1 S2 like signal”; (j) applying signal selections up to “not a saturated signal”; (k) applying signal selections up to “not a long duration signal”; (l) applying signal selections up to “not a short duration signal”. The red hatched shaded area indicates the “top-heavy” region. The blue shaded area indicates the “bottom-heavy” region. The magenta hatched shaded area indicates the “long duration” region. The cyan hatched shaded area indicates the “short duration” region. Data were taken at 2017-12-8 14:02, with grid voltages V_T and V_B at +6kV and -6kV, operating gas density at 0.137 mol L⁻¹. The duration of data taking is 180.09 s.

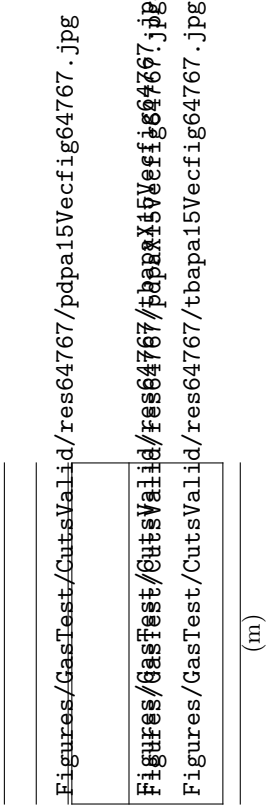


Figure 1.39: *Gas Test* signal selection (part 4): (row one) distribution of t_{10-90} duration vs area after signal selections; (row two) distribution of TBA vs area after signal selections; (row three) distribution of t_{10-90} duration vs area of removed signals; (row four) distribution of TBA vs area of removed signals; (m) applying signal selections up to “time veto selection 1”. The red hatched shaded area indicates the “top-heavy” region. The blue shaded area indicates the “bottom-heavy” region. The magenta hatched shaded area indicates the “long duration” region. The cyan hatched shaded area indicates the “short duration” region. Data were taken at 2017-12-8 14:02, with grid voltages V_T and V_B at +6 kV and -6 kV, operating gas density at 0.137 mol L⁻¹. The duration of data taking is 180.09 s.

¹⁴⁵⁰ **1.9.3 Signal selections varying ΔV_{T-B} and operating gas density**

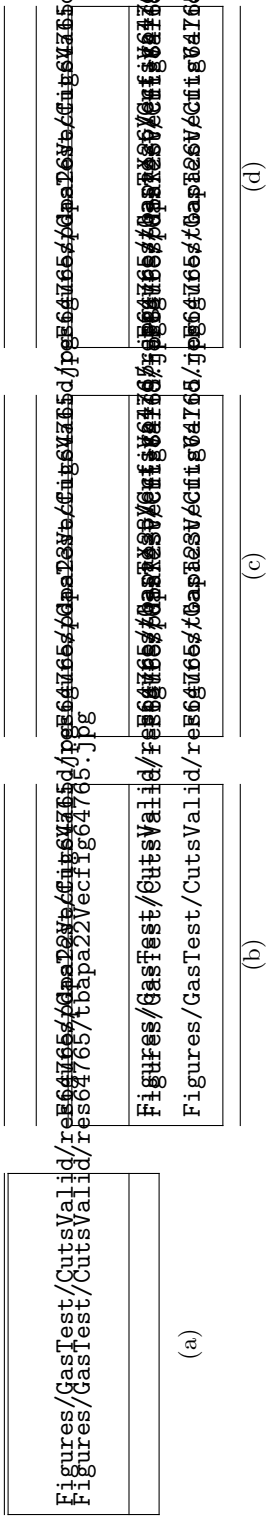


Figure 1.40: *Gas Test* signal selection with ΔV_{T-B} at 8 kV, operating gas density at 0.137 mol L^{-1} : (row one) distribution of t_{10-90} duration vs area after signal selections; (row two) distribution of TBA vs area after signal selections; (row three) distribution of t_{10-90} duration vs area of removed signals; (row four) distribution of TBA vs area of removed signals; (a) coincidence event building; (b) applying signal shape selections based on signal shape; (c) applying signal shape selections based on the previous signals; (d) applying signal shape selections based on signal shape and based on the previous signals. The red hatched shaded area indicates the “top-heavy” region. The blue shaded area indicates the “bottom-heavy” region. The magenta hatched shaded area indicates the “long duration” region. The cyan hatched shaded area indicates the “short duration” region. Data were taken at 2017-12-8 13:43, with grid voltages V_T and V_B at +4 kV and -4 kV. The duration of data taking is 179.95 s.

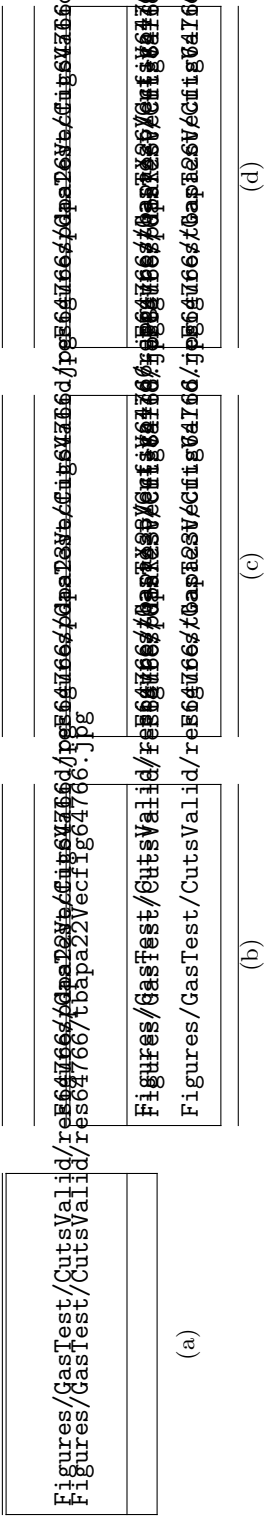


Figure 1.41: *Gas Test* signal selection with ΔV_{T-B} at 10kV, operating gas density at 0.137 mol L^{-1} : (row one) distribution of t_{10-90} duration vs area after signal selections; (row two) distribution of TBA vs area after signal selections; (row three) distribution of t_{10-90} duration vs area of removed signals; (row four) distribution of TBA vs area of removed signals; (a) coincidence event building; (b) applying signal selections based on signal shape; (c) applying signal selections based on the previous signals; (d) applying signal selections based on signal shape and based on the previous signals. The red hatched shaded area indicates the “top-heavy” region. The blue shaded area indicates the “bottom-heavy” region. The magenta hatched shaded area indicates the “long duration” region. The cyan hatched shaded area indicates the “short duration” region. Data were taken at 2017-12-8 13:52, with grid voltages V_T and V_B at +5kV and -5kV. The duration of data taking is 180.11s.

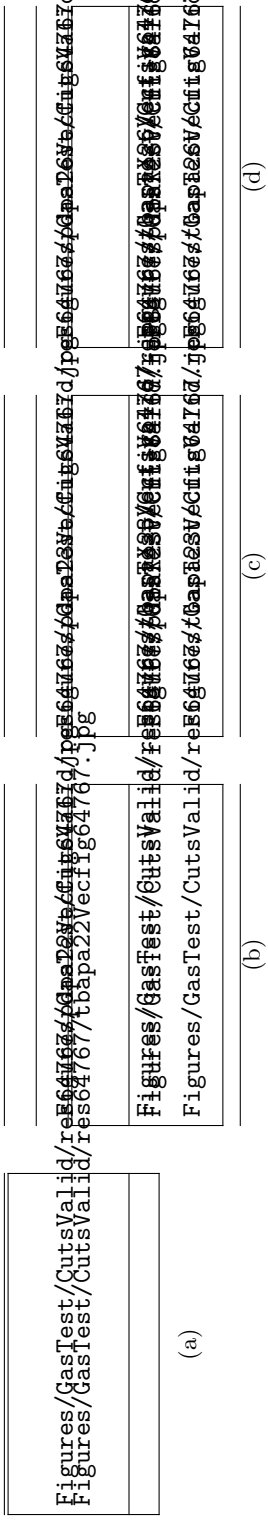


Figure 1.42: *Gas Test* signal selection with ΔV_{T-B} at 12 kV, operating gas density at 0.137 mol L^{-1} : (row one) distribution of t_{10-90} duration vs area after signal selections; (row two) distribution of TBA vs area of removed signals; (row three) distribution of t_{10-90} duration vs area of removed signals; (row four) distribution of TBA vs area of removed signals; (a) coincidence event building; (b) applying signal selections based on signal shape; (c) applying signal selections based on the previous signals; (d) applying signal selections based on signal shape and based on the previous signals. The red hatched shaded area indicates the “top-heavy” region. The blue shaded area indicates the “bottom-heavy” region. The magenta hatched shaded area indicates the “long duration” region. The cyan hatched shaded area indicates the “short duration” region. Data were taken at 2017-12-8 14:02, with grid voltages V_T and V_B at +6 kV and -6 kV. The duration of data taking is 180.09 s.

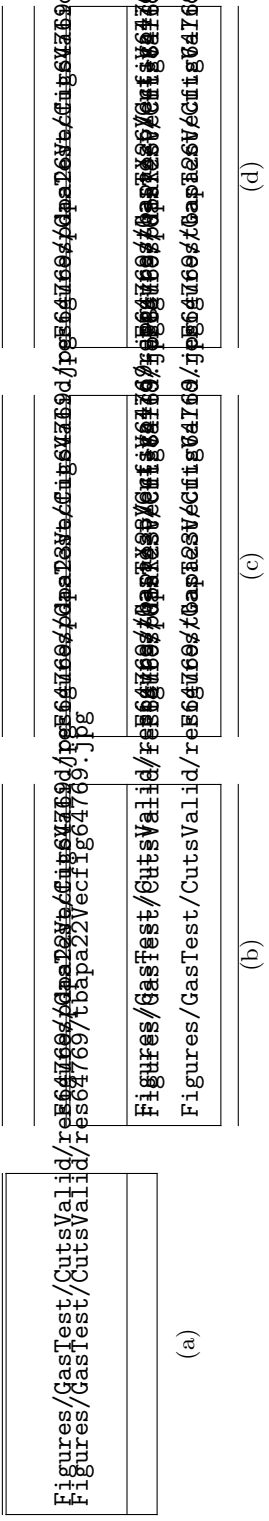


Figure 1.43: *Gas Test* signal selection with ΔV_{T-B} at 14kV, operating gas density at 0.137 mol L^{-1} : (row one) distribution of t_{10-90} duration vs area after signal selections; (row two) distribution of TBA vs area after signal selections; (row three) distribution of t_{10-90} duration vs area of removed signals; (row four) distribution of TBA vs area of removed signals; (a) coincidence event building; (b) applying signal selections based on signal shape; (c) applying signal selections based on the previous signals; (d) applying signal selections based on signal shape and based on the previous signals. The red hatched shaded area indicates the “top-heavy” region. The blue shaded area indicates the “bottom-heavy” region. The magenta hatched shaded area indicates the “long duration” region. The cyan hatched shaded area indicates the “short duration” region. Data were taken at 2017-12-8 14:21, with grid voltages V_T and V_B at +7kV and -7kV. The duration of data taking is 180.01s.

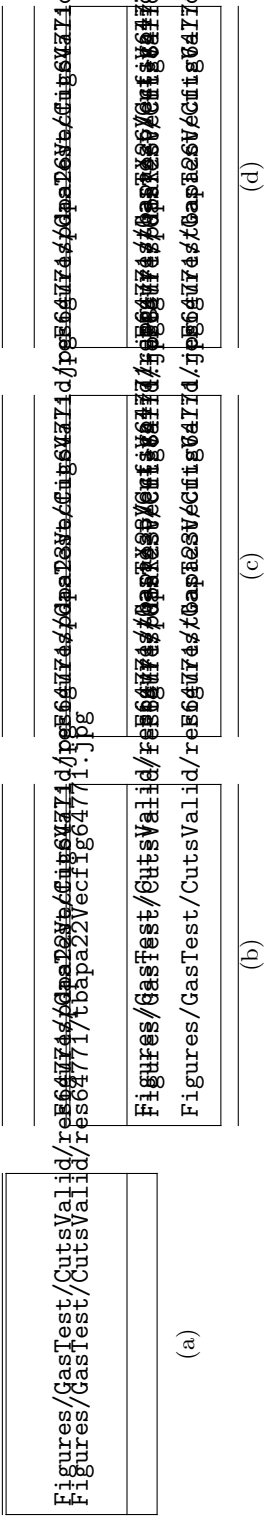


Figure 1.44: *Gas Test* signal selection with ΔV_{T-B} at 16 kV, operating gas density at 0.137 mol L^{-1} : (row one) distribution of t_{10-90} duration vs area after signal selections; (row two) distribution of TBA vs area after signal selections; (row three) distribution of t_{10-90} duration vs area of removed signals; (row four) distribution of TBA vs area of removed signals; (a) coincidence event building; (b) applying signal selections based on signal shape; (c) applying signal selections based on the previous signals; (d) applying signal selections based on signal shape and based on the previous signals. The red hatched shaded area indicates the “top-heavy” region. The blue shaded area indicates the “bottom-heavy” region. The magenta hatched shaded area indicates the “long duration” region. The cyan hatched shaded area indicates the “short duration” region. Data were taken at 2017-12-8 14:42, with grid voltages V_T and V_B at +8 kV and -8 kV. The duration of data taking is 180.10 s.

1451 a figure with $\Delta V_{T-B} = -8\text{kV}$ a figure with $\Delta V_{T-B} = 12\text{kV}$, at 2 bar

1452 1.10 Evaluation

1453 1.10.1 Simulations

1454 Simulations for electron emission signal is

1455 Detailed discussions of the calculation of the electric field is in Appendix ??.

1456 The evaluation of these cuts are estimated by simulations. Cut efficiency is used to indicate the
1457 quality of the cuts. With evaluating the ratio between the simulated electron emission signal passing
1458 cut and the total counts of simulations, the cut efficiency is estimated as

$$\text{cut efficiency} \approx \frac{\# \text{ pulses pass cut}}{\# \text{ simulations}} \quad (1.38)$$

1459 Higher cut efficiency indicates that we are capable of preserving more electron emission signals.
1460 Cut efficiency are evaluated with different detector operation conditions, such as gas density and
1461 grids operation voltage. Since the simulated electron emission signal that I used to evaluate the
1462 cuts have a few discrepancies from the real electron emission signal, the cut efficiency will be not be
1463 exactly accurate. Even though this estimate is only an approximation, the overall cut efficiency are
1464 not wildly off.

1465 1.10.2 Summary

1466 To summarize the cuts that I used, to be an electron emission signal candidate, a pulse should satisfy
1467 these conditions. It should

- 1468 • contain coincidence pulse in both PMTs,
- 1469 • uncorrelated from preceding pulses,
 - 1470 – not have any preceding pulse in the previous $100\ \mu\text{s}$,
 - 1471 – not have any preceding large pulse in the previous 10 ms,
- 1472 • have the correct pulse shape,
 - 1473 – not noise like,
 - 1474 – not have pulse heavily concentrated only in one of the PMTs,
 - 1475 – have longer than single PHE pulse area or positive pulse duration in at least one PMT,
 - 1476 – not “Cherenkov radiation” like,

- 1477 – not S1 like,
- 1478 – not muon like,
- 1479 – not S1 S2 like,
- 1480 – t_{10-90} (signal t_{10-90} duration) matches prediction from electron drift time between the
1481 top and bottom grids,
- 1482 ● not saturate any PMT (this is required for analysis with condition that gas pressure higher
1483 than 1 bara).

1484 **Appendix A**

1485 ***Gas Test* RQ documentation**

1486 This chapter summarizes the definitions of the RQs that are used for analysis in *Gas Test* analysis.

RQ name	shape	type	unit	default
‘aft_tXX’	array (L,)	float32	ns	nan
	Time difference between the start time of the pulse and the integrated pulse area reach XX% of the total area of pulse. XX=05,25,75,95.			
‘aft_t0’, ‘aft_t1’, ‘aft_t2’.	array (L,)	float32	ns	nan
	equivalent to ‘aft_t01’, ‘aft_t50’, ‘aft_t99’.			
‘arearq’	scalar	string		‘waveareas_trim_end’
	RQ used to compute coincidence pulse area.			
‘AmpThreshold’	scalar	float32	mV	2.5
	The threshold value for computing ‘above_threshold’ RQs.			
‘baselines’	array (L,)	float32	mV	nan
	Pulse baseline voltage.			
‘channels’	array (L,)	uint32		
	Pulse channel number.			
‘coin_pulse_amplitudes’	array (N,C)	float32	mV	nan
	Coincidence pulse amplitudes in each channel.			
‘coin_pulse_amplitudes_neg’	array (N,C)	float32	mV	nan
	Coincidence pulse negative amplitudes in each channel.			
‘coin_pulse_areas’	array (N,C)	float32	mV ns	nan
	Coincidence pulse areas in each channel.			

Continued on next page

RQ name	shape	type	unit	default
‘coin_pulse_areas_neg’	array (N,C)	float32	mV ns	nan
	Coincidence pulse negative areas in each channel.			
‘coin_pulse_areas_norm’	array (N,C)	float32	phe	nan
	Coincidence pulse area in each channel.			
‘coin_pulse_areas_post_TTus’	array (N,C)	float32	phe	0
	Pulse area of TT us after the stop time of a coincidence pulse. TT=100,50,20,10.			
‘coin_pulse_areas_pre_TTus’	array (N,C)	float32	phe	0
	Pulse area of TT us before the start time of a coincidence pulse. TT=100,50,20,10.			
‘coin_pulse_areas_section1’	array (N,C)	float32	phe	0
	Pulse area of a coincidence pulse of section1, which is defined by ‘pulse1_start’ and ‘pulse1_stop’.			
‘coin_pulse_areas_section2’	array (N,C)	float32	phe	0
	Pulse area of a coincidence pulse of section2, which is defined by ‘pulse2_start’ and ‘pulse2_stop’.			
‘coin_pulse_areas_sum’	array (N,)	float32	phe	nan
	Coincidence pulse total area.			
‘coin_pulse_areas_tXX’	array (N,)	float32	ns	nan
	Time difference between the start time of the coincidence pulse and the integrated coincidence pulse area reach XX% of the total area of the coincidence pulse. XX=01,05,10,15,25,50,75,85,90,95,99.			
‘coin_pulse_areas_tXXYY’	array (N,)	float32	ns	nan
	'coin_pulse_areas_tYY'-'coin_pulse_areas_tXX'			
‘coin_pulse_chs’	array (N,10)	int32		-1
	First 10 individual pulse channels in the coincidence pulse.			
‘coin_pulse_ids’	array (N,10)	int32		-1
	First 10 individual pulse ids in the coincidence pulse.			
‘coin_pulse_lastpulse_areas’	array (N,C)	float32	mV ns	nan
	Pulse area of the last pulse before a coincidence pulse in each channel.			
‘coin_pulse_lastpulse_ids’	array (N,C)	int32		-1

Continued on next page

RQ name	shape	type	unit	default
	Pulse id of the last pulse before a coincidence pulse in each channel.			
'coin_pulse_lastpulse_lens'	array (N,C)	float64	ns	nan
	Pulse length of the last pulse before a coincidence pulse in each channel.			
'coin_pulse_lastpulse_times'	array (N,C)	float64	ns	nan
	Start time of the last pulse before a coincidence pulse in each channel (since LZ_EPOCH_DATETIME).			
'coin_pulse_lens'	array (N,)	float64	ns	nan
	Coincidence pulse length.			
'coin_pulse_amplitudes_' peaktime	array (N,)	float64	ns	nan
	Time difference between the start time of the coincidence pulse and normalized coincidence pulse reach maximum amplitude.			
'coin_pulse_amplitudes_' peaktime_smooth	array (N,)	float64	ns	nan
	Time difference between the start time of the coincidence pulse and smoothed normalized coincidence pulse reach maximum amplitude.			
'coin_pulse_times'	array (N,)	float64	ns	nan
	Coincidence pulse start time (since LZ_EPOCH_DATETIME).			
'coin_pulse_waveforms'	list (N,C,W)	float32	mV	0
	Waveforms of a coincidence pulse in each channel.			
'coin_pulse_waveforms_norm'	list (N,C,W)	float32		0
	Waveforms of a coincidence pulse in each channel normalize by single photo electron size.			
'coin_pulse_waveforms_sum'	list (N,W)	float32		0
	Sum of waveforms of a coincidence pulse in all channels normalize by single photo electron size.			
'coin_pulse_wtime_tXXYY'	array (N,)	float32	ns	nan
	Pulse height(h_i) weighted average of time(t_i) between 'coin_pulse_areas_tXX' and 'coin_pulse_areas_tYY'. XXYY=1585, 0595. $\bar{t} = \sum h_i t_i / \sum h_i$.			
'coin_pulse_wtimeN_tXXYY'	array (N,)	float32	ns ^N	nan
	$\sum h_i (t_i - \bar{t})^N / \sum h_i$. XXYY=1585, 0595. N=2,3,4.			
'disp'	scalar	string		

Continued on next page

RQ name	shape	type	unit	default
	Display string ‘a:va;g:vg’. (ex: ‘a:+6.5;g:-6.5.’)			
‘duration’	array (F,)	float64	s	
	Duration of a file.			
‘dv’	scalar	float32	kV	
	Voltage difference between the top grid and the bottom grid.			
‘evtnum’	scalar	int64		
	Number of all computed pulses.			
‘firstvals’	array (L,)	float32	mV	
	Value of the first sample of the pulse.			
‘hft_t1’	array (L,)	float32	ns	
	Time difference between the start time of the pulse and the pulse amplitude reach maximum.			
‘in_coin_pulse’	array (L,)	bool		false
	Whether a pulse is in a coincidence pulse.			
‘neg_area_fraction’	array (L,)	float32		nan
	Ratio of negative pulse area and the sum of positive and negative pulse area.			
‘number_of_channels’	scalar	int32		4
	Number of channels.			
‘pos_area_above_threshold’	array (L,)	float32	mV ns	
	Pulse area above a certain threshold (default: 2.5 mV).			
‘pos_len_above_threshold’	array (L,)	float32	ns	
	Pulse length above a certain threshold (default: 2.5 mV).			
‘pos_len_above_threshold_- percentile_XX’	array (L,)	float32	ns	
	Time difference between the start of coincidence pulse of XX percent of all samples above a certain threshold. XX=05,50,95.			
‘pos_len_above_threshold_- trim_end’	array (L,)	float32	ns	
	Pulse length above a certain threshold excluding the ‘suppress_last_NSamples’ period.			
‘posareas’	array (L,)	float32	mV ns	
	Pulse positive area.			
‘pos_area_pulse1’	array (L,)	float32	mV ns	
	Pulse positive area of section1, which is defined by ‘pulse1_start’ and ‘pulse1_stop’.			
‘pos_area_pulse2’	array (L,)	float32	mV ns	

Continued on next page

RQ name	shape	type	unit	default
	Pulse positive area of section1, which is defined by ‘pulse2_start’ and ‘pulse2_stop’.			
‘pos_area_p1_p2’	array (L,)	float32	mV ns	
	‘pos_area_pulse2’ - ‘pos_area_pulse1’			
‘post_baseline’	array (L,)	float32	mV	
	Pulse baseline computed from the end of the pulse.			
‘post_pulse_length’	scalar	float64	ns	1800
	Pulse length not used in the end of a waveform for coincidence pulse searching.			
‘pre_baseline’	array (L,)	float32	mV	
	Pulse baseline computed from the beginning of the pulse.			
‘pre_pulse_length’	scalar	float64	ns	0
	Pulse length not used in the beginning of a waveform for coincidence pulse searching.			
‘procid’	scalar	string		
	Process id. (ex: [12345])			
‘prompt_frac_TTns’	array (L,)	float32		
	Ratio between the pulse area of the first TT ns and the total pulse area. TT=250,500,750,1000			
‘pulse1_start’	scalar	float64	sample	0
	Start time of pulse section 1.			
‘pulse1_stop’	scalar	float64	sample	75
	Stop time of pulse section 1.			
‘pulse2_start’	scalar	float64	sample	0
	Start time of pulse section 2.			
‘pulse2_stop’	scalar	float64	sample	200
	Stop time of pulse section 2.			
‘random_pulse_areas_post_TTus’	array (M,C)	float32	phe	0
	Pulse area of TT us after a random time. TT=100,50,20,10.			
‘random_pulse_areas_pre_TTus’	array (M,C)	float32	phe	0
	Pulse area of TT us before a random time. TT=100,50,20,10.			
‘random_pulse_times’	array (M,C)	float64	ns	nan
	A random time.			
‘rmsratio’	array (L,)	float32		

Continued on next page

RQ name	shape	type	unit	default
	Ratio between Root mean square (rms) of the waveform and the waveform amplitude.			
'sample_size'	scalar	float64	ns	4
	Sample size of a waveform.			
'skimfactor'	scalar	int64		1
	Ratio between the number of all computed pulses and the number of all recorded pulses.			
'sphe_size'	array (C,)	float64	mV ns	inf
	Pulse area of a single photo electron in each channel.			
'suppress_last_NSamples'	scalar	int32		450
	Number of samples not recorded in the end of a waveform.			
'times'	array (L,)	float64	ns	
	Pulse start time (since LZ_EPOCH_DATETIME).			
'trigvals'	array (L,)	float32	mV	nan
	Pulse trigger voltage.			
'usechannels'	array	int32		[0,2]
	Active channels.			
'va'	scalar	float32	kV	
	Voltage of the top grid.			
'vg'	scalar	float32	kV	
	Voltage of the bottom grid.			
'waveamplitudes'	array (L,)	float32	mV	
	Pulse amplitude.			
'waveareas'	array (L,)	float32	mV ns	
	Pulse area.			
'waveareas_trim_end'	array (L,)	float32	mV ns	nan
	Pulse area suppressing last 'suppress_last_NSamples' samples to 0.			
'waveforms'	list (L,)	float32	mV	nan
	Waveform.			
'wavelens'	array (L,W)	float32	ns	
	Pulse length.			
'window_width'	scalar	float64	ns	1500

Continued on next page

RQ name	shape	type	unit	default
	Window size of coincidence pulse searching. It is also called coincidence window width(CWW).			
'wtime'	array (L,)	float32	ns	nan
	Pulse height(h_i) weighted average of time(t_i). $\bar{t} = \sum h_i t_i / \sum h_i$.			
'wtimeN'	array (L,)	float32	ns ^N	nan
	$\sum h_i (t_i - \bar{t})^N / \sum h_i$. N=2,3,4.			
<p>L: number of all computed pulses. N: number of coincidence pulses. M: number of random pulses. C: number of channels. W: number of samples in a waveform. F: number of files in a dataset. LZ_EPOCH_DATETIME: 2015, Jan, 1st, 00 : 00 : 00. phe: average photo electron area.</p>				

Table A.1: Gas Test RQ documentation

1488 **Appendix B**

1489 **Abbreviations**

1490 This chapter summarizes the abbreviations that occur in this thesis.

1491 #: the counts of

1492 ~: approximately

1493 ADC: Analog-to-Digital Converter

1494 avg.: average

1495 BBN: Big Bang Nucleosynthesis

1496 CCD: Charge-couple device

1497 CDF: Cumulative Distribution Function

1498 CMB: Cosmic Microwave Background

1499 config.: configuration

1500 cont.: continued

1501 CSDA range: Continuous Slowing Down Approximation range

1502 CWW: Coincidence Window Width

1503 CV: Coefficient of Variation

1504 DAQ: Data AcQuisition

1505 DM: Dark Matter

1506 dur.: duration

1507 EL: ElectroLuminescence

1508 ELD: ElectroLuminescence Detector

1509 ER: Electron Recoil (event)

1510 LUX: Large Underground Xenon experiment

1511 LZ: LUX-ZEPLIN experiment

1512 max.: maximum

1513 min.: minimum

1514 MFC: Mass Flow Controller

- 1515 NR: Nuclear Recoil (event)
1516 PDE: Photon detection efficiency (also called light collection efficiency)
1517 PDF: Probability Distribution Function
1518 PMF: Probability Mass Function
1519 PEEK: PolyEther Ether Ketone
1520 PHD(phd): counts of PHotoelectrons Detected
1521 PHE(phe): SPHE pulse area or counts of (single) PHotoElectrons. In other literatures, it is
1522 sometime called PE(pe).
1523 PMT: Photomultiplier Tube
1524 PPB(ppb): parts per billion atoms/molecules
1525 PTFE: PolyteTraFluoroEthylene
1526 R&D: Research and Development
1527 refl.: reflectivity
1528 RQ: Reduce Quantity of a pulse
1529 S1: primary Scintillation light
1530 S2: secondary Scintillation light
1531 S, SF: Survival Function
1532 SS: Stainless Steel
1533 QE: Quantum Efficiency (of a PMT)
1534 QF: Quiet Fraction
1535 SLAC: SLAC national accelerator laboratory
1536 TBA: Top-Bottom Asymmetry
1537 TPC: Time Projection Chamber (detector)
1538 vs.: versus
1539 WIMP: Weak Interaction Massive Particle
1540 XML: eXtensible Markup Language
1541 Λ CDM: Lambda Cold Dark Matter

1542 **Bibliography**

- 1543 [1] Hamamatsu Photonics, *Photomultiplier Tubes*, (2006) http://www.hamamatsu.com/resources/pdf/etd/PMT_handbook_v3aE.pdf.
- 1544
- 1545 [2] SAES, *PS3-MT3-R/N SPECIFICATIONS*, (2002) http://www.saespuregas.com/Library/documents/ps3spec_512.pdf.
- 1546
- 1547 [3] KNF Neuberger Incorporated Companies, *Diaphragm-Gas Sampling Pumps with double di-*
1548 *aphragm System*, <https://www.knfsusa.com/products/oem-products/product/products/diaphragm-gas-pumps-and-compressors/double-diaphragm-pumps/>.
- 1549
- 1550 [4] Alicat Scientific, *Operating Manual - MFCs*, http://www.alicat.com/documents/manuals/Gas_Flow_Controller_Manual.pdf.
- 1551
- 1552 [5] T Shutt, *Light guide software for photon propagation (unpublished)*, (2018)
- 1553 [6] C. Silva, “Study of the reflectance distributions of fluoropolymers and other rough surfaces
1554 with interest to scintillation detectors”, (2009).
- 1555 [7] B. Feuerbacher and B. Fitton, “Experimental Investigation of Photoemission from Satellite
1556 Surface Materials”, *Journal of Applied Physics* **43**, 1563 (1972).
- 1557 [8] J. W. Keto, R. E. Gleason, and G. K. Walters, “Production Mechanisms and Radiative Life-
1558 times of Argon and Xenon Molecules Emitting in the Ultraviolet”, *Physical Review Letters*
1559 **33**, 1365 (1974).
- 1560 [9] A. Hitachi et al., “Effect of ionization density on the time dependence of luminescence from
1561 liquid argon and xenon”, *Physical Review B* **27**, 5279 (1983).
- 1562 [10] C. M. B. Monteiro et al., “Secondary scintillation yield in pure xenon”, *Journal of Instrumen-*
1563 *tation* **2**, P05001 (2007).
- 1564 [11] V. Chepel and H. Araújo, “Liquid noble gas detectors for low energy particle physics”, *Journal*
1565 *of Instrumentation* **8**, R04001 (2013).
- 1566 [12] J. C. Bowe, “Drift velocity of electrons in nitrogen, helium, neon, argon, krypton, and xenon”,
1567 Phys. Rev. **117** (1960).

- 1568 [13] C. Geuzaine and J.-F. Remacle, “Gmsh: A 3-D finite element mesh generator with built-in pre-
1569 and post-processing facilities”, *International Journal for Numerical Methods in Engineering*
1570 **79**, 1309 (2009).
- 1571 [14] CSC – Scientific Computing Ltd., *ELMER–a finite element solver for multiphysics*, (1999)
1572 <https://www.csc.fi/web/elmer>.
- 1573 [15] S. Kotila and J. Haataja, “CSC Report on Scientific Computing 1999–2000”, CSC – Scientific
1574 Computing Ltd., Finland (1999).
- 1575 [16] S. Biagi, “Monte Carlo simulation of electron drift and diffusion in counting gases under
1576 the influence of electric and magnetic fields”, *Nuclear Instruments and Methods in Physics*
1577 *Research Section A: Accelerators, Spectrometers, Detectors and Associated Equipment* **421**,
1578 234 (1999).
- 1579 [17] R. Veenhof, “Garfield, recent developments”, *Nuclear Instruments and Methods in Physics*
1580 *Research Section A: Accelerators, Spectrometers, Detectors and Associated Equipment* **419**,
1581 726 (1998).
- 1582 [18] W. Blum, W. Riegler, and L. Rolandi, *Particle Detection with Drift Chambers* (Springer, 2008),
1583 p. 448.
- 1584 [19] COMSOL Inc., *COMSOL Multiphysics Reference Manual, version 5.3*, (2018) [https://www.
1585 comsol.com/](https://www.comsol.com/).
- 1586 [20] US Environmental Protection Agency, “EPA Assessment of Risks from Radon in Homes”,
1587 (2017).
- 1588 [21] D. E. Groom, N. V. Mokhov, and S. I. Striganov, “MUON STOPPING POWER AND RANGE
1589 TABLES 10 MeV–100 TeV”, *Atomic Data and Nuclear Data Tables* **78**, 183 (2001).
- 1590 [22] S. J. C. do Carmo et al., “Absolute primary scintillation yield of gaseous xenon under low drift
1591 electric fields for 5.9 keV X-rays”, *Journal of Instrumentation* **3**, P07004 (2008).
- 1592 [23] L. M. P. Fernandes et al., “Primary and secondary scintillation measurements in a Xenon Gas
1593 Proportional Scintillation Counter”, *Journal of Instrumentation* **5**, P09006 (2010).
- 1594 [24] U Fano, “Penetration of Protons, Alpha Particles, and Mesons”, *Annual Review of Nuclear
1595 Science* **13**, 1 (1963).
- 1596 [25] S. P. Ahlen, “Theoretical and experimental aspects of the energy loss of relativistic heavily
1597 ionizing particles”, *Reviews of Modern Physics* **52**, 121 (1980).
- 1598 [26] V. Álvarez et al., “Initial results of NEXT-DEMO, a large-scale prototype of the NEXT-100
1599 experiment”, *Journal of Instrumentation* **8**, P04002 (2013).
- 1600 [27] P. Sorensen and K. Kamdin, “Two distinct components of the delayed single electron noise in
1601 liquid xenon emission detectors”, *Journal of Instrumentation* **13**, P02032 (2018).

- ¹⁶⁰² [28] A.~Kramida, Yu.~Ralchenko, and J.~Reader, *No Title*, (2018)